1995

Synthesis, characterization and application of electrode materials

Lin He
Iowa State University

Synthesis, characterization and application of electrode materials

by

Lin He

A Dissertation Submitted to the

Graduate Faculty in Partial Fulfillment of the

Requirements for the Degree of

DOCTOR OF PHILOSOPHY

Department: Chemistry
Major: Physical Chemistry

Approved:

Signature was redacted for privacy.

In Charge of Major Work

Signature was redacted for privacy.

For the Major Department

Signature was redacted for privacy.

For the Graduate College

Iowa State University
Ames, Iowa

1995

TABLE OF CONTENTS

ACKNOWLEDGEMENTS

I would like to express my thanks to Dr. Hugo F. Franzen, my major professor, and Dr. Dennis C. Johnson for their guidance, support and patience throughout my graduate studying at Iowa State University. Without them my PhD work will never be completed. I really enjoy having two mentors as my research advisors and it has been an honor to work and learn under their supervision.

I would like to thank Dr. Robert A. Jacobson, Dr. Jacob W. Petrich and Dr. Kenneth R. Jolls for their taking time and serving as my PhD program committee members.

I would also like to thank the many members, past and present, of Dr. Franzen's group, Dr. Johnson's group and Dr. Corbett's group for the valuable discussion and help. Special thanks go to Dr. R. A. Mackey and Dr. J. E. Vitt for teaching me in my first year at Iowa State University in solid state and electrochemistry laboratories, respectively.

I am indebted to Mr. James Anderegg for doing ESCA and a lot of suggestions and discussion. Thanks are also extended to Mr. Jerry Amenson for the SEM of Pt-Ti_4O_7 RDEs and Dr. V. Young and Dr. L. M. Thomas for the XRD. I'd like to thank Ms. Shirley Standley for organizing everything successfully and making every day enjoyable.

I would like to express my thanks and gratitude to my parents whose constant encouragement and support I could always count on. Finally, I would like to express my special thanks to my husband, Youchun, for his continuing love and support. He has provided not only encouragement and help but also happiness in my life.

This work was performed at Ames Laboratory under Contract No. W-7405-Eng-82

with the U.S. Department of Energy. The United States government has assigned the DOE Report number IS-T 1739 to this thesis.

GENERAL INTRODUCTION

1. Dissertation Organization

This dissertation consists of four manuscripts preceded by a General Introduction and followed by General Conclusions. The general introduction gives background information about the interdisciplinary field of solid state chemistry and electrochemistry including electron-transfer and mass-transport, structure and properties of oxide surfaces, electrochemical kinetics, electrode design and blocking effects.

The research described in this dissertation was a result of collaboration of physical chemistry and analytical chemistry, and was performed under the direction of Dr. Hugo F. Franzen and Dr. Dennis C. Johnson. The first manuscript contains the results of a study of Ru microelectrode arrays within a conductive Ti_4O_7 ceramic matrix. These Ru-Ti_4O_7 rotating disk electrodes (RDEs) were examined by x-ray diffraction (XRD), scanning electron microscopy (SEM) - energy dispersive spectrometer (EDS), voltammetry and amperometry. The second manuscript includes the results of a study of the electrocatalysis of anodic O-transfer reactions on the pyrochlore oxide $Bi_2Ru_2O_{7.3}$ for several anodic reactions. In the third manuscript, the study of electrocatalysis focuses on I^- oxidation and IO_3^- reduction at $Bi_2Ir_2O_7$ in acidic media. The last paper consists of the investigation of Pt microscale electrodes on a Ti_4O_7 matrix yielding composite electrodes which dramatically increase the current densities.

2. Electron transfer and mass transport

An electrochemical reaction is a heterogeneous chemical process involving the transfer of charge to or from an electrode, generally a metal or semiconductor. The charge transfer may be a cathodic process in which an otherwise stable species is reduced by the transfer of electrons from the electrode. Conversely, the charge transfer may be an anodic process where an otherwise stable species is oxidized by the removal of electrons to the electrode. Since the rate of electrochemical reaction is determined by the rate of the overall sequence of reaction steps, it is controlled by the rate of the slowest step in the sequence. Thus, to understand the characteristics of such an electrode reaction, we need to know about both mass transport and electron transfer.

The simplest model for the electron-transfer process involves the hopping of an electron between the electrode and the electroactive species. However, the electrode reactions of interest in electrochemical technology are seldom that simple. They involve multiple electron transfers and the possibility of at least three additional types of basic steps.

(a) Chemical reactions

The species formed by electron transfer may be unstable in the electrolysis medium: it may only be an intermediate product which undergoes chemical change to form the observed product.

(b) Adsorption

Adsorption has important roles in electrochemical technology. Sometimes , it is a

key step since its occurrence on the surface provides alternative lower energy pathways.

(c) Phase formation

The electrode reaction may involve the formation of a new phase or the transformation of a new solid phase to another.

Since electrode reactions commonly involve the transfer of several electrons, the complications can occur between, preceding or following electron transfer. Moreover, very complex situations do arise. It is possible to involve electron transfer, diffusion, chemical reactions, phase transformation and adsorbed intermediates.

In general, in electrochemical systems, it is necessary to consider three mechanisms of mass transport; namely diffusion, migration and convection.

(a) Diffusion

Diffusion is the movement of a species down a concentration gradient and it occurs whenever there is a chemical change at a surface. An electrode reaction converts starting material to a product and, hence, close to the electrode surface a boundary layer develops in which the concentrations of starting material and product are a function of distance from the electrode surface. The concentration of starting material is lower at the surface than in the bulk while the opposite is the case for product, and hence, starting material will diffuse towards and product away from the electrode.

(b) Migration

The current of electrons through the external circuit must be balanced by migration of ions through the solution between the electrodes. Migration is the movement of charged

species due to a potential gradient and it is the mechanism by which charge passes through the electrolyte; The forces leading to migration are purely electrostatic and hence do not discriminate between types of ions.

(c) Convection

Convection is the movement of a species due to mechanical forces. In practice, it is much more common to stir or agitate the electrolyte or to flow the electrolyte through the cell. These are all forms of forced convection and, when present, it is always the predominant form of mass transfer.

3. Structure and properties of oxide surfaces

When a solid is immersed in aqueous solution its surface usually acquires a net electric charge which in turn is balanced by a region of opposite charge in the solution adjacent to the solid surface. This charge separation at the interface is known as an electrical double layer. The properties of this double layer play an important role in the adsorption of charged chemical species. Hence, it is important in understanding many technologically important phenomena such as ion exchange, froth flotation and electrode processes. This is particularly true for insoluble metal oxides such as SiO_2, TiO_2, Fe_2O_3, Al_2O_3, alumino-silicates, etc., because of their natural abundance as minerals and soils and also because of their commercial importance as pigments, thickening agents, abrasives, and as oxide films on metal electrodes.

For metal oxide electrodes, one very important point is the problem of the true surface area of these films. Some evidence for a high surface area can be inferred from the

low crystallinity as observed by x-ray analysis. It is known[1] for powders that the lower the crystallite size, the higher the specific surface area. Crystal growth is favored by a high firing temperature together with a slow heating rate and a highly oxidizing atmosphere.

Although oxide particles can be prepared in many different ways one approach to describing the structure of an oxide surface is to consider it as resulting from the cleavage of a bulk oxide crystal[2-5]. The surface formed by cleavage would consist of oxygen and metal atoms that are unsaturated with respect to co-ordination and carry formal charges. This surface would be highly strained M-O-M surface bonds[4,6]. However, in the presence of water vapor, dissociative chemisorption of water molecules can occur on the strained surface giving a layer of surface hydroxyl groups. This chemisorption process presupposes that hydroxyl groups can be accommodated on adjacent metal atoms.

In addition to the two possible forms of chemisorbed water on oxides, hydroxyl groups and water molecules, physical adsorption of molecular water will occur to give layers of relatively loosely water bound. Hence, interaction with oxide surfaces may involve interactions with metal cations, oxide anions, hydroxyl groups and/or water molecules.

Mixed metal oxides often generate additional surface acidity over their individual end members because of an increase in the polarizability of the hydroxide groups present in the mixed oxide[7,8].

It has often been suggested that porosity is important to the establishment of the electrical double layer properties of oxides[9]. Since it was first observed that the surface charge densities on oxide surfaces are generally considerably higher than those on

corresponding mercury and AgI/solution interfaces, several theories have been postulated for the structure of the electrical double layer at the oxide-solution interface. Most of these theories are based on either the Gouy-Chamman-Stern-Grahame (GCSG) model or the porous double layer (PDL) model proposed by Tadros and Lyklema[9-11]. The fundamental difference between the two models is that in the GCSG model the surface charge is confined to a flat surface plane and the counter charge to the solution side of the interface. whereas in the PDL model, the surface charge together with part of the counter charge can penetrate into the solid. The two models treat the diffuse layer on the solution side of the interface in the same way.

4. Electrochemical kinetics

Electrochemistry is particularly well-suited to kinetic studies, since the electrode current provides a direct measure of the overall rate of the electrochemical reaction. This relationship becomes apparent from differentiating Faraday's law with respect to time[12].

$$Q = nFN \qquad [1]$$

$$dQ/dt = i = nF(dN/dt) \qquad [2]$$

Eqn. [2] illustrates the difference between electrochemical kinetics, where the rate of a reaction is given as the number of moles reacted per unit time (dN/dt), and homogeneous solution kinetics, where the rate is often expressed as a change in concentration per unit time (dC/dt). The current is proportional to the electrode area and, therefore, the rate is usually normalized by the electrode area.

$$\text{rate} = dN/(Adt) = i/(nFA) = k_{app}C^s \qquad [3]$$

Eqn. [3] is based on the assumption that the net rate of the reaction can be approximated by an elementary reaction involving the transfer of n electrons in a single step. The apparent heterogeneous rate constant, k_{app}, is the apparent rate constant for this hypothetical one-step reaction, and is used as an empirical measure of the kinetics of the electrode reaction. The equivalence between electrode current and the rate of the reaction makes the application of steady-state methods very desirable. Rotated disk electrodes (RDE) can be used to provide a constant flux of reactant and, therefore, the current is independent of time.

A concentration gradient between the surface of the electrode and the bulk solution always develops as the reactant is consumed by electrochemical reaction, resulting in diffusion of reactant to the electrode. Nernst estimated that the concentration gradient could be approximated by a linear relationship, where the diffusion layer thickness (δ) is the distance from the electrode surface where the concentration is approximately equal to the bulk concentration (C^b). In this case, the reaction rate is equal to the flux of reactant due to diffusion[13].

$$i/nFA = (D/\delta)(C^b - C^s) \qquad [4]$$

By comparison with Eqn. [3], it is apparent that the term D/δ in Eqn.[4] can be thought of as a rate constant for mass transport, and has the same units (cm s^{-1}) as does k_{app}. For a reaction that is completely mass-transport limited, C^s can be assumed to be essentially zero. The diffusion layer thickness, δ, has been solved for two experimental situations which will be of interest here: a planar electrode in unstirred solution and a rotated disk electrode.

The diffusion layer thickness is equal to $(\pi Dt)^{1/2}$ for a planar, disk electrode in an unstirred solution where diffusion is restricted to the direction normal to the plane of the electrode surface. This value is substituted into Eqn. [4] to yield the Cottrell equation[14].

$$i_{lim} = nFAD^{1/2}C^b/(\pi t)^{1/2} \quad [5]$$

This equation is based on the assumption that, at $t = 0$, the potential of the electrode is stepped from a value where no reaction occurs to a value where the reaction occurs at a mass-transport limited rate. This implies that $C^s = 0$ for $t > 0$. Also, the disk electrode must be uniformly accessible to the reactant, that is, the current must be equal at all points on the electrode surface.

The current at a stationary disk electrode varies with the inverse square root of time ($t^{-1/2}$), as shown in Eqn. [5]. It is much more convenient to choose conditions where the current does not vary with time. This is the case at a rotated disk electrode (RDE), where convection supplies a constant flux of reactant to the electrode surface. With this experimental configuration, the current is constant at any given value of electrode potential if the bulk concentration of the electroactive species can be assumed to be constant for the duration of the experiment.

The diffusion layer thickness (Eqn. [6]) at a rotated disk electrode was found by Levich and, when combined with Eqn. [4], gives the Levich equation[15].

$$\delta = 1.61D^{1/3}\nu^{1/6}\omega^{-1/2} \quad [6]$$

$$i_{lim} = 0.62nFAD^{2/3}\nu^{-1/6}C^b\omega^{1/2} \quad [7]$$

A correction to the constant term 0.62 in Eqn. [7] has been given (Eqn. [8])[16]. This

constant reduces to 0.62 when D is much smaller than ν.

$$\text{constant} = 0.554/(0.8934 + 0.316\,(D/\nu)^{0.36}) \qquad [8]$$

Like the Cottrell equation, the Levich equation is based on the assumption that the current is equal at all points on the electrode surface and that the current is limited only by mass transport. The diffusion layer thickness is the distance at which convection maintains the concentration of the electroactive species approximately equal to the bulk concentration. At distances $< \delta$, mass transport of the electroactive species in the direction normal to the electrode surface occurs mainly by diffusion.

Measurement of the current for a mass transport limited reaction can give useful information about the net reaction, such as the value of n or D. However, kinetic information is necessarily absent from current measurements that are limited only by mass transport of the electroactive species to the electrode. Kinetic information is present only under conditions when the current is less than the mass-transport limited values predicted by Eqns.[5] and [7].

The equation for conditions of mixed control by mass transport and kinetic processes is obtained by solving Eqn. [3] for C^s and substituting this result into Eqn. [4]. This equation can be rearranged to give Eqn. [9].

$$i = nFADC^b/(\delta + D/K_{app}) \qquad [9]$$

When the kinetics are fast with respect to mass transport ($D/K_{app} \ll \delta$), this equation reduces to Eqn. [4] where $C^s = 0$, i.e., the equation for mass-transport controlled reactions. When kinetics are slow compared to the rate of mass transport ($D/K_{app} \gg \delta$),

this equation reduces to Eqn. [3] where $C^s = C^b$, i.e., the equation for irreversible reactions in the absence of mass transfer effects.

The equation for reactions under mixed control at a stationary disk electrode (Eqn. [10]) is obtained by substituting the diffusion layer thickness from the Cottrell equation (Eqn. [5]) into Eqn. [9].

$$i = nFADC^b/((\pi Dt)^{1/2} + D/k_{app}) \qquad [10]$$

Note that at long times, the current approaches the current for the purely mass transport limited case. Therefore, in theory, Cottrell data at long times can be used to determine useful information about the net reaction such as n and D, even when there are kinetic limitations on the current at short times.

The equation for the RDE can be obtained in an analogous manner by substituting Eqn. [6] into Eqn. [9]. This equation is commonly called the Koutecky-Levich equation[15].

$$i^{-1} = (nFAK_{app}C^b)^{-1} + (0.62nFAD^{2/3}\nu^{-1/6}C^b\omega^{1/2})^{-1} \qquad [11]$$

This equation is written in the inverse form so that the effects of mass transport can be separated form the effects of kinetics. Based on Eqn. [11], a plot of i^{-1} vs. $\omega^{-1/2}$ gives a slope dependent on the mass transport characteristics of the net reaction, and an intercept dependent on the kinetics.

One of characteristics, K_{app}, for a reaction at the RDE can be obtained for the specific mechanism and substituting the result into Eqn. [11]. For example, the i-E curve for an irreversible electron-transfer oxidation can be obtained by substituting k_{app} for an anodic electron-transfer reaction into Eqn. [11]. The apparent rate constant, k_{app}, varies with

potential according to Eqn. [12]. The results can be plotted according to Eqn. [13] for different values of k°.

$$k_{app} = k°\exp\{\alpha_a nF(E-E°')/RT\} \quad [12]$$

$$i = nFADC^b/(1.61D^{1/3}\nu^{1/6}\omega^{-1/2} + D/K°\exp\{\alpha_a nF(E-E°')/RT\}) \quad [13]$$

Note that at large overpotentials, the current reaches the mass-transport limited value regardless of k°. Thus, at large overpotentials, a plot of i^{-1} vs. $\omega^{-1/2}$ for a simple electron-transfer process yields no kinetic information, and corresponds to the mass-transport limited response predicted by the Levich equation (Eqn. [7]). However, the anodic wave is shifted to more positive potentials as k° decreases. The half-wave potential ($E_{1/2}$) can be found by setting Eqn. [13] equal to one-half of the mass-transport limited current given by Eqn. [7][17].

$$E_{1/2} = E°' + (RT/\alpha_a nF)\ln(D/1.61D^{1/3}\nu^{1/6}\omega^{-1/2}k°)) \quad [14]$$

Thus, i-E data at the RDE can be used to obtain both the kinetic and mass-transport characteristics of simple electron-transfer reactions.

For real electrochemical systems, the mass-transport limited current predicted by Eqn. [7] is rarely achieved. However, i-E curves often show large regions where the current is independent of potential, indicating that some other step besides electron transfer is rate limiting.

The apparent rate constant has been obtained for several possible mechanisms where electron transfer is not rate limiting. Consider an electrochemical reaction where the electron transfer is preceded by a chemical step, as represented by Eqn. [15] and [16]. This is commonly referred to as a CE mechanism. When $E \gg E°'$, the apparent rate constant

is given by Eqn. [17] [12]

$$A \underset{k_r}{\overset{k_f}{\rightleftharpoons}} B \qquad [15]$$

$$B \xrightarrow{k_a} C + ne^- \qquad [16]$$

$$k_{app} = DK_{eq}/X_R \qquad [17]$$

where $X_R = (D/(k_f + k_r))^{1/2}$

The limiting currents could be measured from Eqns. [11] and [17] for various rotation rates of the electrode. These results could be plotted as i vs. $\omega^{1/2}$, along with the results from Eqn.[7] for the mass-transport limited reaction. For the CE mechanism, the limiting currents are much smaller than the mass-transport limited values. This difference becomes larger at larger rotation rates (smaller δ). The rate constants were deliberately chosen so that at high overpotentials D/k_{app} would be about the same size as δ. For much larger values of D/k_{app} (slower kinetics), the limiting current is independent of rotation rate. For much smaller values of D/k_{app} (faster kinetics), the limiting current would correspond to the mass-transport limited value predicted by the Levich equation.

The data also could be plotted as i^{-1} vs. $\omega^{-1/2}$. The slope calculated from i^{-1} vs. $\omega^{-1/2}$ data is unchanged by kinetic limitations on the current, and can be used to calculate the number of electrons transferred in the net electrochemical reaction, provided a value of D is available. The value of k_{app} calculated form the intercept can be used to calculate rate constants, provided k_{app} can be solved based on the mechanism of the reaction. This is possible for only a few simple mechanisms, including the CE mechanism described here.

It is much more common to simply use the value of k_{app} as an empirical measure of the rate of the electrochemical reaction.

Voltammetric data often resemble the data for the simple CE model. For example, the anodic, oxygen-transfer reactions discussed in this dissertation are almost always irreversible, with $E_{1/2}$ values that are much greater than their E°' values. Also, the limiting current rarely approaches the mass-transport limited value predicted by the Levich equation. This implies that a step other than electron transfer is rate limiting for these reactions. The slow chemical step might correspond to any combination of the following: deprotonation, oxygen transfer, adsorption of reactants, a change in the surface characteristics of the electrode, or a change in conformation of a reactant or an intermediate species.

The value of k_{app} in Eqn. [17] for the CE mechanism was calculated using the reaction layer approach based on the assumption that the homogeneous reactions are rapid so that the hypothetical reaction layer (X_R) is much smaller than the diffusion layer (δ). Digital simulation can be used to provide a more exact solution for electrochemical problems which can only be solved directly by making numerous assumptions[18,19].

5. Electrode design

Electrode design consists of the fashion of working electrode, reference electrode and counter electrode. In our experiments, the reference and counter electrodes were the saturated calomel electrode and platium electrode, respectively. The research in this work will focus on the design of the working electrode. In most of the cases it is the electrode material itself that is under investigation and so its composition, and indeed its shape and

size, may well be determined by outside factors.

(A)General consideration The complexity of electrode behavior and our lack of detailed insight make it impossible to select the optimum electrode for a given process on a theoretical basis. The most satisfactory electrode configuration will be determined by the experimental conditions. For instance, small electrodes will allow high current densities to be employed with minimal ohmic heating, which is very important in low-conductivity solutions. This approach is also useful if high-current sources are not available. On the other hand, the use of the end face of a thin wire can be awkward because of the difficulty in obtaining a reproducible and known electrode area and surface finish[20]. Nevertheless, there are some general guidelines to assist the choice of an electrode material:

(a) Physical stability

The electrode material must have adequate mechanical strength, must not be eroded by the electrolyte, reactants, or products, and must be resistant to cracking.

(b) Chemical stability

The electrode material must be resistant to corrosion, unwanted oxide or hydride formation, and the deposition of inhibiting organic films under all conditions experienced by the electrode.

(c) Suitable physical form

The material must be easy to fabricate into the form demanded by the reactor design, to facilitate sound electrical connections, and to permit easy installation and replacement at a variety of scales.

(d) Electrical conductivity

The electrode system must have reasonably high conductivity including the current feeder, electrode connections, and the entire electrode surface exposed to the electrolyte. Only in this fashion is it possible to obtain a uniform current and potential distribution as well as to avoid voltage losses leading to energy inefficiencies.

(e) Rate and product selectivity

The electrode material must support the desired reaction and, in some cases, significant electrocatalytic properties are essential. The electrode material must promote the desired chemical change while inhibiting all competing chemical changes.

(f) Cost and lifetime

A reasonable and reproducible performance including a lifetime probably extending over several years must be achieved for an acceptable initial investment.

Today, the environment is a big issue, the electrodes and their compounds must have a low toxicity.

The need for electrocatalysts in electrochemical technology is widely appreciated[14] as the use of these materials may lead to significant energy saving, more efficient energy conversion (great selectivity or faster rates of reaction with consequent saving in plant size and capital cost), and increased electrode stability. Many electrode reactions only occur at a measurable rate at a very high overpotential, i.e. k is low. The art of electrocatalysis is to provide alterable reaction pathways which avoid the slow step and permit the reaction to be carried out with a high current close to the reversible potential, i.e., to increase k.

It is important to design and construct an electrode from the catalyst materials. Since some modern catalysts are not metals, it may be necessary to mix the catalyst with an inert conductor and a binder, and press them onto a supporting grid or to develop a technique for coating them onto an inert metal. In practice, the electrode may be operated as a porous gas electrode or as a gas-evolving electrode and this will also place additional restraints on the design. Certainly under the electrolysis conditions the electrode structure must be physically stable, resistant to corrosion and the catalyst must maintain its activity over a long period of time, i.e. the electrode doesn't do the poisoning.

What factors determine the activity of electrocatalysts and are likely to introduce specificity into an electrode reaction? At the present time, a complete answer to this question is not possible and we have certainly not reached the stage where it is possible to design electrocatalysts from theoretical consideration. On the other hand, a number of general principles can be set out. Thus, while metals, alloys, semiconductors (particularly oxides) and complexes are based on transition metals and it seems that the design of a catalyst requires the placing of transition-metal ions or atoms in a matrix which serves to optimize their electronic configuration and position with respect to each other.

The dependence factors of electrocatalysis has already been emphasized and therein lies the explanation of the success of transition metals as catalysts; they have unpaired d-electrons and unfilled d-orbitals which are available to form bonds with the adsorbate. The free energy of adsorption will, however, depend strongly on the number of unpaired electrons per atom and also on their energy levels. Hence, it is not surprising that activity

electrons per atom and also on their energy levels. Hence, it is not surprising that activity varies with the identity of the transition metal and may be modified by alloying or placing the transition metal in a non-metallic lattice. In the limit, the lattice and the adsorbate may be considered as ligands in a metal complex. The observation that the rate of reaction for hydrogen evolution passes through a maximum when plotted versus free energy of adsorption is equally true of other electrocatalytic processes and, hence, the objective should be to tailor the electronic environment of the metal to obtain the free energy of adsorption that leads to the maximum current density.

In addition to electronic factors, the geometric arrangement of catalyst centers will also be important. All electrocatalytic reactions involve the formation or cleavage of bonds and it is likely that such processes will be substantially increased in rate if they can occur as concerted reactions. For example in the reduction of chlorine, the bond between the surface and the chlorine atoms forms at the same time as the Cl-Cl bond is broken:

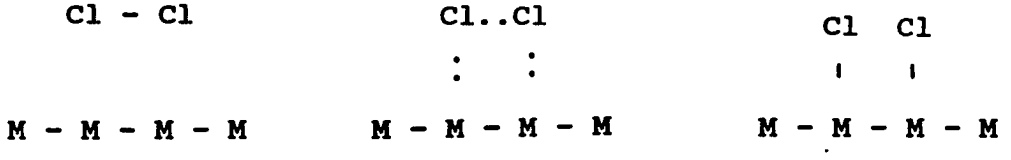

Such mechanisms require the correct spacing of the adsorption sites. Here the sites are written as the metal atoms themselves but it is also possible that adsorption occurs at interstitial positions although the argument would remain the same. The adsorption of larger

appropriate site spacings.

The activity of electrocatalysts can further be enhanced by special sites on the surface, edge sites, lattice vacancies, grain boundaries and dislocations have all been suggested to have beneficial effect. This may be because they lead to sites with different free energies of adsorption or because they create unusual spacings or arrangements of potential adsorption sites.

How can we set out to find the most suitable catalysts? The various stages in the overall processes may require properties different from those of the transition metal and one way of facilitating this is to use transition metals where the oxidation state can readily be altered.

Once the catalyst is developed, it remains necessary to construct an electrode incorporating it. In electrocatalytic processes, the real surface area of the electrode is important and the measured exchange current density can be increased by preparing a rough or otherwise high-area surface. This is in contrast to mass-transfer-controlled reactions where only the apparent geometric area matters provided that the surface roughness is small compared with the diffusion layer thickness. Hence, a variety of procedures for obtaining high-surface-area electrodes have been developed; these including spray coating, sputtering, thermal decomposition of solutions of a catalyst or a catalyst precursor and painting dispersions of the appropriate crystallite size. For example, satisfactory platinum electrodes have been manufactured with very low loading of the active metal, e.g. a few milligrams per square centimeter of graphite.

(B) Microelectrode Microelectrodes are defined as electrodes which have particle size between 0.1 and 50 μm. Common geometries include spherical, hemispherical, disc, ring, and line. They exhibit high current densities, but low total currents. Electrodes of microscale have found a number of applications in electrochemical kinetic studies[22-24]. Ensembles of microelectrode have been proposed[25-28] as a way of increasing the magnitude of the current, while maintaining the advantages of the single microelectrode with respect to diffusion and ohmic drop.

Comparing ordered arrays (e.g., hexagonal and square lattice), the random array shows considerably lower currents[29]. These lower currents originate from the lower symmetry of the random array, where the diffusion zones extending out from the microelectrodes do not inscribe uniformly within the voids of the array. Their overlap being higher, the resulting current is therefore lower. A closed form distribution function for randomly distributed non-overlapping circles on the plane is unfortunately unavailable.

Electrodes having structurally heterogeneous surfaces are frequently used in electroanalytical chemistry. Examples of electrodes that are deliberately constructed to be heterogeneous include carbon paste and other composite electrodes, and microelectrode arrays. Unintentional heterogeneity at solid electrode can result from electrode processes such as adsorption or filming. Structural heterogeneity, whether it is caused by deliberate design or by processes subsequent to electrode construction, can result in a level of electrochemical activity that is nonuniform over the electrode surface. In an extreme case, an electrochemically heterogeneous electrode might consist of well-defined active regions

that, although electrochemically active, exhibit dissimilar electron transfer kinetics. Characterization of kinetically heterogeneous surfaces should prove important to the optimization of electrode design and to the correct interpretation of data obtained from such surfaces.

(C) Composite electrode A composite electrode has a surface that consists of an ordered arrangement or a random arrangement of conductor regions, typically micrometers in dimension, separated from one another by an insulator. These active regions may themselves be of regular geometry and confined primarily to the surface, as with most array electrodes.

Composite electrodes offer many potential advantages compared to more traditional electrodes consisting of a single conducting phase, such as glassy carbon, mercury, platinum, or gold. For example, composite electrodes can often be fabricated with greater flexibility in size and shape of the material, permitting easy adaptation to a variety of electrode configurations. Composite electrodes made from precious metals offer advantages in the form of less weight and lower cost (per unit of current density) in comparison to their pure counterparts. Of particular advantage in electroanalysis is the higher signal-to-noise (S/N) ratio often observed with composite electrodes, relative to the corresponding solid electrode, which generally translates into improved (lower) limits of detection. Perhaps the most exciting aspect of composite electrode is the versatility they provide for incorporating selectivity and/or sensitivity enhancement into the bulk electrode material, either through chemical modification of the active sites or through physical incorporation

into the composite matrix. Unlike surface-modified electrodes, these bulk-modified composite electrodes can be resurfaced without loss of modifier.

(D) Fabrication of Composite Electrodes Most array electrodes used in electroanalysis are surface arrays and are not bulk composite materials. Some selected examples of surface arrays include linear arrays of gold- and platinum-band microelectrodes fabricated using photolithographic and thick-film technologies,[30-32] arrays of gold and platinum interdigitated microband electrodes fabricated by photolithography[33,34], ordered arrays of microdisk electrodes formed photolithographically by etching holes through a photoresist coating on a macrodisk glassy carbon electrode[35], and hexagonal arrays of chromium, and gold disk electrodes formed by electron-beam etching of a polymethymethacrylate resist coating on the metal substrate[36]. These surface arrays have well-defined geometries, an advantage when attempting to understand the theoretical behavior of such electrodes.

The studies performed by Adams and co-workers on carbon paste electrodes were the first serious investigations of the properties of composite electrode materials[37]. Other examples of this type of composite include the polythiazyl paste[38] and poly(chlorotrifluoroethylene) oil carbon paste[39] electrodes.

Solid dispersed composites are most often fabricated in one of two ways. The most common method involves uniformly dispersing a conductor in a monomer that is subsequently polymerized, as with the epoxy/graphite[40,41], bulk-modified epoxy/graphite[42], epoxy/carbon fiber[43], silicone rubber/graphite[44], bulk-modified polystyrene/carbon black[45], and bulk-modified polystyrene/carbon fiber[46] electrodes.

Consolidated composites are also fabricated by one of two general approaches. One approach involves the impregnation of either a porous conductor with an insulator or a porous insulator with a conductor. In this case, the consolidation of the conductor within the composite is predetermined by the porous structure of the conductor or insulator. Examples include the various impregnated graphite rod electrodes[47], the epoxy-impregnated reticulated vitreous carbon electrode[48], microcellular carbon foam/epoxy electrode[49], and the platinum and the carbon paste impregnated polycarbonate membrane electrodes[50,51].

The second approach to forming consolidated electrodes involves mixing a powdered conductor with a powdered polymer and compression molding the mixture, as with the polyethylene/graphite[52], Teflon/graphite[53], Kel-F/graphite[54-56] , and Kel-F/precious metal[57,58] electrodes (Kel-F is a 3M trade name for poly(chlorotrifluoroethylene)). After mixing, the conductor particles occupy the interstices between the larger polymer particles. Such systems have been referred to as segregated distributions in the applied physics literature[59].

(E) Composite electrode surface morphology---An array electrode is designed and fabricated to possess a well-defined, rather simple surface geometry, and scanning electron microscopy (SEM) and/or optical microscopy are often used to confirm the geometry. On the other hand, the surface morphology of an ensemble electrode can be exceedingly complex, and a variety of techniques for probing the surface morphology is required to fully understand the relationship between surface morphology and electrochemical response. For example, the morphology of the surface of a Kel-F/gold composite electrodes has been examined by SEM[58,60] and the active sites have been confirmed by energy-dispersive x-ray

analysis (EDXA)[58]. Furthermore, the electrochemically active area of such composite materials has been probed by capacitance measurements,[58,60,61] chronoamperometry[58], x-ray photoelectron spectroscopy (XPS)[61], and electrogenerated chemiluminescence (ECL) imaging[61].

6. Blocking effects

The apparent charge transfer rate constant observed for partially blocked electrode surfaces is composed of two rate components. It may be assumed that at any particular potential and concentration of adsorbed species, the fraction θ is covered by the blocking species and the fraction $(1-\theta)$ corresponds to the free surface area. The charge transfer rate constant in the blocked area and free area may be assumed to be k_b and k_f respectively. The overall apparent rate constant is then given by Eqn.[18]

$$k_a = (1-\theta)k_f + \theta k_b \qquad [18]$$

In most of the cases, it turns out that k_b is very much smaller when compared with k_f and, hence, when evaluating blocking effects involving mass transport, it is usually assumed that k_b is zero and thus Eqn.[18] becomes

$$k_a = (1-\theta)k_f \qquad [19]$$

Concerning the mass transport problem at a microscopical uniform planar electrode, the electron transfer takes place uniformly throughout the electrode surface and concentration changes also occurring uniformly. Hence, the concentration of electroactive species varies only in the direction perpendicular to the plane of the electrode surface. At all the planes in the solution side which are parallel to the electrode surface, the concentration at any

point of time is uniform. Hence, one can employ semi-infinite linear diffusion condition for treating mass transport. However, the situation becomes much more complex when the electrode contains permanent blocking and active regions. The concentration of active species deceases first in the active regions. In the blocking regions, the concentration still remains equal to the bulk concentration. Hence, the concentration gradient exists in two directions, one perpendicular to the electrode surface plane and another at the boundary between the active and blocking region. Now the mass transport problem becomes non-linear. The mass transport not only depends on the total blocked and active surface area components, but also on the geometry of the blocked and active regions. They can be of different sizes and shapes.

According to the relative magnitude of the average distance between two active sites, $2R_o$, and the thickness of the diffusion layer, δ, several types[62] of behaviors are anticipated. Let us designate θ as the fractional coverage by blocking film: (1) When $R_o \gg \delta$, each active site functions independently from the others. The same voltammogram as with a bare electrode of surface area $(1-\theta)A_{geom}$ is observed. There will not be any apparent slowing down of the electron-transfer process, the effect of the film being only on the magnitude of the current heights. (2) When $R_o \approx \delta$, the voltammograms have the current heights smaller than the peak heights observed for a bare electrode. (3) When $R_o \ll \delta$, the diffusion layers of the various active sites intermingle. Provided $\theta \ll 1$, the cyclic voltammograms are the same as those obtaind with a geometric area A_{geom}, at which the apparent standard rate constant of electron transfer would be $K_{app,\,geom}(1-\theta)$. Two extreme

situations have been discussed so far, one in which the electrode is completely covered by a film which uniformly slows down the electron transfer, and the other where a completely blocking film is sprinkled with numerous and small active sites where electron transfer has the same rate as on the clean electrode. It is conceivable that the actual situation is between these two extremes. The larger the coverage, the slower the apparent electron transfer. Deviation from this quasi-reversible behavior should be observed when further increasing the coverage, resulting in a decrease of the current height and modification of the shape of the voltammograms, which then becomes of the polarogram type[63].

The behavior of a partially covered RDE is usually presented in terms of an attenuation factor ρ, defined as the ratio of the current obtained at a blocked electrode to that delivered by a uniformly active electrode of the same diameter, operating in the same conditions. According to Contamin and Levart's results[64], ρ does not depend on the angular velocity of the disk if radial diffusion can be neglected. Consequently, the plot of $\rho\omega^{1/2}$ as a function of $\omega^{1/2}$ will be represented for a partially covered RDE by a pseudo-Levich straight line with a slope depending on θ and the number of sites on the electrode surface, N,, tending to 1 for $N \rightarrow \infty$ when it becomes a true Levich line and to $1-\theta$ for $N \rightarrow 0$.

There are many experimental situations when a disk electrode exhibits nonuniform current density. This situation can arise because of electrode fouling by impurities or reaction products. Also, many electrochemical reactions are either catalyzed or inhibited by the presence of small amounts of oxide on the electrode surface. Spatial heterogeneity can be intentionally introduced, as is the case for electrodes doped with catalytic sites, such

as Bi(V)-doped PbO_2 film electrodes. This is also true of composite electrodes, where conducting particles are suspended in a nonconducting matrix. Examples of this type of electrode include the carbon-paste electrode and composite electrodes fabricated form mixtures of conducting particles and Kel-F polymer (polychlorotrifluoroethylene).

Landsberg and Thiele[65], using an electrical result of Smyth for the resistance between two disk electrodes of different radii separated by a distance R_o, established an approximate equation for the hydrodynamic current at a rotating disk array. The result is shown as

$$i = nFDC^b/(\delta + f(r_2,r_1,\delta)) \qquad [20]$$

where δ is the Levich diffusion layer thickness and f is a complex function of δ and the radii of the two disks. In this problem one views the smaller disk of radius r_1 as corresponding to a circular electroactive region and the larger disk radius r_2 as the half-distance (center to center) between microelectrodes. More recent work has been reviewed by Wipf and Wightman[66]. An array of microelectrodes has a well understood, if difficult to calculate, behavior.

The electrochemical response of the RDE is extremely difficult to calculate under conditions of nonuniform current density, since mass transport by convection and diffusion is no longer limited to the direction normal to the plane of the electrode. These calculations are much simpler if convection is eliminated. Therefore, chronoamperometry in quiescent solution is often used to characterize the dimensions of the active sites at spatially heterogeneous disk electrodes.

The chronoamperometric response at microelectrode ensembles is discussed here, although the results are also applicable to other examples of nonuniform current density. First, consider the chronoamperometric response at an individual microelectrode. At short times, the current at an inlaid microdisk electrode is given by Eqn. [21][67]

$$i_{lim} = nFDC^b(A/(\pi Dt)^{1/2} + P/2) \qquad [21]$$

$$P = 2\pi r$$

where P is the circumference of the electrode. The first term is the familiar Cottrell equation where diffusion is restricted to the direction normal to the electrode surface. The second term reflects the contribution to the total current from enhanced diffusion to the edge of the electrode, but is the source of the higher current densities that are observed at single microelectrodes and microelectrode ensembles. At long times, the current is given by Eqn. [22], and is equal to that at a hemispherical electrode with a radius of $2r/\pi$ for t $\rightarrow \infty$[67-69].

$$i_{lim} = 4nFC^bDr \qquad [22]$$

Equation [22] can be solved for the steady-state diffusion layer thickness (Eqn. [23])[48].

$$\delta = \pi r/4 \qquad [23]$$

The equivalence between the limiting currents at an inlaid microelectrode and at a hemispherical electrode demonstrate that the current is independent of the shape of the microelectrode when the diffusion layer is $\geq$ the dimensions of the electrode. For an inlaid microelectrode, short times (Eqn. [21] correspond to $t \ll r^2/D$, whereas long times (Eqns. [22] and [23]) correspond to $t \gg r^2/D$[67].

Equations [21]-[23] were derived for an isolated microelectrode, but also apply to a microelectrode ensemble where is no overlap of the diffusion layers for adjacent active sites. In this case, the total current is just the sum of the currents at each individual microelectrode , i.e., Eqns.[21] or [22] multiplied by the number of microelectrode elements. From Eqn. [23], one might expect that there would be no overlap of diffusion layers when the spacing between elements is larger than their diameter. However, it has been recommended that the elements be separated by at least 6 diameters to avoid diffusion layer overlap[70]. In the experimental limit that diffusion layer overlap is complete, the current is given by Eqn. [21], but the area term refers to the geometric area of the disk. This means that at long times, the microelectrode ensemble behaves as if the whole surface is active. The current at times intermediate between zero diffusion layer overlap and total diffusion layer overlap can be solved by digital simulations, and an empirical solution has been given[71]. Recently, an analytical solution was derived which was accurate within 5% of experimental data[29].

Chronoamperometric data at short times (Eqn. [21]) can be used to calculate the fractional active area and the total perimeter for a composite electrode. From inspection of Eqn. [21], higher current densities are expected for microelectrode ensembles that have a larger perimeter to area ratio. Thus, for electrodes with the same fractional active area, higher current densities are expected for the electrode with a larger number of smaller active sites.

Chronoamperometry is useful for determining active site sizes and separations, but

mass-transport properties are important since practical applications certainly involve convective conditions. The earliest solution for the current at a partially blocked RDE[65,72] predicted that curvature in both Levich plots ($i - \omega^{1/2}$) and Koutecky-Levich plots ($i^{-1} - \omega^{-1/2}$) would be observed when the distance between the active sites was comparable to the diffusion layer thickness.

This treatment was criticized[73] because it was based on a uniform diffusion layer thickness across the electrode surface. Alternate treatments have neglected mass-transport by radial diffusion[64,73], and concluded that the rotation rate dependence of the current would be equal to that of a uniformly accessible RDE of smaller geometric area. The response was characterized by an attenuation factor (ρ), which is the ratio of the current at a partially blocked RDE to the current at a uniformly accessible RDE of the same geometric area. It was concluded that ρ is independent of rotation rate when radial diffusion is negligible. Therefore, a linear relationship was predicted for both Levich plots (i-$\omega^{1/2}$) and Koutecky-Levich plots (i^{-1}-$\omega^{-/12}$).

Experimental results demonstrated that curvature can be observed for both Levich and Koutecky-Levich plots at an electrode poisoned by chemisorbed substances[74,75]. Recently, digital simulation was used to calculate the current at a partially blocked RDE as a function of rotation rate and fractional active area[76]. This calculation included terms for radial mass transport by both diffusion and convection, as well as diffusion and convection in the direction normal to the electrode surface. These calculations support the conclusion that the attenuation factor (ρ) is a function of rotation rate, i.e., both i-$\omega^{1/2}$ and

i^{-1}-$\omega^{-1/2}$ plots show significant deviation from linearity. These calculations also demonstrate that for electrodes with equal fractional areas, the current density was high for a RDE with a larger number of smaller active sites.

Qualitative results for disk electrodes under both stationary and convective (RDE) conditions demonstrate that a greater enhancement in current density is observed by maximizing the edge effect, i.e., for a larger number of smaller active sites. These results are given for electrodes with macroscopic inhomogeneities, i.e., active sites with r $\approx$ mm. It is interesting to speculate whether these trends can be extended to electrodes with microscopic inhomogeneities.

The research described in this dissertation focus on the synthesis and development of composite electrode materials by solid state chemistry and high temperature techniques. The characterization of these composite electrode materials has been examined by XRD, SEM-EDS, ESCA, voltammetry and amperometry.

References

1. H. Schafer, *Chemical Transport Reactions*, Academic Press, New York, ch.6, (1964).)

2. P. Jones and J. A. Hockey, *Trans. Faraday Soc.* **67**, 2679 (1971).

3. G. Munuera and F. S. Stone, *Disc. Faraday Soc.* **52**, 205 (1971).

4. J. B. Peri, *J. Phys. Chem.*, **69**, 220 (1965).

5. P. J. Anderson, R. F. Horlock and J. F. Oliver, *Trans. Faraday Soc.*, **61**, 2754

(1965).

6. W. A. Steele, *Adv. Colloid Interface Sci.*, **1**, 3 (1967).

7. K. Tanabe, T. Sumiyoshi, K. Shibata, T. Kiyoura and J. Kitagawa, *Bull. Chem. Soc. Jpn.*, **47**, 1064 (1974).

8. H. Nakabayashi, *Bull. Chem. Soc. Jpn.*, **65**, 914 (1992).

9. J. Lyklema, *J.Electroanal. Chem* **18** (1968) 341.

10. J. Lyklema, *Croat. Chem. Acta* **43** (1971) 249.

11. Th. F. tadros and J. Lyklema, *J.Electroanal. Chem* **17** (1968) 267.

12. A. J. Bard and L. R. Faulkner, *Electrochemical Methods*; Wiley: New York, NY, 1980.

13. C. M. A. Brett and A. M. C. F. O. Brett, *Comprehensive Chemical Kinetics*; C. H. Bamford, R. G. Compton, Eds.; Elsevier: New York, NY, 1986; Chapter 5, p 358.

14. F. G. Cottrell, *Z. Physik. Chem.* **42**, (1902) 385.

15. V. G. Levich,, *Physicochemical Hydrodynamics*, Prentice Hall: Englewood Cliffs, NJ, 1962; p 75.

16. D. P. Gregory and A. C. Riddiford, *J. Chem. Soc.* (1956), 3756-3764.

17. P. H. Rieger, *Electrochemistry*; prentice Hall: Englewood Cliffs, NJ, 1987; p 300.

18. D. Britz, *Digital Simulation in Electrochemistry*; Springer-Verlag: New York, NY, 1981.

19. S. W. Feldberg *Electroanalytical Chemistry*; A.J.Bard, Ed.; Marcel Dekker: New

York, NY, 1969; Vol.3, pp199-296.

20. R. Lines and V. D. Parker, Acta Chem. Scand. B31 (1977) 369.]

21. D. Pletcher, J. Appl. Electrochem. 14,403(1984).

22. M. Fleischmann, F. Laserre, J. Robinson and D. Swan, *J Electroanal. Chem.*, **177**, (1984) 97.

23. M. Fleischmann, F. Laserre, J. Robinson and D. Swan, *J Electroanal. Chem.*, **177**, (1984)115.

24. B. R. Scharifker and G. J. Hills, *J Electroanal. Chem.*, **130**, (1981) 81.

25. R. M. Wightman, *Anal.Chem.*, **53** (1981) 1125A.

26. H. Reller, E. Kirowa-Eisner and E. Gileadi, *J. Electroanal. Chem.*. **138** (1982) 65.

27. R. C. Paciej, G. L. Cahen,Jr., G. E. Stoner and E. Gileadi, *J. Electrochem.Soc.* **138** (1985) 1307.

28. M. Ciszkowska and Z. Stojek, *J. Electroanal. Chem.* **191** (1985) 101.

29. B. R. Scharifker, *J Electroanal. Chem.*, **240**, (1988) 61.

30. W. Thormann, P. van den Bosch, and A. M. Bond, *Anal. Chem.* **57** (1985) 2764.

31. A. J. Bard, J. A. Crayston, G. P. Kittlesen, T. V. Shea, and M. S. Wrighton, *Anal. Chem.* **58** (1986) 2321.

32. M. DeAbreu and W. C. purdy, *Anal. Chem.* **59** (1987) 204]

33. L. E. Fosdick, J. L. Anderson, T. A. Baginski, and R. C. Jaeger, *Anal. Chem.* **58** (1986) 2750.

34. K. Aoki and M. Tanaka, *J. Electroanal. Chem.* **266** (1989) 11.

35. K. Aoki and J. Osteryoung, *J. Electroanal. Chem.* **122** (1981) 19.

36. T. Hepel and J. Osteryoung, *J. Electrochem.Soc.* **133** (1986) 752

37. R. N. Adams, *Anal. Chem.* **30** (1958) 1576.

38. R. J. Nowak, C. L. Joyal, and D. C. Weber, *J. Electroanal. Chem.*. **143** (1983) 413.

39. N. D. Danielson, J. Wangsa, and M. A. Targove, *Anal. Chem.* **61** (1989) 2585]

40. J. E. Anderson and D. E. Tallman, *Anal. Chem.* **48** (1976) 209.

41. R. C. Engstrom, M. Weber and J. Werth, *Anal. Chem.* **57** (1985) 933

42. J. Wang, T. Golden, K. Varughese and I. EL-Rayes, *Anal. Chem.* **61** (1989) 508.

43. S. M. Lipka, G. L. Gahen,Jr., G. E. Stoner, L. L. Scribner,Jr., and E. Gileadi, *J. Electrochem.Soc.* **135** (1988) 368.

44. G. Nagy, Zs. Feher, and E. Pungor, *Anal. Chim. Acta*, **52** (1970) 47.

45. J. Park and B. R. Shaw, *Anal. Chem.* **61** (1989) 848.

46. K. E. Creasy and B. R. Shaw, *Anal. Chem.* **61** (1989) 1460.

47. R. N. Adams, *Electrochemistry at solid Electrodes,* Dekker, New York, 1969, pp.278-280.

48. N. Sleszynski, J. Osteryoung, and M. Carter, *Anal. Chem.* **56** (1984) 130.

49. B. K. Davis, S. G. Weber, and A. P. Sylwester, *Anal. Chem.* **62** (1990) 1000.

50. R. M. Penner, and C. R. Martin, *Anal. Chem.* **59** (1987) 2625.

51. I. F. Cheng, L. D. Whiteley and C. R. Martin, *Anal. Chem.* **61** (1989) 762.

52. M. Mascini, F. Pallozzi, and A. Liberti, *Anal. Chim. Acta*, **64** (1973) 126.

53. L. N. Klatt, D. R. Connell, R. E. Adams, I. L. Honigberg, and J. C. Price, *Anal. Chem.* **47** (1975) 2470.

54. J. E. Anderson, D. E. Tallman, D. J. Chesney, and J. L. Anderson, *Anal. Chem.* **50** (1978) 1051.

55. D. E. Weisshaar and D. E. Tallmen, *Anal. Chem.* **55** (1983) 1146.

56. D. E. Tallmen and D. E. Weisshaar, *J. Liq. Chromatogr.* **6**, (1983) 2157.

57. S. L. Peterson and D. E. Tallmen, *Anal. Chem.* **60** (1988)82.

58. S. L. Peterson and D. E. Tallmen, *Anal. Chem.* **62** (1990) 459.

59. P. J. S. Ewen and J. M. Robertson, *J. Phys. D., Appl. Phys.* **14** (1981) 2253.

60. S. L. Peterson, D. E. Tallmen, G. Shepherd, and W. J. MacKellar, *J. Electroanal. Chem.*. **261** (1989) 249.

61. S. L. Peterson, D. E. Weisshaar, D. E. Tallmen, R. K. Schulze, J. F. Evans, S. E. Desjarlais, and R. C. Engstrom, *Anal. Chem.* **60** (1988)2385.

62. C. Amatore, J. M. Saveant and D. Tessier, *J. Electroanal. Chem.* **146** (1983) 37.

63. C. Amatore, J. M. Saveant and D. Tessier, *J. Electroanal. Chem.* **147** (1983) 39.

64. O. Contamin and E. Levart, *J. Electroanal. Chem.* **136** (1982) 259.

65. R. Landsberg and R. Thiele, *Electrochim. Acta* **11**, (1966) 1243.

66. R. M. Wightman and D. O. Wipf, In *Electroanalytic Chemistry*; Bard A. J., Ed.; Dekker: New York, 1988.

67. K. B. Oldham *J. Electroanal. Chem.*. **122** (1981) 1.

68. J. Newman, *J. Electroanal. Chem.*. **113** (1966) 501.

69. K. Aoki and J. Osteryoung, *J. Electroanal. Chem.* **125** (1981) 315.

70. W. L. Caudill, J. O. Howell and R. M. Wightman, *Anal. Chem.* **54** (1982) 2532.

71. D. Shoup, A. Szabo, *J Electroanal. Chem.*, **160**, (1984) 19.

72. F. Scheller, S. Muller, R. Landsberg, H.-J. Spitzer *J Electroanal. Chem.*, **19**, (1968). 187.

73. V. Yu. Filinovsky *Electrochim. Acta* **25**, (1980) 309.

74. A. M. Trukhan, Yu. M. Povarov and P. D. Lukovtsev, *Elektrokhimiya* **6**, (1970) 425.

75. Yu. M. Povarov and P. D. Lukovtsev *Electrochim. Acta* **18**, (1973) 13.

76. E.Levart, *J.Electroanal. Chem* **187** (1985) 247.

SYNTHESIS AND CHARACTERIZATION OF RU-TI_4O_7 MICROELECTRODE ARRAYS

A paper published in the *J. Electrochem Soc.*, **141**, (1994) 1014.

Lin He, Hugo F. Franzen, Joseph E. Vitt and Dennis C. Johnson

Abstract

A synthesis is described for Ru microelectrode arrays within a conductive Ti_4O_7 ceramic matrix. Data obtained by X-ray diffractometry and scanning electron microscopy are consistent with the existence of heterogeneous mixtures of Ru particles (*ca.* 0.8 μm dia.) within the Ti_4O_7 matrices. No mixed metal oxides or other new compounds are detected. Rotated disk electrodes (RDEs) constructed from the Ru-Ti_4O_7 materials are compared on the basis of their voltammetric response for the oxidations of I^- to I_2 and IO_3^- in 0.10 M H_2SO_4. These results are rationalized on the basis of microelectrode arrays, *i.e.*, elevated current densities and diminished sensitivity to changes in rotational velocity as compared to a solid Ru RDE. A RDE constructed from Ru-Ti_4O_7 containing *ca.* 0.5% Ru by volume exhibits virtually zero dependence on rotational velocity for the oxidation of I^- to I_2 and, therefore, this material is concluded to function virtually as an ideal microelectrode array.

Introduction

Microelectrode arrays consist of numerous small (micro-scale) electrodes organized into a regular pattern (array) within the surface of an electrochemically inert matrix. The inert material fulfills the functions of (i) providing mechanical stability for the array, (ii) defining the fluid dynamical properties of the array, and (iii) assuring electrical correspondence between the microelectrodes. Microelectrodes organized in planar arrays have received considerable attention among electrochemists because of a significant enhancement in the current density (coul s^{-1} cm^{-2}) observed at single microelectrodes in comparison to electrodes of the same material having large geometries. [1-4] Enhancement of current densities at microelectrodes in planar arrays is expected because the hemispherical diffusional transport of electroactive species to individual microelectrodes results in a flux density (mol s^{-1} cm^{-2}) that is significantly larger than would exist if the planar surface was uniformly reactive.

The amperometric response of microelectrode arrays can be characterized by the relative current density (*J*) defined as the true current density at the collective microelectrodes of the array normalized with respect to the current density at a solid electrode of large geometry:

$$J = \frac{(i/A_{act})_{array}}{(i/A_{geom})_{solid}} \qquad [1]$$

In effect, according to Equation 1, the ratio of signal-to-background current densities (*S/B*) are enhanced by the factor *J* at array electrodes, in comparison to solid electrodes, when

the background current is proportional to the total area of the active region(s) of the electrodes.

The amperometric response at microelectrode arrays also has been characterized by a so-called "attenuation factor" (ρ) defined as the apparent current density at the array normalized with respect to the current density for a solid electrode of large geometry:

$$\rho = \frac{(i/A_{geom})_{array}}{(i/A_{geom})_{solid}} \qquad [2]$$

Hence, from Equations 1 and 2, values of J and ρ are related according to:

$$\rho = J(1 - \theta) \qquad [3]$$

where θ has been called a "blocking factor" [1,5,6] in analogy with partially fouled electrode surfaces, and the quantity $\rho/J = 1 - \theta$ is the ratio of the active and geometric areas (A_{act}/A_{geom}).

The effect of change in rotational velocity (ω) for disk electrodes constructed from microelectrode arrays can be predicted easily for two limiting conditions. For low density arrays ($\theta \rightarrow 1$) with active sites that behave as isolated and ideal microelectrodes, current is expected to be independent of ω. However, because the transport-limited current at a solid RDE is proportional to $\omega^{1/2}$, [7] J and ρ are expected to be proportional to $\omega^{-1/2}$ for ideal microelectrode arrays. For high density arrays ($\theta \rightarrow 0$), the diffusion zones of adjacent active sites overlap extensively and, in the limit of total overlap of diffusion zones, the corresponding array electrodes have a virtually uniform diffusion-layer thickness across the face of the electrode and the current is proportional to $\omega^{1/2}$. Hence, for these high density

array electrodes, J and ρ are expected to be independent of changes in ω. These conclusions are consistent with predictions based on models which neglect the effect of radial mass transport.[1,6,8] For microelectrode arrays of intermediate density ($0 \ll \theta \ll 1$), J and ρ are expected to be complex functions of ω.

Microelectrode arrays have been fabricated commonly with the use of inert polymeric materials, *e.g.*, Kel-F, to bind the microelectrode particles into physically stable arrangements.[2-4] However, to achieve the optimal fractional active area of *ca.* $\leq 1.7\%$, as predicted by Weber for microelectrode arrays,[9] it has been necessary to incorporate graphite particles within the plastic matrices to achieve electrical connectivity between the microelectrodes. In a recent study of these so-called "Kelgraf electrodes" containing small Au particles,[4] current densities were more than 10 times larger in comparison to those for pure Au electrodes of large geometry. However, two major disadvantages were recognized when using graphitic powder in the fabrication of these composite electrodes.[4] First, loss of graphite occurred at the surface when the composite materials were subjected to mechanical polishing. Hence, it is apparent that some metal particles can be lost and there can be a sacrifice in electrical connectivity between the remaining metal particles. Second, graphite is a useful electrode material for many faradaic reactions and, therefore, its use is undesirable in the fabrication of metal microelectrode arrays.

We speculate that significant advantage can result from fabrication of microelectrode arrays using matrices (binders) that are both electrically conductive and electrochemically inert. Among the list of possibilities, Ti_4O_7 is an attractive candidate. This ceramic

material is a member of the Magneli phases (Ti_nO_{2n-1}), has a high conductivity (*ca.* 10^3 Ω^{-1} cm^{-1}), and is very stabile in a variety of corrosive media. [10,11] Furthermore, the desired electrochemical inertness of Ti_4O_7 is indicated by the large values of overpotential reported for anodic and cathodic evolution of O_2 and H_2, respectively, in aqueous media. [10,11] Possible applications of Ti_4O_7 in electrolytic processes have been described in reviews [10,11] and patents [12,13].

Research described here is part of a larger project to synthesize composite electrode materials using a minimum of precious metals distributed as microelectrodes within electrically conductive but electrochemically inert matrices. Here we report on the generation of Ru microelectrodes within conductive Ti_4O_7 matrices. X-ray diffraction and scanning electron micrographic data are presented along with voltammetric results for the oxidations of I^- to I_2 and IO_3^- in 0.10 M H_2SO_4.

Experimental

Reagents.—The potassium iodide was a reagent grade chemical (Fisher) and the water was purified in a Milli-Q system (Millipore) after passage through two D-45 deionizing tanks (Culligan). The solutions of 0.10 M H_2SO_4 were prepared by dilution of the concentrated reagent grade chemical (Mallinckrodt) in deionized water.

Electrode fabrication.—The Ru-Ti_4O_7 materials were prepared by mixing the appropriate quantities of TiO_2 (Fisher), Ti_2O_3 (Alpha, Johnson Matthey), and Ru (Morton Thiokol). Each mixture was ground in an alumina mortar until a uniform color was

obtained. Several drops of polyvinyl acetate (1% by vol.) in ethanol were added to the mixture to produce a paste which was pressed into a cylindrical pellet (9-mm dia., 15-mm length) in a laboratory press (Carve) at a pressure of 3 tons cm^{-2}. Pelletization improved contact between particles and, thereby, increased diffusion rates during thermal processing.

The pellets were dried at 150 °C for 1 day and then placed in a tungsten Knudsen cell in an induction furnace. The temperature of the tungsten crucible was monitored using an optical pyrometer. The residual pressure in the furnace was lowered to $< 10^{-5}$ torr using an oil-diffusion pump backed by a mechanical pump. The temperature was then slowly increased to 800 °C and held constant for *ca.* 1 hr to evaporate the all traces of organic material. The temperature was then slowly increased to 1300 °C, under a vacuum of *ca.* 10^{-6} torr, and held constant for 5 hr. Heating was terminated and the sample quenched by radiative heat loss in vacuum, allowing the sample to reach room temperature in *ca.* 2.5 hr.

Disk electrodes were assembled by mounting thermally processed pellets into a metal socket at the end of a stainless steel shaft which could be inserted into the rotor assembly of an ASR rotator. Cylindrical surfaces of these pellets were wrapped with Teflon tape to prevent their contact with the aqueous test solutions and, furthermore, only the end (disk) surfaces were allowed to contact solutions during use.

Active surface areas (A_{act}) for Ru-Ti_4O_7 electrodes were calculated from the geometric areas (A_{geom}) and the volume fractions of Ru according to:

$$A_{act} = [V_R/(V_R + V_T)]A_{geom} \simeq [V_R/V_T]A_{geom} \quad (\text{for } V_R \ll V_T)$$

$$= (d_T/d_R)(M_R/M_T)(N_R/N_T)A_{geom}$$

$$= 0.1(N_R/N_T)A_{geom} \quad [4]$$

where V, d, M and N represent the volume, density, molecule weight, and number of moles, respectively; and the subscripts R and T designate Ru and Ti_4O_7, respectively.

X-ray diffractometry.—X-ray diffraction (XRD) data were obtained with a model FR552 Guinier camera (Enraf-Nonius) using Cu $K\alpha_1$ radiation (λ = 1.5406 Å). A small amount of well-ground sample was mixed with SRM 640 silicon (NIST) as an internal standard and mounted on a sample holder using Scotch^R tape (3M). The sample was rotated during data collection to reduce effects of preferred orientation and data were collected for a 2-hr period.

Microscopy.—Micrographs and elemental analyses were obtained using a S-200 scanning electron microscope (SEM; Cambridge) equipped with a thin-window energy dispersive spectrometer (EDS; Tracor Northern).

Voltammetry.—Voltammetric data were obtained using a RDE4 potentiostat and ASR rotator (Pine Instrument) interfaced with a 386 computer (Apex) by a DT2801-A interface (Data Translation) using ASYST-3.1 software (Keithley-ASYST). The electrochemical cell was constructed from Pyrex with porous glass disks separating the working, reference and counter electrode compartments. All potentials are reported in volts *vs.* a saturated calomel electrode (SCE; Fisher Scientific). The counter electrode was a coiled Pt wire (*ca.* 7.6 cm^2).

The mass transport-limited current at a uniformly accessible RDE (θ = 0) is a linear

function of $\omega^{1/2}$ [7] and observation of negative deviation from linearity in i-$\omega^{1/2}$ plots is indicative of faradaic reactions under mixed control by mass-transport and kinetic processes. Data of this type are often plotted as i^{-1} *vs.* $\omega^{-1/2}$ according to: [7]

$$i^{-1} = (nFA_{geom}k_{app}C^b)^{-1} + (cnFA_{geom}D^{2/3}\nu^{-1/6}C^b\omega^{1/2})^{-1} \quad [5]$$

where $c = 0.554/(0.8934+0.316(D/\nu)^{0.36})$, A_{geom} is the geometric area (cm^2), ν is the solution kinematic viscosity ($cm^2\ s^{-1}$), k_{app} is the apparent heterogeneous rate constant ($cm\ s^{-1}$), and n, F and C^b have their usual electrochemical significance. The plot of i^{-1} *vs.* $\omega^{-1/2}$ for a reaction under mixed control at a RDE with $\theta = 0$ is linear with a slope proportional to n^{-1} and intercept proportional to k_{app}^{-1}.

Values of n for electrochemical processes were estimated on the basis of the differential form of Equation 5 written as:

$$\Delta i^{-1}/\Delta\omega^{-1/2} = (cnFA_{geom}D^{2/3}\nu^{-1/6}C^b)^{-1} \quad [6]$$

where $\Delta i^{-1} = i_2^{-1} - i_1^{-1}$ is the difference between the reciprocal currents measured at ω_2 and ω_1, respectively, and $\Delta\omega^{-1/2} = \omega_2^{-1/2} - \omega_1^{-1/2}$. According to Equation 6, the ratio $\Delta i^{-1}/\Delta\omega^{-1/2}$ is expected to be independent of k_{app}.

Results and discussion

XRD and SEM data.—Figure 1A contains the XRD pattern for pure Ru metal. [14] Figure 1B contains the XRD pattern of Ti_4O_7 prepared by the method described but in the absence of Ru. This diffraction pattern is in good agreement with that reported for a single Ti_4O_7 crystal by Le Page and Marezie. [15] Figures 1C - 1F contain XRD patterns for Ti_4O_7

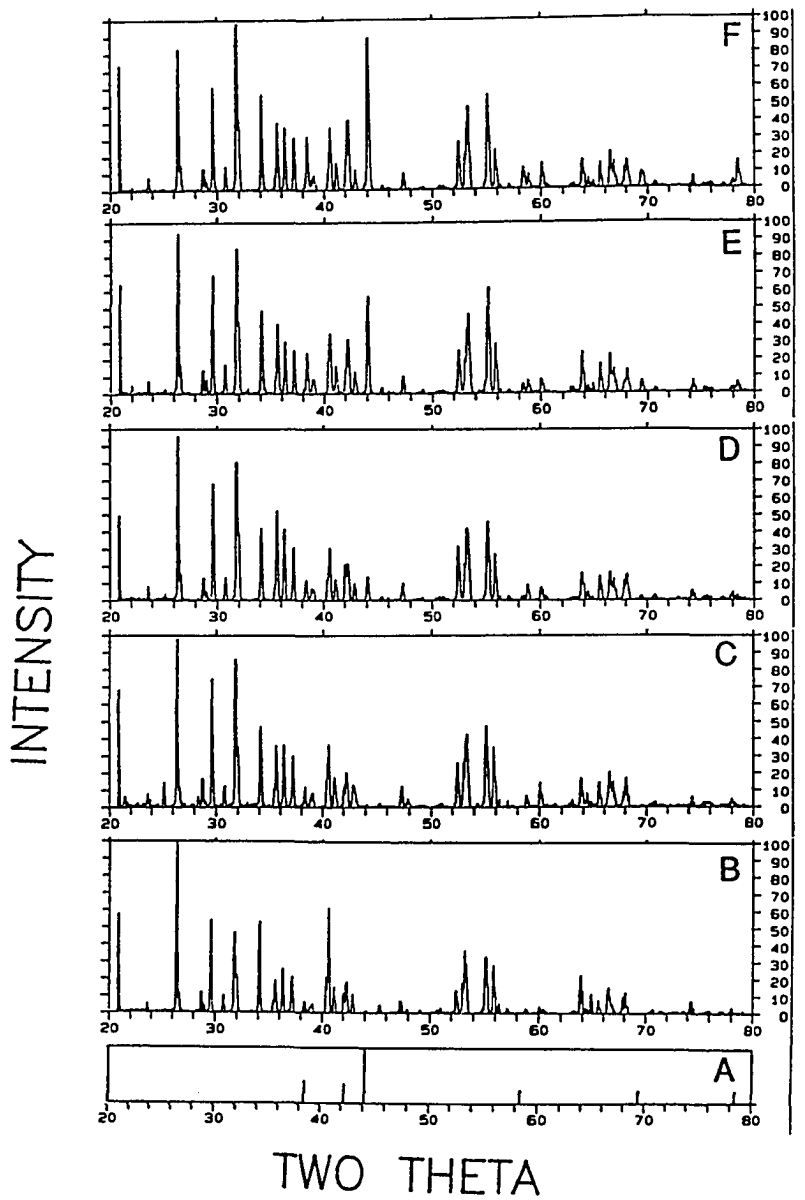

Figure 1. X-ray powder diffraction patterns. Materials: (A) Ru, (B) Ti_4O_7, (C) 0.1% Ru-Ti_4O_7, (D) 1% Ru-Ti_4O_7, (E) 3% Ru-Ti_4O_7, (F) 5% Ru-Ti_4O_7.

samples containing various amounts of Ru. These patterns correspond exactly to combinations of the patterns in Figures 1A & 1B which indicates these samples correspond to heterogeneous mixtures of pure Ru and Ti_4O_7, and there is no evidence that new compounds are formed in which Ru is incorporated within the Ti_4O_7 lattice. Hence, on this basis, it is expected that the Ru is distributed throughout the Ti_4O_7 matrices in the form of small metallic particles, *i.e.*, microelectrodes. A very small diffraction peak exists in Figure 1C corresponding to TiO_2 ($I4_1/amd$) and it is apparent that a small quantity of this oxide existed in this sample of Ti_4O_7 containing 0.1% by volume of Ru. The average grain size in the samples was estimated on the basis of the Fresnel Construction [16] and determined to be on the order of 0.4 μm.

Planar surfaces of electrodes were examined using SEM and typical micrographs are shown in Figures 2A - 2E as a function of increasing Ru content. The existence of porosity is evident for all samples with the average pore diameters estimated to increase with increasing Ru content from *ca.* 0.5 μm for pure Ti_4O_7 (Fig. 2A) to *ca.* 10 μm for 5% Ru-Ti_4O_7 (Fig. 2D). SEM-EDS applied to the surfaces shown in Figure 2D & 2E revealed that only a small fraction of the bright spots in these micrographs correspond to discreet Ru particles. The EDS spectrum was obtained for the spot designated by the arrow in Figure 2E for 5% Ru-Ti_4O_7-Ru and the result is shown in Figure 3. The average diameter for the Ru particles was estimated to be *ca.* 0.8 μM from SEM-EDS data, which is in acceptable agreement with estimates from XRD data. Distances between nearest Ru particles exceed the dimensions of Figure 2E (*i.e.*, $>$ 15 μm).

(a) Ti_4O_7

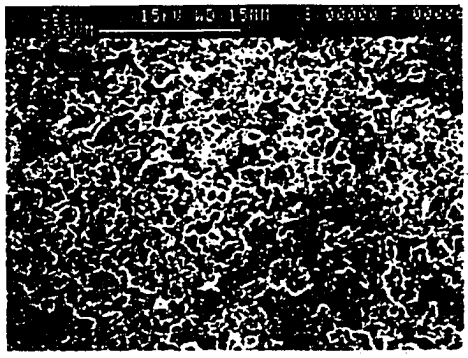

(b) 0.1% Ru-Ti_4O_7

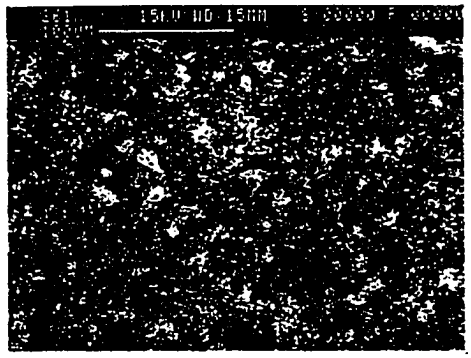

(c) 1% Ru-Ti_4O_7

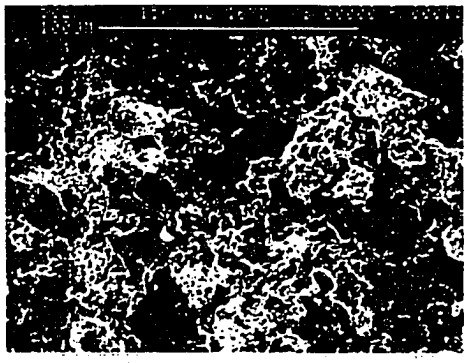

(d) 5% Ru-Ti_4O_7

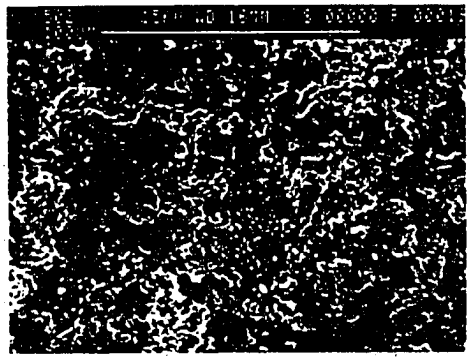

(e) 5% Ru-Ti_4O_7

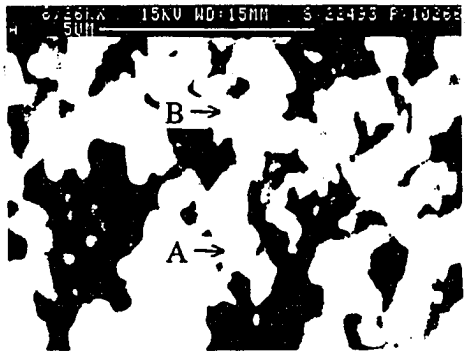

Figure 2. Micrographs of Ru-Ti_4O_7 electrode surfaces. Ru content and distance indicated by bar: (A) 0%, 100μm; (B) 0.1%, 100μm; (C) 1%, 100μm; (D) 5%, 100μm; (E) 5%, 5μm.

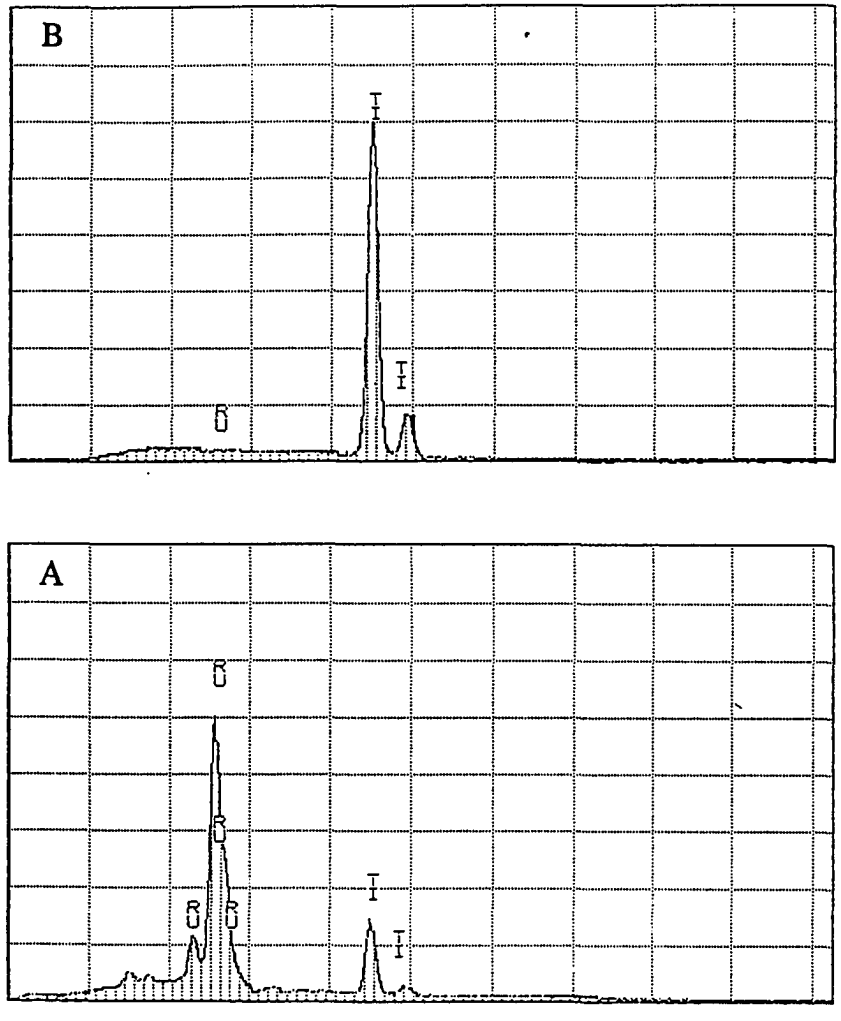

Figure 3. EDS spectra for regions identified in Figure 2E.

Voltammetric results.— Iodide was chosen as a model reactant for the voltammetric characterization of these electrode materials because two major anodic reactions have been reported for iodide at noble metals electrodes in acidic media. The first reaction is the oxidation of I^- to I_2 (1 eq mol^{-1}) by a quasi-reversible process with $E_{1/2}$ = *ca.* 0.5 V at Ru, Pt, Au, Ir, and glassy carbon (GC) electrodes in acidic media. The second reaction is the oxidation of I^- to IO_3^- (6 eq mol^{-1}) by an irreversible process that requires the concomitant anodic discharge of H_2O. [17] Hence, the anodic wave for production of IO_3^- occurs with a variable $E_{1/2}$ that is dependent on the overpotential for discharge of H_2O at the electrode under consideration. [17]

Representative voltammetric data (*i-E*) are shown in Figure 4 for 5.0 mM I^- in 0.10 M H_2SO_4. Curves **a** and **b** correspond to the residual response in the absence of I^- for the Ti_4O_7 and 4% Ru-Ti_4O_7 RDEs, respectively; whereas Curves **c** and **d** correspond to the response for 5.0 mM I^- at the Ti_4O_7 and 4% Ru-Ti_4O_7 RDEs, respectively. Clearly, there is no appreciable difference between Curves **a** and **c** which indicates the absence of any electrochemical reaction involving I^- at the pure Ti_4O_7 electrode. The residual response for the Ru-Ti_4O_7 RDE is significantly different from that for the Ti_4O_7 RDE. Most obvious is the large difference in the potential for onset of solvent breakdown observed for this current sensitivity, *i.e.*, *ca.* 1.1 V for Ru-Ti_4O_7 as compared to *ca.* 2.5 V for Ti_4O_7. Furthermore, the residual current at *ca.* 1.0 V, whether obtained for the positive or negative scans, is much larger for Ru-Ti_4O_7 (curve **b**) in comparison to Ti_4O_7 (curve **a**). We speculate that the explanation is related to the larger apparent porosity for Ru-Ti_4O_7 which results in a

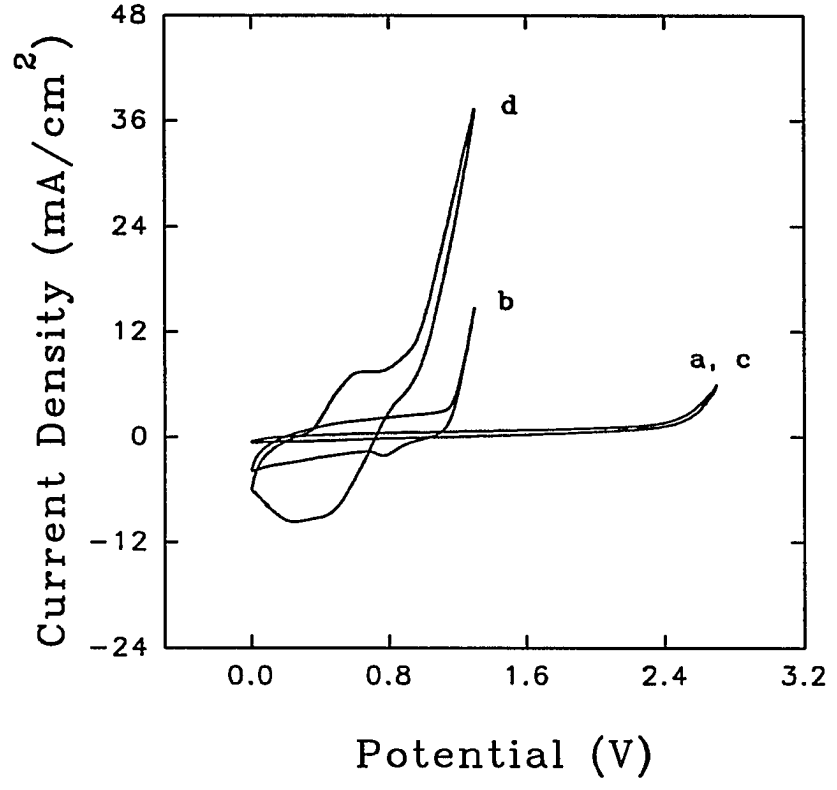

Figure 4. Voltammetric response for I^- at Ti_4O_7 and 4% Ru-Ti_4O_7 rotated disk electrodes. Scan rate: 30 mV s^{-1}. Scan range: 0.0 to 1.3 V. Rotational velocity: 261.7 rad s^{-1}. Electrodes: (a,c) Ti_4O_7, (b,d) 4% Ru-Ti_4O_7. Concentration of I^- (mM): (a,b) 0, (c,d) 5.0.

larger total surface area exposed to the supporting electrolyte.

Figures 5A and 5B contain voltammetric data obtained at the solid Ru RDE (A) and the 4% Ru-Ti_4O_7 RDE (B) in the absence (Curves **a** and **c**) and presence (Curves **b** and **d**) of 5.0 mM I^-. In the residual response (Curves **a** and **c**), the observed currents in the region 0.0 to 1.1 V are believed to be exclusively the result of the double-layer charging process, whereas the rapidly rising current for $E >$ *ca.* 1.1 V is from the anodic discharge of H_2O with concomitant evolution of O_2. The large magnitude of the charging current in curve **c**, as compared with curve **a**, indicates that the Ru-Ti_4O_7 RDE has a much greater porosity with a larger surface area exposed to the aqueous solution. This is consistent with the conclusion based on SEM data in Figures 2A - 2E that pore size increases with increasing Ru content.

Anodic waves are visible during the positive scans in Figure 5A and 5B for both electrodes that are concluded to correspond to the oxidation of I^- to I_2: $E_{1/2}$ = *ca.* 0.45 V for Ru (A) and *ca.* 0.47 V for 4% Ru-i_4O_7 (B). The second anodic wave, observed for both electrodes at $E >$ 0.9 V, is tentatively concluded to correspond to the oxidation of I^- to IO_3^-. This second wave does not exhibit a clear limiting-current plateau, probably partly because of the contribution from the concurrent anodic discharge of H_2O which increases rapidly with increasing potential. The importance of the anodic discharge of H_2O in the mechanism for oxidation of I^- to IO_3^- has already been discussed.[17] From the response for Ru in Figure 5A, we estimate $E_{1/2}$ = *ca.* 1.05 V for oxidation of I^- to IO_3^- at Ru in this media.

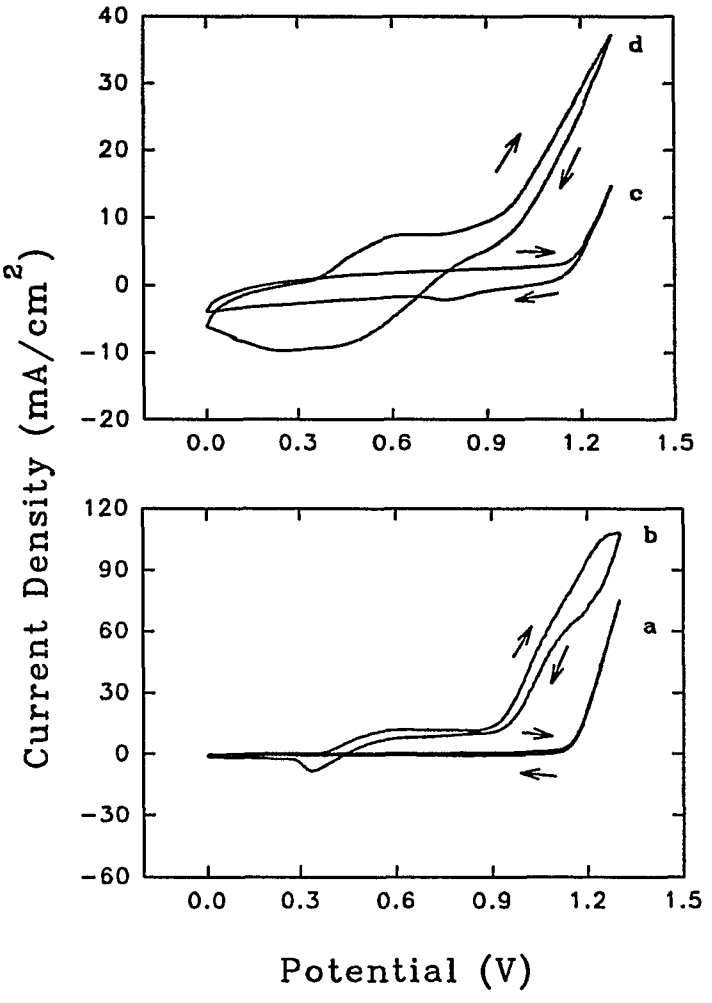

Figure 5. Voltammetric response for I^- at Ru (A) and 4% Ru-Ti_4O_7 (B) rotated disk electrodes. A_{geom}: 0.741 cm^2. Scan rate: 30 mV s^{-1}. Rotational velocity: 261.7 rad s^{-1}. Concentration of I^- (mM): (a,c) 0, (b,d) 5.0.

This tentative conclusion regarding the identities of the two anodic waves shown in Figure 5A and 5B was tested on the basis of values of $\Delta i^{-1}/\Delta\omega^{-1/2}$ (see Eqn. 6) measured at 0.62 and 1.18 V in the *i-E* curves (pos. scan) recorded for ω = 376.8 and 94.2 rad s^{-1} at the Ru RDE for 5.0 mM I^- (Fig. 5A, Curve **b**). These potential values are estimated to correspond to the transport-limited currents for the two anodic processes involving I^- and, hence, the quotient $(\Delta i^{-1}/\Delta\omega^{1/2})_{0.62V}/(\Delta i^{-1}/\Delta\omega^{1/2})_{1.18V}$ is expected to represent the ratio of the numbers of electrons for the two reactions (*i.e.*, $n_{1.18V}/n_{0.62V}$). The experimental value of $n_{1.18V}/n_{0.62V}$ was determined to be 5.6 which we consider to be in satisfactory agreement with the theoretical value of 6.0 based on the assumption that the oxidation products at 0.62 and 1.18 V are I_2 and IO_3^-, respectively. It should be noted that this method of calculation is expected to eliminate contributions from the anodic discharge of H_2O because this process is not influenced by changes in ω.

The cathodic peak observed at E_{peak} = 0.35 V during the negative scan at the Ru RDE (Fig. 5A, curve **b**) was determined to increase approximately as linear functions of I^- concentration and $\omega^{1/2}$ for C^b = 1 - 3 mM and ω = 10.5 - 94.2 rad s^{-1}. Therefore, by analogy with similar phenomena at Pt RDEs, [18] this peak is attributed to the cathodic stripping of adsorbed I_2 from the Ru surface. The broader cathodic peak observed during the negative scan at the Ru-Ti_4O_7 RDE (Fig. 5B, curve **d**) is tentatively concluded to result from overlap of the two cathodic peaks for (i) cathodic stripping of I_2 adsorbed on Ru microelectrodes and (ii) reduction of I_2 trapped within surface pores at Ru microelectrodes inside the pores. Trapped I_2 can originate from the oxidation of I^- to I_2 and homogeneous

reaction of I^- with IO_3^-.

Figure 6 contains typical *i-E* curves (pos. scan) obtained at the 4% Ru-Ti_4O_7 RDE as a function of I^- concentration. Clearly, both anodic waves increase with increasing I^- concentration. The plot of $i_{0.62V}$ *vs.* C^b was determined to be linear ($r^2 = 0.9985$, N = 5) for C^b = 0.5 - 5 mM. As is apparent from Figure 6, evidence for a transport-limited current for the oxidation of I^- to IO_3^- in the region $E > 1.0$ V becomes increasingly obscure as C^b is increased. Similar behavior is observed with increases in ω at constant C^b (data not shown). These observations are believed to be a consequence of the complex nature of the heterogeneous mechanism for this reaction and that, for large I^- flux, the reaction rate tends to become limited by the rate of discharge of H_2O to generate the oxygen species required by the anodic O-transfer reaction.

Dependence of Amperometric Response on Electrode Composition.— Figure 7 contains plots of i/A_{geom} *vs.* $\omega^{1/2}$ corresponding to the oxidation of I^- to I_2 (0.62 V) for the solid Ru RDE (Curve **a**) and various Ru-Ti_4O_7 RDEs (Curves **b** - **d**). Curve **a** is virtually linear with a near-zero intercept, as expected for transport-limited reactions at a solid RDE (*i.e.*, $A_{act} \simeq A_{geom}$). In sharp contrast, i/A_{geom} is virtually independent of $\omega^{1/2}$ for the 0.5% Ru-Ti_4O_7 RDE (Curve **b**) which is an indication that this electrode behaves virtually as an ideal microelectrode array. The response for the 1% and 5% Ru-Ti_4O_7 RDEs (Curves **c** & **d**) is more complex and indicates some overlap of the diffusional zones for adjacent microelectrodes in these RDEs, especially at low ω values. Figure 8 contains plots of i/A_{geom} *vs.* $\omega^{1/2}$ corresponding to the oxidation of I^- to IO_3^- (1.18 V). As in Figure 7, the

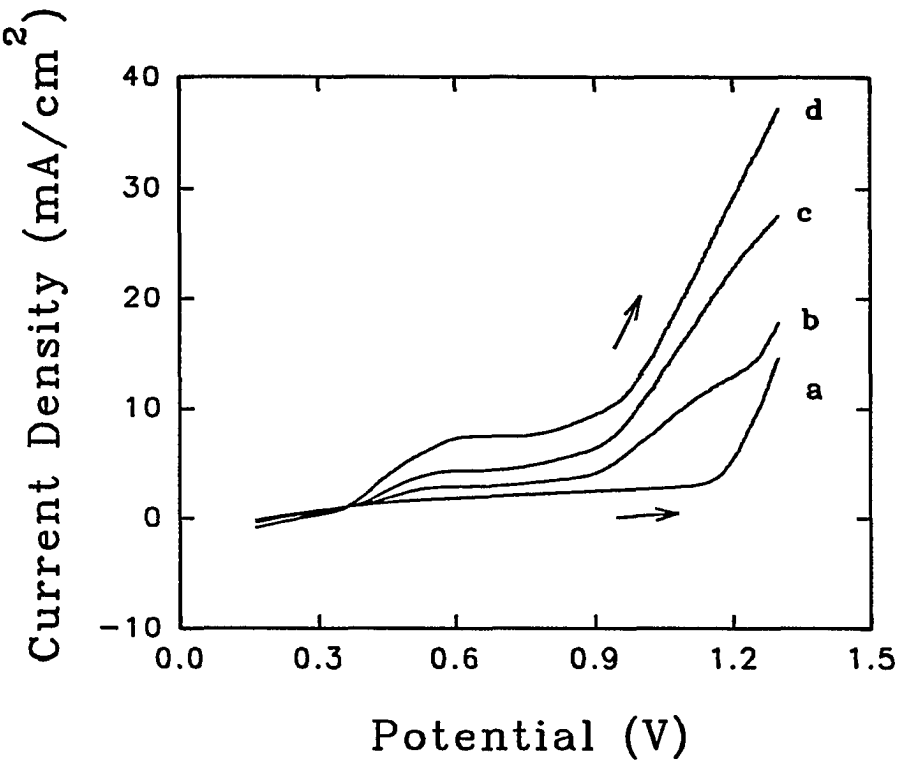

Figure 6. Voltammetric response as a function of I^- concentration at the 4% Ru-Ti_4O_7 rotated disk electrode. Rotational velocity: 261.7 rad s^{-1}. Scan rate: 30 mV s^{-1}. Concentration of I^- (mM): (a) 0, (b) 1.0, (c) 2.5, (d) 5.0.

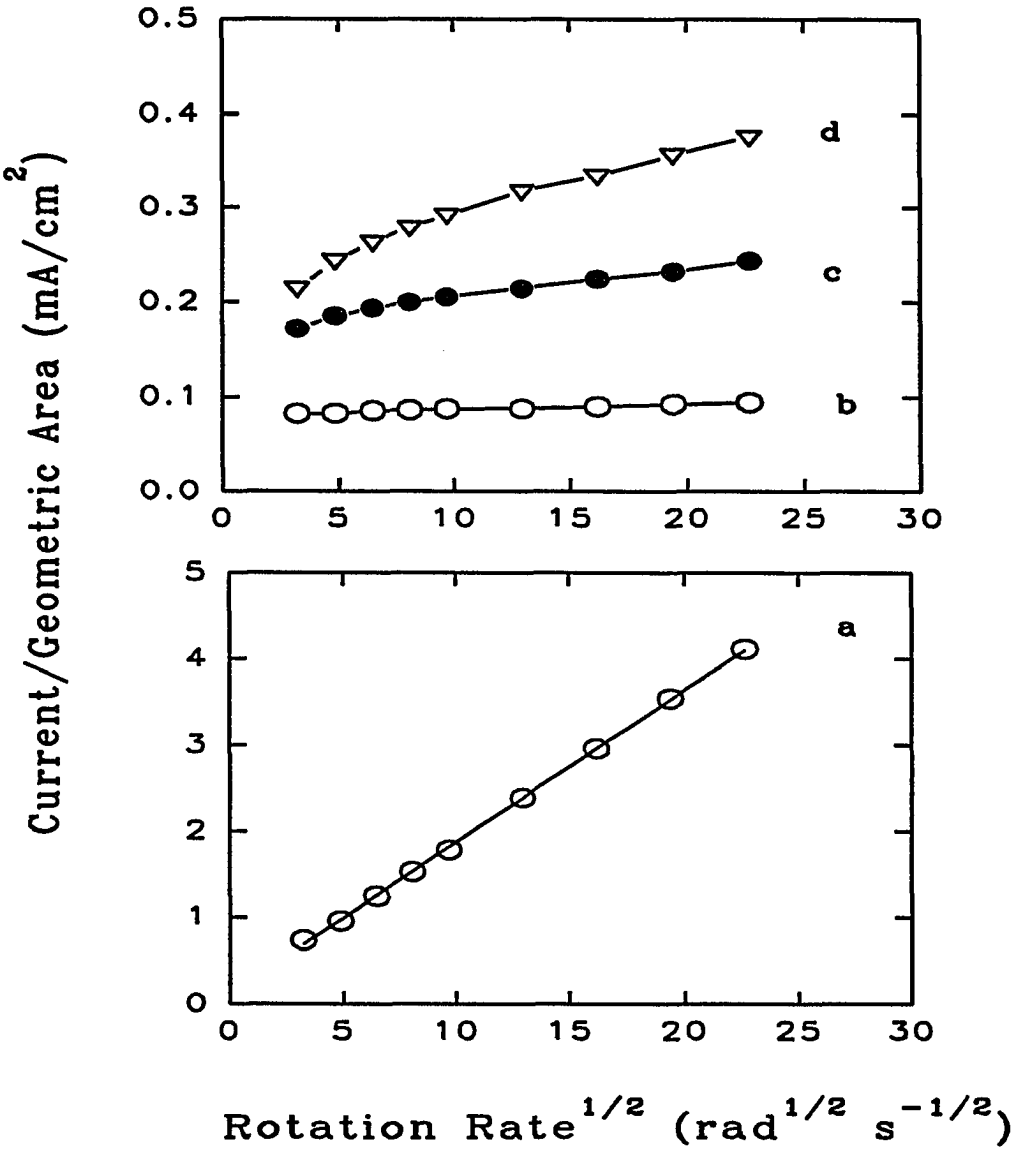

Figure 7. Plots of apparent current density *vs.* square root of rotational velocity for various rotated disk electrodes for oxidation of I^- to I_2 at 0.62 V. A_{geom}: 0.741 cm^2. Concentration of I^-: 1.0 mM. Electrodes: (a) Ru, (b) 0.5% Ru-Ti_4O_7, (c) 1% Ru-Ti_4O_7, (d) 5% Ru-Ti_4O_7.

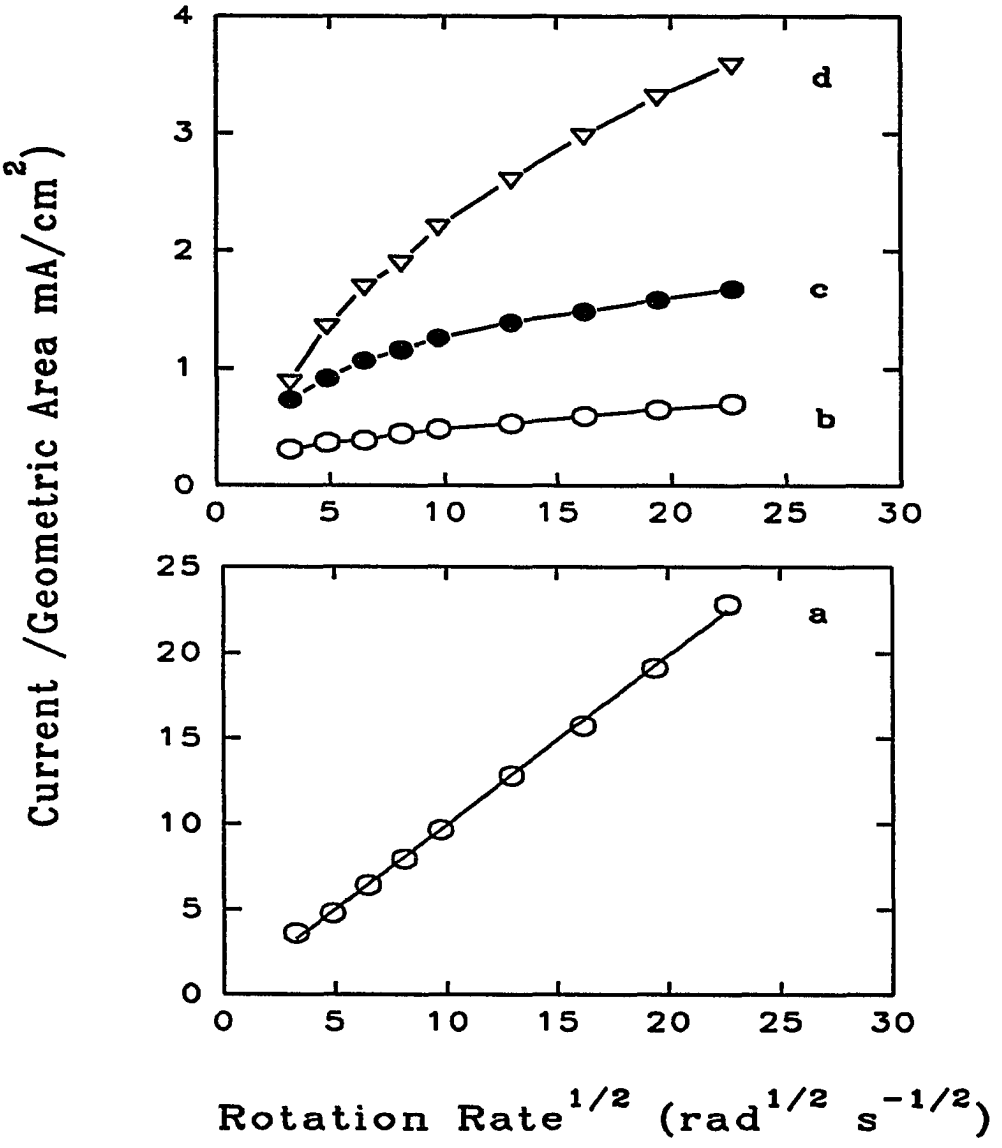

Figure 8. Plots of apparent current density *vs.* square root of rotational velocity for various rotated disk electrodes based on oxidation of I^- to IO_3^- at 1.18 V. A_{geom}: 0.741 cm^2. Concentration of I^-: 1.0 mM. Electrodes: (a) Ru, (b) 0.5% Ru-Ti_4O_7, (c) 1% Ru-Ti_4O_7 (d) 5% Ru-Ti_4O_7.

plot for the solid Ru RDE (Curve a) is linear with a near-zero intercept. Unlike Curve b in Figure 7 for the 0.5% Ru-Ti_4O_7 RDE, Curve b in Figure 8 exhibits significant dependence on $\omega^{1/2}$ for oxidation of I^- to IO_3^-. Undoubtedly, this is a reflection of both the complexity of this anodic O-transfer mechanismom as well as deviation of response for these electrodes from the ideal for microelectrode arrays.

Values of the relative current density (J, see Eqn. 1) are plotted *vs.* $\log(A_{act}/A_{geom})$ in Figures 9 and 10 for oxidations of I^- to I_2 (0.62 V) and to IO_3^- (1.18 V), respectively, at various Ru-Ti_4O_7 RDEs for three values of ω (Curves a - c). The theoretical value $J = 1$ (point d) for $A_{act}/A_{geom} = 1$, corresponding to a transport-limited reaction at the solid Ru RDE, is included as a reference point. As expected, J values are largest for the smallest ω value, *i.e.*, Curves c corresponding to $\omega = 10.5$ rad s^{-1}. The largest enhancement factors for oxidations of I^- to I_2 ($J = 23$) and to IO_3^- ($J = 20$) are apparent for the 1% Ru-Ti_4O_7 RDE. This electrode composition corresponds closely to the optimal fractional active area predicted by Weber for microelectrode arrays.[9] Even though it is expected that J will decrease with increased ω, the 1% Ru-Ti_4O_7 RDE still exhibits significantly larger J values than the Ru RDE at the highest velocity tested (512.9 rad s^{-1}, Curves a), *i.e.*, $J = 8$ and 6 for the production of I_2 and IO_3^-, respectively. With an increase in ω from 10.5 rad s^{-1} (Curves c) to 512.9 rad s^{-1} (Curves a), the composition producing the maximum J value shifts from 1% Ru-Ti_4O_7 to 2% Ru-Ti_4O_7 for the oxidation of I^- to IO_3^-. We do not have an explanation for this shift. Furthermore, we do have an explanation for the dramatic falloff of J values for 0.1% Ru-Ti_4O_7. However, we note the

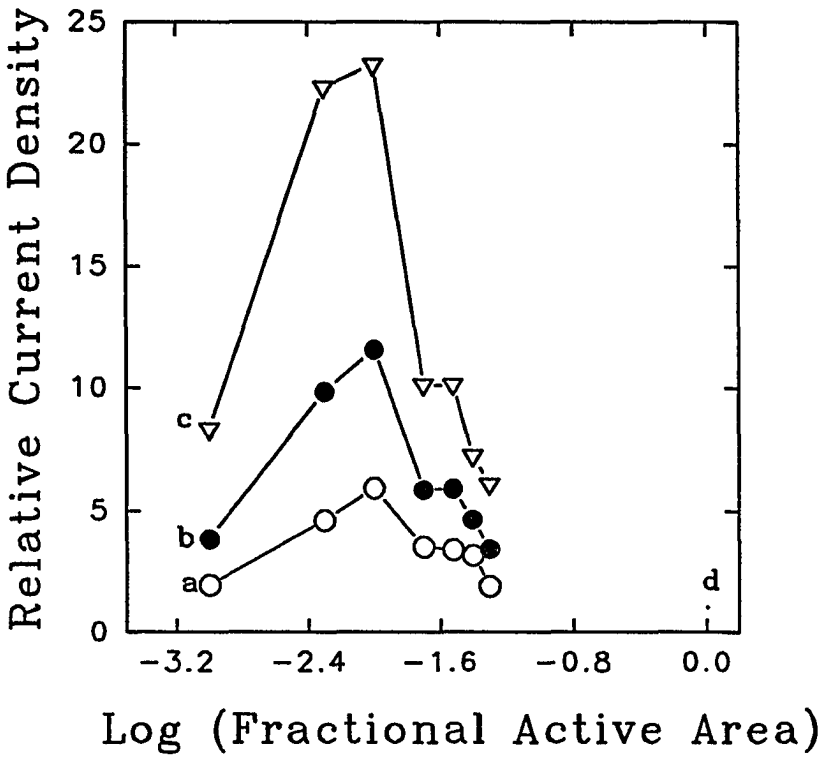

Figure 9. Relative current density (J) as a function of fractional active area ($A_{act}/A_{geom} = 1 - \theta$) at Ru-$Ti_4O_7$ rotated disk electrodes for oxidation of I^- to I_2 at 0.62 V. Concentration of I^-: 1.0 mM. Rotational velocity (rad s^{-1}): (a) 512.9, (b) 94.2, (c) 10.5, (d) value for solid Ru (by definition).

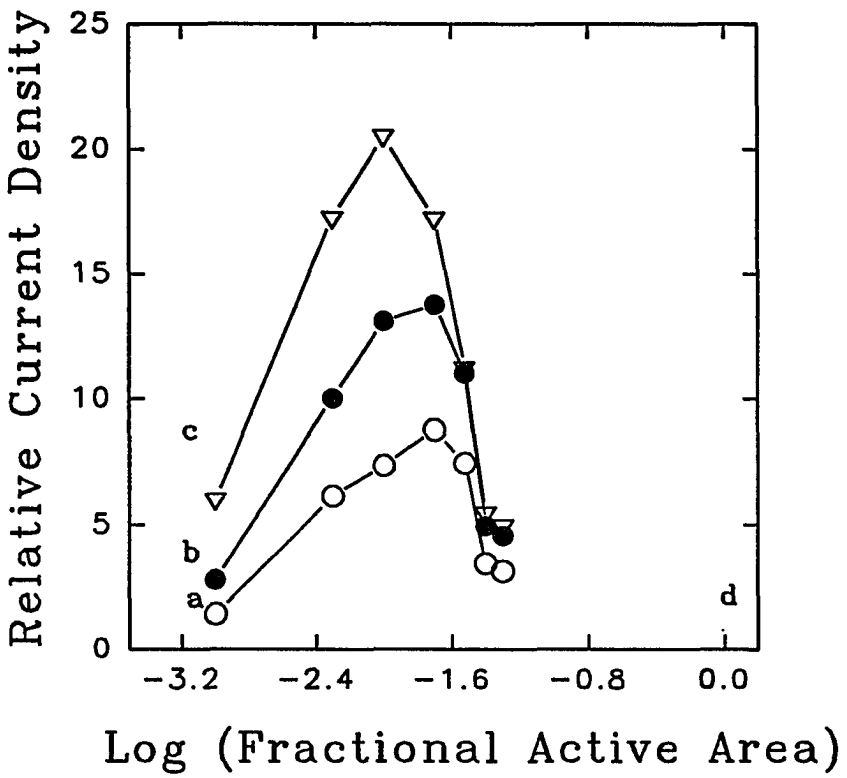

Figure 10. Relative current density (J) as a function of fractional active area (A_{act}/A_{geom} = 1 - θ) at Ru-Ti_4O_7 rotated disk electrodes for oxidation of I^- to IO_3^- at 1.18 V. Concentration of I^-: 1.0 mM. Rotational velocity (rad s^{-1}): (a) 512.9, (b) 94.2, (c) 10.5, (d) value for solid Ru (by definition).

high sensitivity of these values to even very small systematic errors in the measurement of the small electrode currents for this electrode.

Conclusions

Curvature observed in plots of i *vs.* $\omega^{1/2}$ and i^{-1} *vs.* $\omega^{-1/2}$ for transport-limited faradaic reactions at partially blocked rotated disk electrodes has been rationalized previously on the basis of significant overlap of adjacent diffusion zones when the distance between adjacent active regions is comparable to the diffusion-layer thickness at the electrode surface. [5,6,8,19-22] Hence, we rely on similar arguments to explain curvature in our plots, especially for oxidation of I^- to I_2 (Figs. 7 & 9) where kinetics complications are least expected.

The apparent current density (i/A_{geom}) for oxidation of I^- to I_2 (0.62 V) at the 0.5% Ru-Ti_4O_7 RDE is virtually independent of ω (Fig. 7, Curve **b**). Hence, we conclude this electrode virtually as an ideal microelectrode array without significant overlap of diffusion zones at adjacent Ru sites. The percentage composition of Ru in this electrode (0.5%) is well below the value *ca.* 1.7% predicted by Weber [9] for the optimal fractional area of microelectrode arrays. However, in apparent contradiction to Weber's prediction, i/A_{geom} for oxidation of I^- to IO_3^- at the 1% Ru-Ti_4O_7 RDE is sensitive to change in ω (Fig. 7, Curve **c**) and it is apparent that significant overlap exists between adjacent diffusion zones at this electrode surface. It is important to note, however, that Weber's prediction corresponds to a uniform distribution of active sites within the microelectrode array whereas we cannot adequately test the uniformity of our Ru-Ti_4O_7 surfaces.

Curvature in the plot of i/A_{geom} *vs.* $\omega^{1/2}$ for oxidation of I^- to IO_3^- (1.18 V) at 0.5% Ru-Ti_4O_7 (Fig. 8, Curve b) is concluded to be a consequence of the mechanistic complexity of this O-transfer reaction and does not negate the above conclusion regarding the absence of overlap of adjacent diffusion zones at this electrode surface. Anodic discharge of H_2O to produce adsorbed hydroxyl radicals ($\cdot OH_{ads}$) is required to occur concurrently with oxidation of I^- to O_3^-. [17] Hence, the anodic signal for IO_3^- production can exhibit characteristics of convective-diffusional transport limitation at small ω, when the flux (mol cm^{-2} s^{-1}) of I^- is smaller than that of $\cdot OH_{ads}$, or mixed transport-kinetic control at large ω, when the flux of I^- is comparable to or exceeds that of $\cdot OH_{ads}$.

The observation that $\leq$ 0.5% Ru-Ti_4O_7 respond in a manner expected for nearly ideal microelectrode arrays is consistent with results of a simple comparison of estimated values for the diffusion-layer thickness at the Ru sites and the distance between adjacent Ru sites. The steady-state diffusion layer thickness (δ) at an ideal microdisk electrode is $\pi r/4$, where r is the radius of the microdisk. [23,24] Based on the average diameter of 0.4 μm for Ru sites in Ru-Ti_4O_7 estimated on the basis of the Fresnel Construction in the XRD data, we calculate δ = 0.2 μm as a conservative estimate. This value of δ is significantly smaller than the value of 10 μm estimated for the minimum inter-site distance in 1% Ru-Ti_4O_7 surfaces using SEM. Hence, from this comparison, it is logical to expect that adjacent diffusion zones have virtually no overlap for this electrode material.

Whereas none of the Ru-Ti_4O_7 electrodes tested exhibited the transport-limited response obtained for pure Ru electrodes, the current densities at the Ru microelectrodes

were elevated significantly above that for pure Ru electrodes. Thus, we suggest that these Ru-Ti_4O_7 electrodes might have utility for large-scale applications wherein cost of precious metal electrode materials must be minimized.

Acknowledgment

Ames Laboratory is operated for the U.S. Department of Energy by Iowa State University under Contract No. W-7405-ENG-82. This research was supported by the Director for Energy Research, Office of Basic Energy Sciences.

References

1. O. Contamin and E. J. Levart, *J. Electroanal. Chem.*, **136**, 259 (1982).
2. S. L. Peterson and D. E. Tallman, *Anal. Chem.*, **60**, 82 (1988).
3. D. J. Chesney, J. L. Anderson, D. E. Weissaar and D. E. Tallman, *Anal. Chim. Acta*, **124**, 321 (1981).
4. J. E. Vitt, D. C. Johnson and D. E. Tallman, *Anal. Chem.*, **65**, 231 (1993).
5. F. Schelle, R. Landsberg and H. Wolf, *Electrochim. Acta*, **15**, 525 (1970).
6. E. Levart, *J. Electroanal. Chem.*, **187**, 247 (1985).
7. V. G. Levich, *Physicochemical Hydrodynamics*, Prentice Hall: Englewood Cliffs, NJ, p. 75 (1962).
8. V. Yu. Filinovsky, *Electrochim. Acta*, **25**, 309 (1980).
9. S. G. Weber, *Anal. Chem.*, **61**, 295 (1989).

10. R. L. Clarke, in *Proceedings of the Second International Forum on Electrolysis in the Chemical Industry*, Deerfield Beach, FL (1988).

11. P. C. S. Hayfield and R. L. Clarke, in *Proceedings of the Electrochemical Society Meeting*, Los Angeles, CA (1989).

12. P. C. S. Hayfield, *U.S. Patent* 4,422,917 (1983).

13. N. L. Weinberg, J. D. Genders and R. L. Clarke, *U.S Patent* 4,936,970 (1990).

14. P. Villars and L. D. Calvert, *Pearson's Handbook of Crystallographic Data for Intermetallic Phases*, 2nd ed., ASM International: Materials Park, OH, pp. 4776 & 5097 (1991).

15. Y. Le Page and M. Marezie, *J. Solid State Chem.*, **53**, 13 (1984).

16. A. Guinier, *X-Ray Diffraction*, W.H. Freeman and Co., San Francisco, CA, and London, U.K., p. 121 (1963).

17. J. E. Vitt and D. C. Johnson, *J. Electrochem. Soc.*, **138**, 774 (1992).

18. D.C. Johnson, *J. Electrochem. Soc.*, **119**, 331 (1972).

19. R. Landsberg and R. Thiele, *Electrochim. Acta*, **11**, 1243 (1966).

20. F. Schelle, S. Muller, R. Landsberg and H.-J. Spitzer, *J. Electroanal. Chem.*, **19**, 187 (1968).

21. A. M. Trukhan, Yu. M. Povarov and P. D. Lukovtsev, *Elektrokhim.*, **6**, 425 (1970).

22. Yu. M. Povarov, A. M. Trukhan and P. D. Lukovtsev, *Elektrokhim.*, **6**, 602 (1970).

23. K. B. Oldham, *J. Electroanal. Chem.*, **122**, 1 (1981).

24. K. Aoki and J. G. Osteryoung, *J. Electroanal. Chem.*, **122**, 19 (1981).

ELECTROCATALYSIS OF ANODIC OXYGEN-TRANSFER REACTIONS: $Bi_2Ru_2O_{7.3}$ ELECTRODES IN ACIDIC MEDIA

A paper submitted to *J. Appl. Electrochem.*

Lin He, Hugo F. Franzen and Dennis C. Johnson

Abstract

Details are reported for the synthesis and characterization of composite electrodes prepared from powdered $Bi_2Ru_2O_{7.3}$ and fashioned into the form of disk electrodes. Voltammetric data obtained for various anodic reactions at these electrodes are examined for evidence that oxidations can occur with transfer of oxygen to the oxidation products in the potential region corresponding to anodic discharge of H_2O with simultaneous evolution of O_2. Model reactants include: iodide, dimethyl sulfoxide, tetramethylene sulfoxide, and manganese(II). The structure of the synthesized material is concluded to correspond to that of pyrochlore oxides on the basis of X-ray diffractometry (XRD). Surface morphology of a composite electrodes is examined using scanning electron microscopy (SEM).

Introduction

This research is part of a larger effort directed to the discovery of new mixed-metal oxide electrodes that exhibit electrocatalytic activity for anodic reactions involving the

transfer of oxygen from H_2O in the solvent phase to the oxidation product(s). Goals of this research include the identification of important composition-structure-reactivity relationships as well as the discovery of new electrode materials that might have applicability in various electrochemical industries, including use as amperometric sensors. Here, we describe results for a pyrochlore ruthenate ($Bi_2Ru_2O_{7.3}$) synthesized by a thermal procedure commonly used in solid-state chemistry and fabricated into composite electrodes.

Pyrochlore ruthenates have received some attention from electrochemists because of their electrical properties.[1,2] Specifically, $Bi_2Ru_2O_{7.3}$ is characterized by high electrical conductivity and has been demonstrated to be an effective electrocatalyst for both anodic discharge of H_2O, with evolution of O_2, and cathodic reduction of dissolved O_2.[3,4] Recently, Marković and Ross presented results for O_2 reduction and evolution in 0.1 M KOH at $Bi_2Ru_2O_7$ having the pyrochlore structure.[5] Although less active than Ru and Bi_{ads}/Ru for O_2 evolution, the $Bi_2Ru_2O_7$ electrode was more stable during O_2 evolution. No reports were found for application of pyrochlore ruthenate electrodes to anodic O-transfer reactions.

This investigation is based on the premise that anodic discharge of H_2O to form adsorbed hydroxyl radicals (OH) is a prerequisite to anodic O-transfer reactions. Furthermore, it is assumed that benefit can come from reactant adsorption in the vicinity of adsorbed OH species, where the adsorption sites for OH and reactant species may or may not be identical. Based on these premises, our efforts to discover new catalytic materials to support anodic O-transfer reactions has emphasized the fabrication of mixed

metal oxides in which at least one of the metallic species is expected to present unfilled atomic *p*- and/or *d*-orbitals at the electrode surface that might function for adsorption of the OH species and/or the various reactants in O-transfer reactions.

A negative consequence of an increased density of adsorbed OH species at an inert anode surface is the decrease in the apparent O_2-evolution overpotential and the OH species also are an intermidiate product in the anodic evolution of O_2. Hence, the desired O-transfer reactions always are expected to occur with some concurrent evolution of O_2. Thus, the maximization of current efficiency for the desired O-transfer reactions is a major challenge in this work. We expect that current efficiencies will be maximized for relatively low densities of adsorption sites and at potentials corresponding to relatively low rates of O_2 evolution.

Iodide can be considered as an ideal model reactant in the characterization of new electrode materials because two anodic reactions have been observed for this ion at noble metal electrodes in acidic media:[6] (i) the oxidation of I^- to I_2 (1 eq mol^{-1}) by a quasi-reversible process with $E_{1/2}$ = ca. 0.5 V vs. SCE, and (ii) the oxidation of I^- to IO_3^- (6 eq mol^{-1}) by an irreversible process with a variable $E_{1/2}$ that is correlated with the overpotential for anodic discharge of H_2O.[6] Dimethyl sulfoxide (DMSO) and tetramethylene sulfoxide (TMSO) also are good model reactants because the expected oxidations to the corresponding sulfones ($DMSO_2$ and $TMSO_2$) have relatively simple stoichiometries that involve the transfer of single oxygen atoms. Furthermore, $E°$ values for the $DMSO_2$-DMSO and $TMSO_2$-TMSO half reactions are ca. 0.0 V vs. SCE.[7] Therefore, oxidations of DMSO and

TMSO are thermodynamically allowed at potentials accessible at the common anode materials (Pt, Au, PbO_2, C); however, these reactions are not observed to occur persistently at these anodes.[8] The anodic oxidation of Mn(II) is examined because multiple O-transfer steps are likely to be associated with production of MnO_2(s) and MnO_4^-.

Experimental

Reagents.—Standard solutions were prepared from reagent grade chemicals: KI (Fisher Scientific), $Mn(NO_3)_2$ (Sigma), DMSO (Fisher), and TMSO (Aldrich). The supporting electrolyte was 0.10 M H_2SO_4 (Mallinckrodt). Water was purified by distillation with passage through D-45 deionizing columns (Culligan) and a Milli-Q system (Millipore).

Electrodes.—A mixture of the appropriate amounts of Bi_2O_3 and RuO_2 (Alfa, Johnson Matthey) was ground in an agate mortar and then pressed into the form of a pellet using a laboratory press (Carve) at 5 tons cm^{-2} pressure. Pelletization improved contact between particles and, thereby, increased the diffusion rate during thermal treatment. The pellet was placed in a small Pt crucible located in the quartz tube of a resistance furnace. The pellet was annealed in air at 600 °C for 18 hr, 700 °C for 24 hr, and 800 °C for 72 hr under the control of an 818 Controller/Programmer (Eurotherm).

After thermal processing, the pellet was ground to a fine powder and blended with a polymeric cement (Duco) to produce a conductive paste. The paste was spread over one end of a stainless steel rod to be used as a rotated disk electrode (RDE, 0.264 cm^2). The outer surface of the rod then was covered with pure cement (Duco) and, after curing, was

wrapped with Teflon tape to eliminate contact between the cylindrical surface of the stainless steel and test solutions. Two disk electrodes were prepared using different ratios of powder to polymeric cement. RDE-I was made from a 1:1 (vol:vol) mixture of cement and powder and RDE-II was made from a ca. 2:1 (vol:vol) mixture. Finally, the end (disk) surfaces were polished lightly with 1-μm alumina (Buehler Ltd.). Only the end surfaces covered with the composite films were allowed to contact test solutions.

Instrumentation.—X-ray diffractometry (XRD) was performed using a XDS-2000 diffractometer (Scintag) with Cu-Kα_1 radiation. Scanning electron microscopy (SEM) was performed using a S-200 (Cambridge) equipped with a thin-window energy dispersive detector (Tracor Northern). X-ray photoelectron spectroscopy (XPS) was performed using a Perkin-Elmer 5500 multitechnique surface analysis system (Physical Electronics) with monochromatic Al-Kα radiation (1,486.6 eV, 300 W) for excitation. Binding energies were referenced to the O(1s) emission band at 531 eV,[9] and the difference in binding energy between O(1s) and Ru($3d_{5/2}$) was 247 eV. The base pressure of the ion-pumped ultrahigh vacuum (UHV) chamber was less than $1x10^{-9}$ Torr during analysis.

Voltammetry was performed using a RDE4 potentiostat and AFMSRX rotator (Pine Instrument Co.) interfaced with a 486 personal computer (Apex) by a DT2800-A data acquisition board (Data Translation) under the control of ASYST-3.1 software (Keithley/ASYST). The electrochemical cell had porous glass discs separating the working, reference, and counter electrode compartments. All potentials are reported in volts vs. a saturated calomel electrode (SCE, Fisher Scientific). The counter electrode was a Pt wire.

Voltammetric procedures.—Some data correspond to so-called difference voltammograms (Δi-E) generated by subtraction of the i-E responses obtained in the presence and absence of the reactant. Difference voltammetry is anticipated to discriminate against residual currents resulting from double-layer charging, formation and dissolution of surface oxides, and anodic and cathodic evolution of O_2 and H_2, respectively.[10]

Values for the effective number of electrons (n_{eff}, eq mol^{-1}) transferred in electrode processes were estimated from slopes of plots of Δi (mA) vs. the square root of the angular velocity of electrode rotation ($\omega^{1/2}$, $s^{-1/2}$) according to the Levich equation.[11]

Results and discussion

XRD and SEM data.—Figure 1 contains the XRD data obtained for the mixed metal-oxide powder prepared in this study (B) in comparison with the calculated pattern for $Bi_2Ru_2O_{7.3}$ (A).[12] These XRD data are in good agreement and it is concluded that the synthesized material is the pyrochlore ruthenate designated $Bi_2Ru_2O_{7.3}$. The average grain size for the material represented by Figure 1B is estimated to be 0.7 μm on the basis of the Fresnel Construction.[13]

The planar surface of RDE-I prepared from the material represented in Figure 1B was examined using SEM and typical micrographs are shown in Figures 2A to 2C. The appearance is that of a nearly homogeneous 1:1 mixture of conductive $Bi_2Ru_2O_{7.3}$ particles (black, 0.1 to 10 μm diameter) within a nonconductive (white) matrix of the polymeric adhesive. The existence of porosity is very evident in Figure 2C.

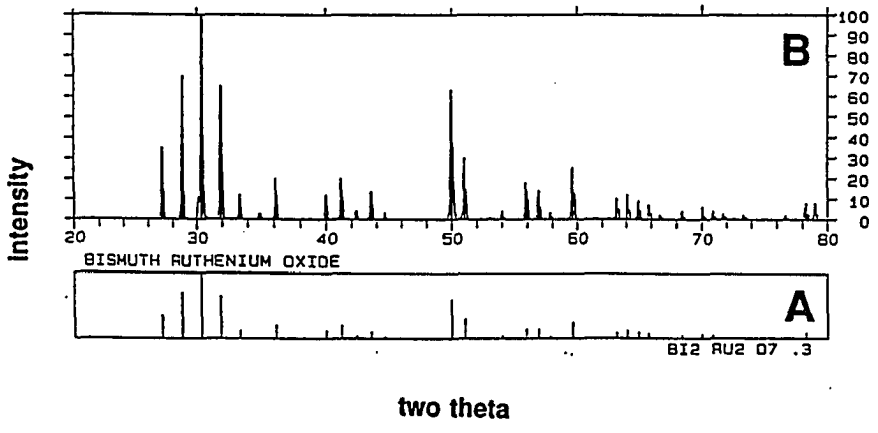

Figure 1. X-ray powder diffraction patterns: (A) theoretical for $Bi_2Ru_2O_{7.3}$, (B) prepared powdered sample.

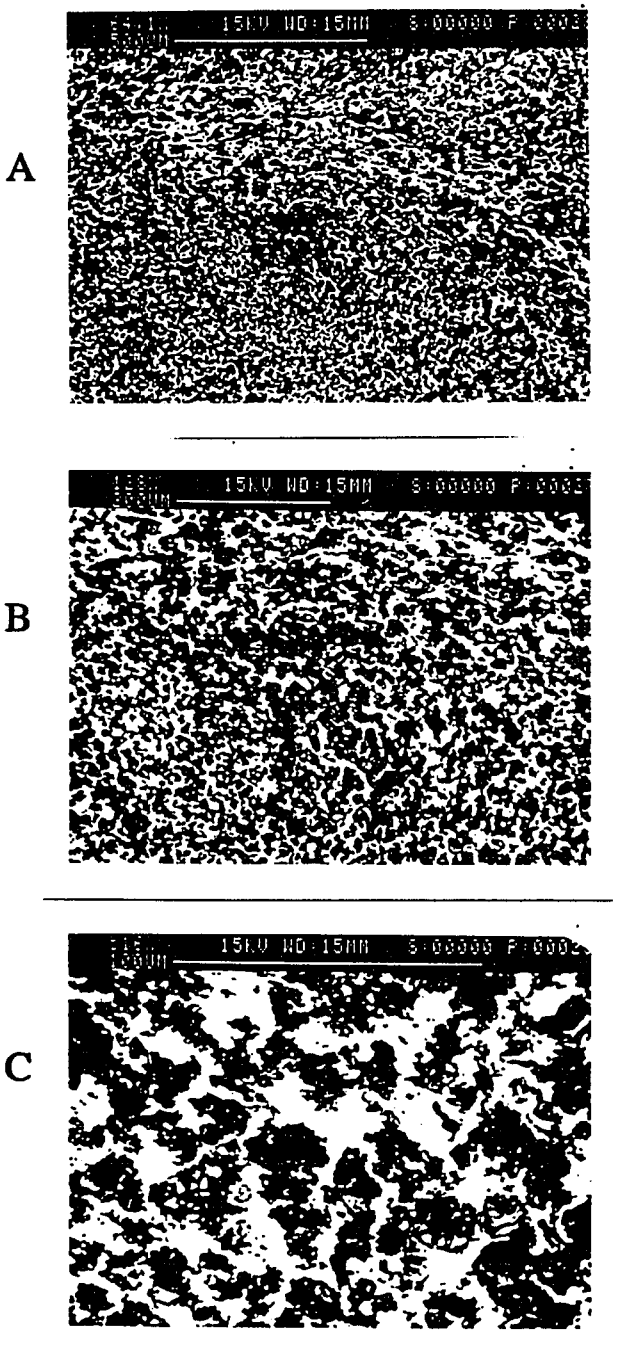

Figure 2. Scanning electron micrographs of the composite surface of RDE-I.

Anodic response for iodide.— Figure 3A contains the *i-E* curves obtained with RDE-II in 0.10 M H_2SO_4 containing 2.5 mM I^- (——) in comparison with the residual response (- - - -). Anodic discharge of H_2O with evolution of O_2 is readily observed to occur in the residual curve for $E > 1.6$ V in this acidic medium (Figure 3A). The anodic wave in Figure 3A with $E_{1/2}$ = ca. 1.10 V is concluded to correspond to oxidation of I^- to I_2. Whereas this $E_{1/2}$ value is substantially more positive than that observed for the same reaction at noble metal electrodes (i.e., $E_{1/2}$ = ca. 0.5 V at Pt, Ir and Au),[6] this $E_{1/2}$ is close to the value 1.0 V observed at glassy carbon electrodes.[6] The large anodic wave in Figure 3A with $E_{1/2}$ = ca. 1.5 V occurs coincidently with onset of H_2O discharge and is, therefore, concluded tentatively to correspond to the anodic O-transfer reaction in which I^- is converted to IO_3^-. Figure 3B contains the Δi-E response for 2.50 mM I^- obtained by difference voltammetry, i.e., corresponding to the difference between the two curves shown in Figure 3A. A peak in the value for Δi is observed at ca. 1.6 V with a substantial decrease for $E > 1.6$ V corresponding to the region of increasing contribution to total current observed in the residual curve for O_2 evolution. A peaked response in the Δi-E curves would occur if the presence of I^- results in a decrease in the rate of O_2 evolution. Hence, values of Δi for $E >$ ca. 1.6 V are underestimates of the anodic current from oxidation of I^- to IO_3^-. Figure 3C shows *i-E* curves (positive scan) obtained as function of increasing I^- concentration. The plot of Δi (E = 1.20 V) vs. C^b was determined to be linear (r = 0.999, N = 5) for C^b in the range 0.5 to 2.5 mM. As is apparent from Figure 3C, evidence for a transport-limited current for oxidation of I^- to IO_3^- in the region $E >$

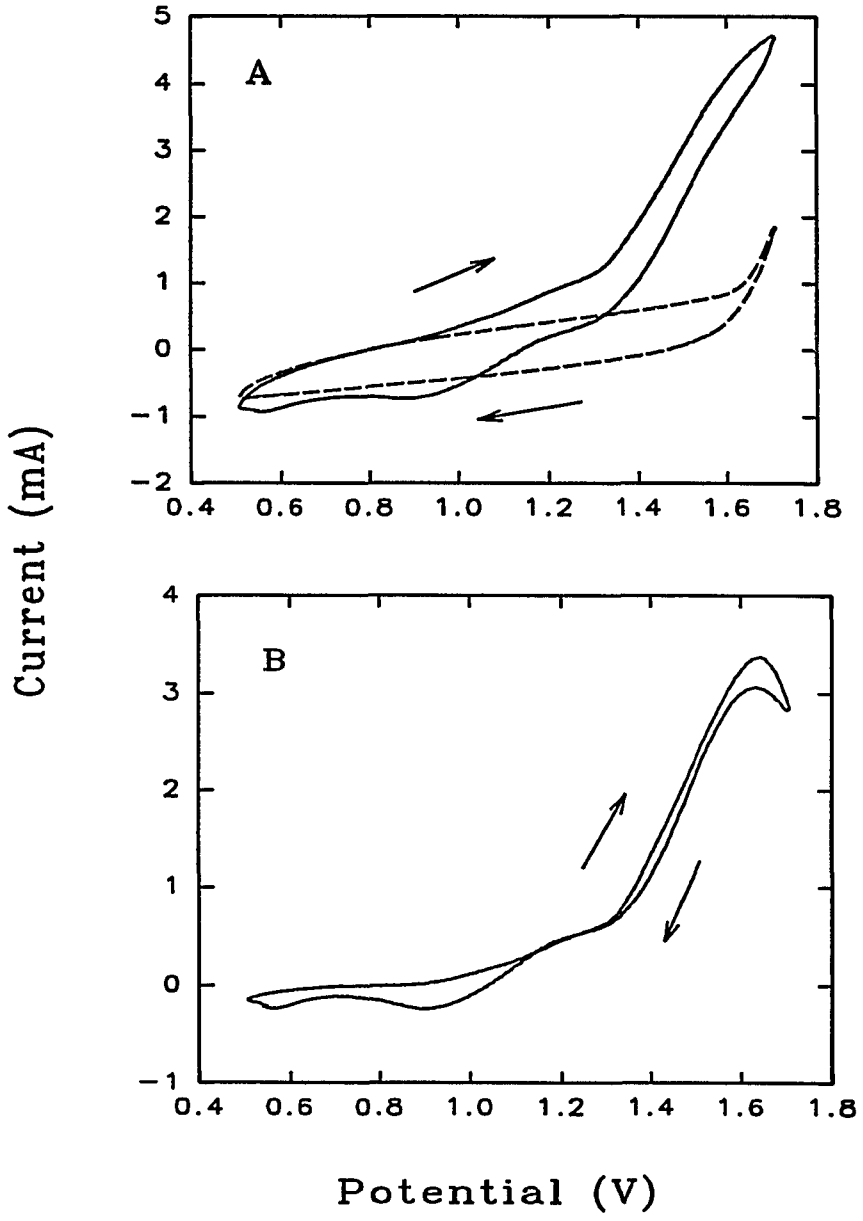

Figure 3A&B Cyclic voltammetric (A) and difference voltammetric (B) response at RDE-II (A_{geom} =0.264cm^2) for 2.50 mM I^-. Electrolyte: 0.10 M H_2SO_4. Rotation rate: 168 rad s^{-1}. Scan rate: 30 mV s^{-1}.

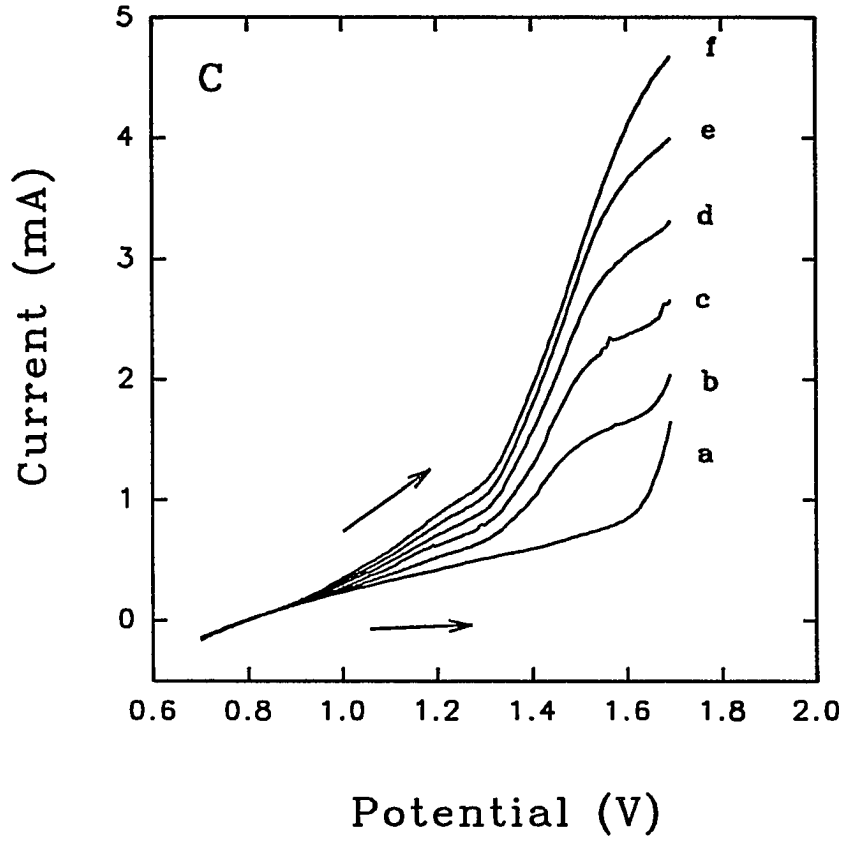

Figure 3C Voltammetric response (pos. scan) at RDE-II (A_{geom} =0.264cm^2) as a function of I^- concentration (mM): (a) 0, (b) 0.5, (c) 1.0, (d) 1.5, (e) 2.0, (f) 2.5 . Electrolyte: 0.10 M H_2SO_4. Rotation rate: 168 rad s^{-1}. Scan rate: 30 mV s^{-1}.

1.4 V becomes increasingly obscure as C^b is increased. This is evidence that increasing values of I^- concentrations require increasingly larger rates of H_2O discharge to produce a sufficient flux of OH species to support transport-limited rate of oxidation of I^- to IO_3^-.

Figure 4 contains Levich plots corrected for the residual current (Δi vs.$\omega^{1/2}$) corresponding to oxidation of I^- at E = 1.2 V (Curve A) and at 1.59 V (Curve B) at the RDE-II. These potential values are chosen to correspond approximately to the regions of maximum Δi for the two anodic processes. The plots are linear with regression statistics given by: $\Delta i = a + b\omega^{1/2}$, where a = 0.025 mA and b = 0.0070 mA $s^{-1/2}$ (r = 0.996) (Curve A); and $\Delta i = a + b\omega^{1/2}$, where a = 0.091 mA and b = 0.043 mA $s^{-1/2}$ (r = 0.999) (Curve B). The linearity of these Δi-$\omega^{1/2}$ plots is an indication that the corresponding anodic processes occur at virtually transport-limited rates at the potentials designated. Furthermore, we note that the ratio of slopes for the two plots, i.e., 0.043/0.0070 = 6.1, is in very good agreement with the expected value of $n_{eff,1.59V}/n_{eff,1.20V}$ = 6 corresponding to transport-limited oxidations of I^- to IO_3^- (1.59 V) and to I_2 (1.20 V).

The value of $E_{1/2}$ for oxidation of I^- to IO_3^- in 0.10 M H_2SO_4 at RDE-I (data not shown) was ca. 1.1 V. Differences between $E_{1/2}$ values observed for the two electrodes are discussed in a later section.

Anodic response for DMSO and TMSO.-Oxidations of DMSO and TMSO are thermodynamically allowed at potentials accessible at the common anode materials (Pt, Au, PbO_2, C); however, these reactions are not observed to occur persistently at these anodes.[8] Figure 5A contains the i-E curve obtained at RDE-II in 0.10 M H_2SO_4 containing 5.0 mM

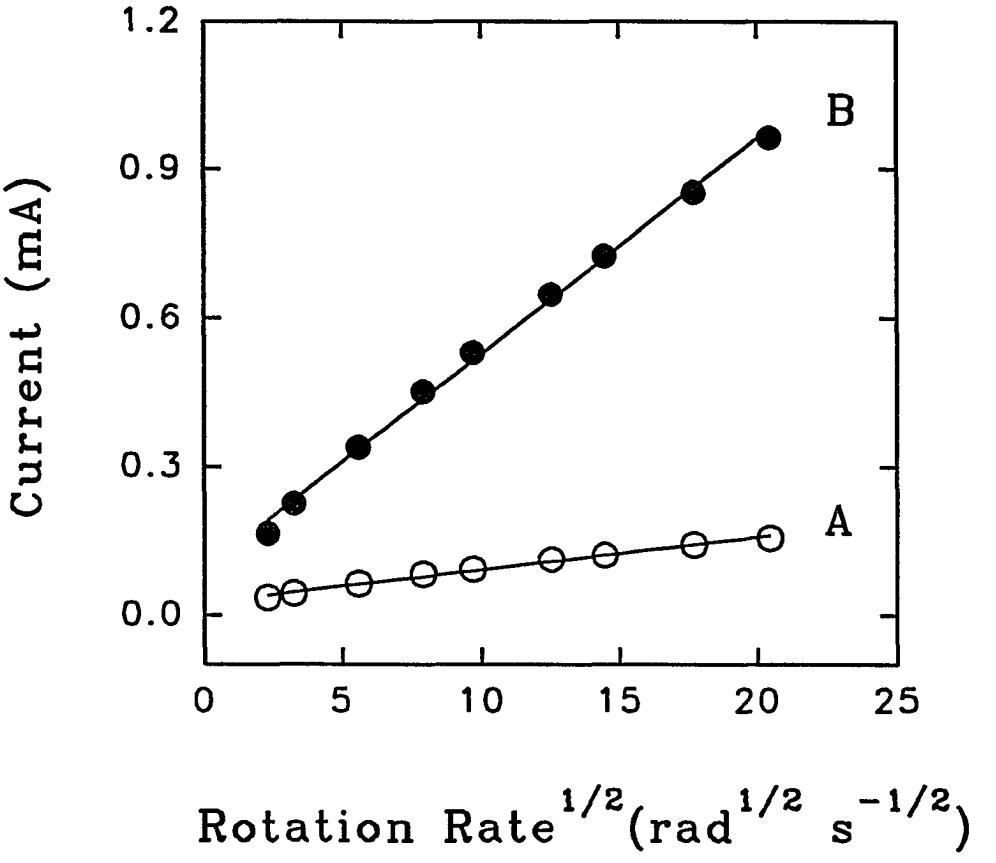

Figure 4. Levich plots of residual-corrected current at electrode RDE-II (A_{geom} =0.264cm^2) for oxidation of 0.5 mM I^- in 0.1 M H_2SO_4 as a function of potentials (V vs. SCE): (A) 1.20, (B) 1.59.

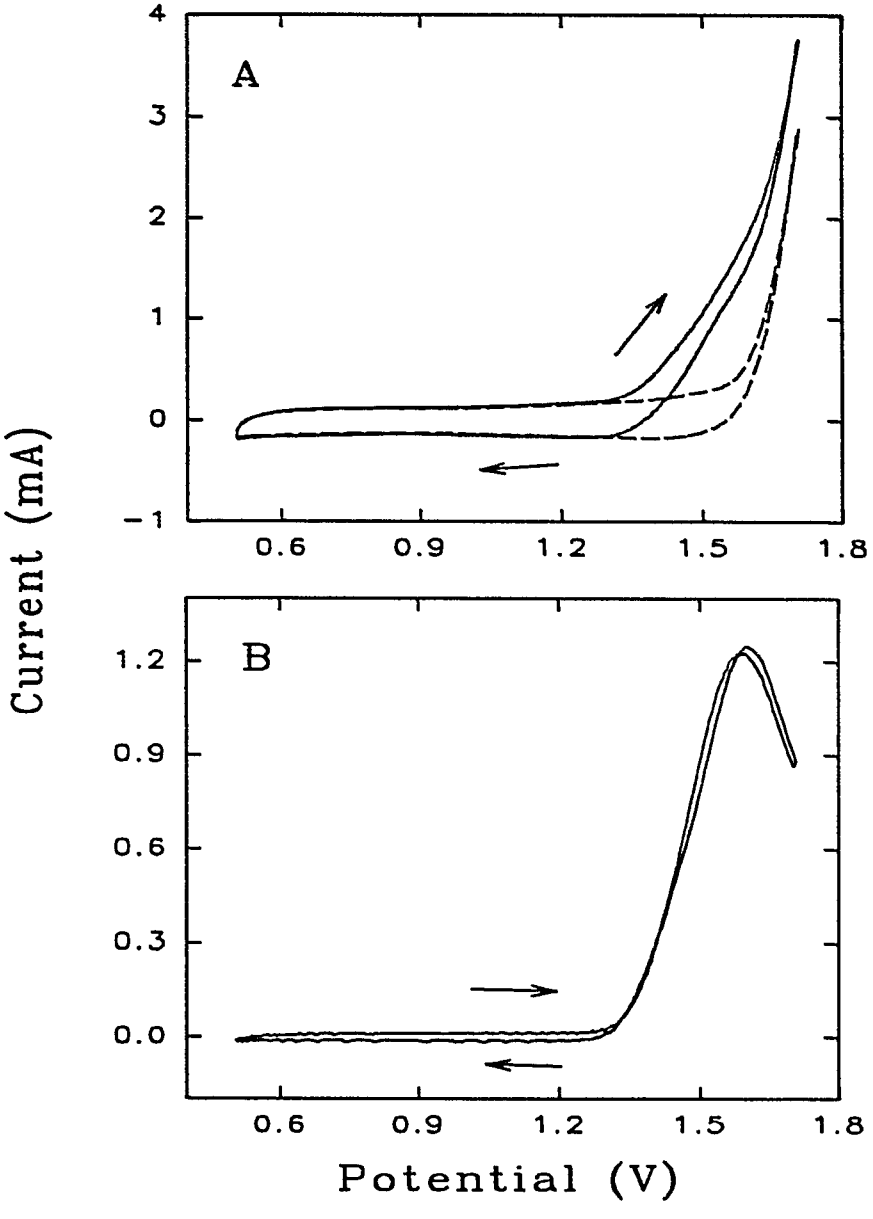

Figure 5A&B Cyclic voltammetric (A) and difference voltammetric (B) response at RDE-II (A_{geom} =0.264cm^2) for 5 mM DMSO. Electrolyte: 0.1 M H_2SO_4. Rotation velocity: 168 rad s^{-1}. Scan rate: 30 mV s^{-1}.

DMSO (——) in comparison to the residual response (- - - -), and Figure 5B contains the corresponding Δi-E curve computed from the data in Figure 5A. The large anodic wave in Figure 5B with $E_{1/2}$ = ca. 1.45 V, occurring concurrently with anodic discharge of H_2O, is concluded to correspond to oxidation of DMSO to $DMSO_2$. Again, the peaked of the Δi-E curve (E_{peak} = ca. 1.6 V) is interpreted as an indication of the failure of difference voltammetry to discriminate accurately against the large residual current for $E > 1.6$ V. Figure 5C contains i-E curves (pos. scan) as a function of DMSO concentration which demonstrate that $E_{1/2}$ for DMSO oxidation shifts to more positive values as concentration is increased. This behavior is to be expected for a quasi-irreversible anodic reaction that requires simultaneous discharge of H_2O.

Figure 6 contains the Levich plot of the anodic currents obtained by difference voltammetry (Δi-$\omega^{1/2}$) at RDE-II for oxidation of 1.0 mM DMSO at 1.60 V. The non-linearity of this plot is interpreted to be evidence that the reaction occurs under mixed kinetic-transport control. Regression statistics of the linear segment constructed with a zero intercept in Figure 6 are indicated by: $\Delta i = b\omega^{1/2}$, where $b = 0.037$ mA $s^{1/2}$ ($r = 0.992$). The value n_{eff} = 2.3 eq mol^{-1} was calculated from the slope using A_{geom} = 0.264 cm^2, ν = 0.010 cm^2 s^{-1}, and assuming $D = 1.0 \times 10^{-5}$ cm^2 s^{-1}. Considering the assumption for D, this calculated value for n_{eff} is in good agreement with the conclusion that DMSO is oxidized to $DMSO_2$ at 1.60 V.

Figures 7A and 7B contain i-E and Δi-E data, respectively, obtained with RDE-II for 5 mM TMSO in 0.10 M H_2SO_4. It is concluded tentatively that the anodic wave

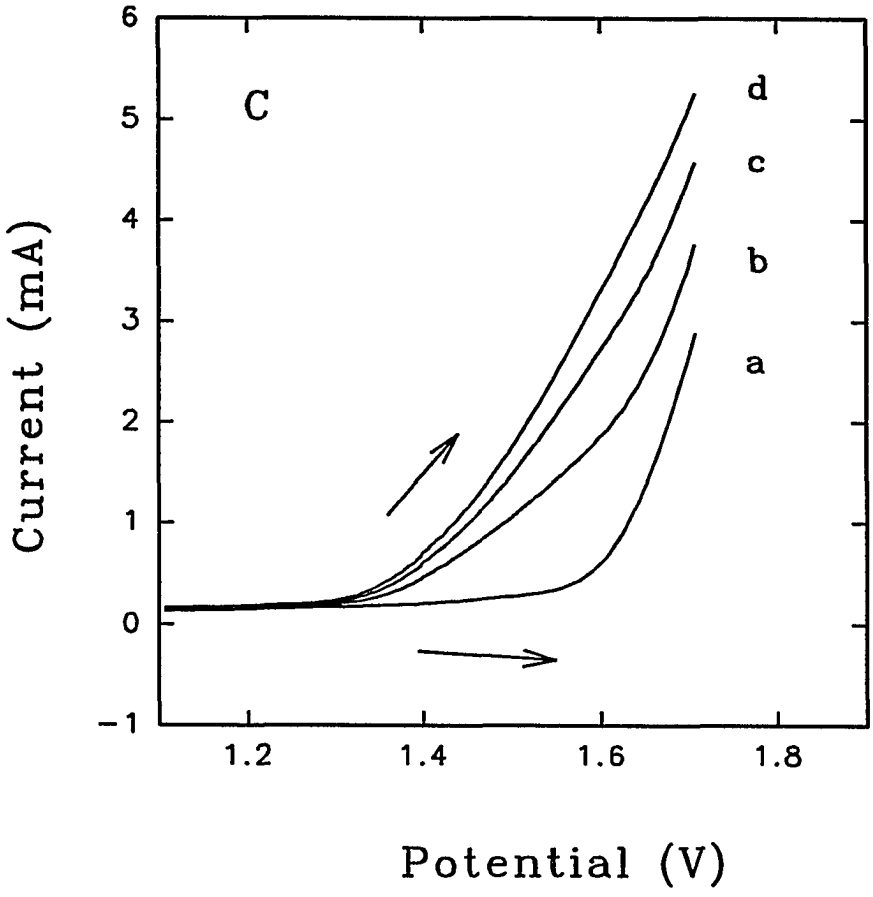

Figure 5C. Voltammetric response (pos. scan) at RDE-II (A_{geom} =0.264cm^2) of DMSO as a function of concentration (mM): (a) 0, (b) 5, (c) 10, (d) 15. Electrolyte: 0.1 M H_2SO_4. Rotation velocity: 168 rad s^{-1}. Scan rate: 30 mV s^{-1}.

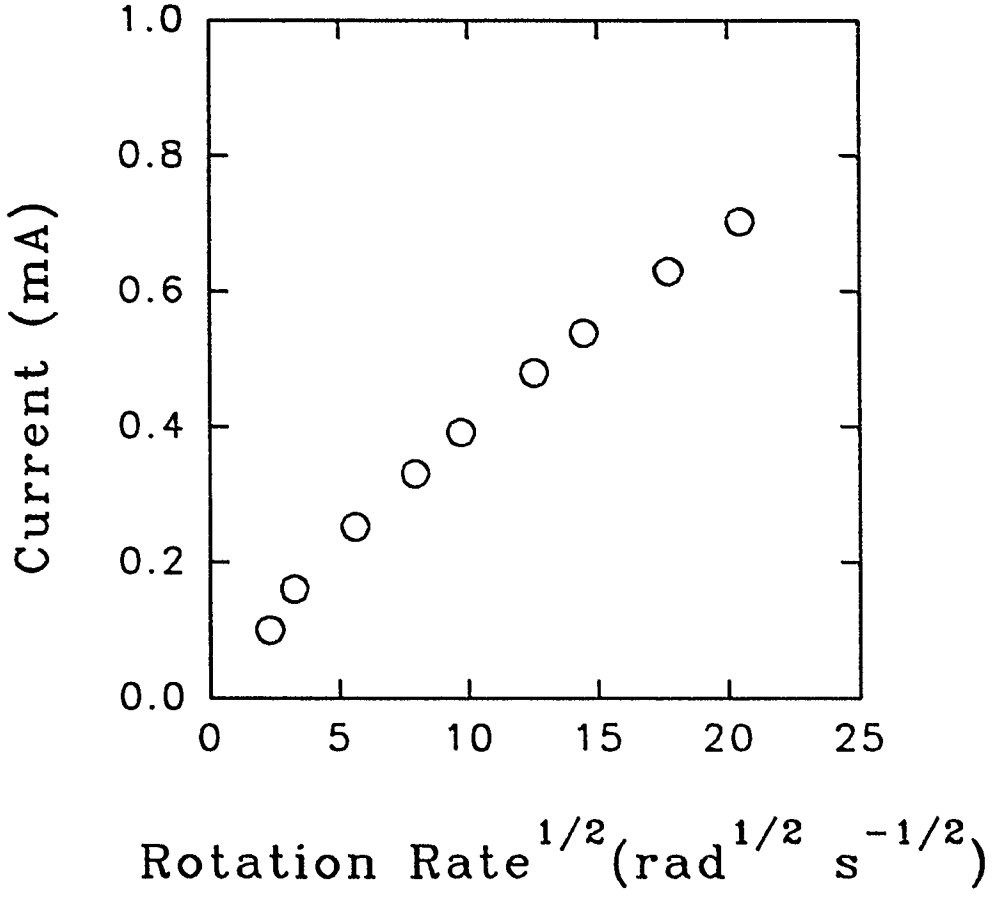

Figure 6. Levich plots of residual-corrected currents at electrode RDE-II (A_{geom} =0.264cm^2) at 1.60 V for oxidation of 1.0 mM DMSO in 0.1 M H_2SO_4.

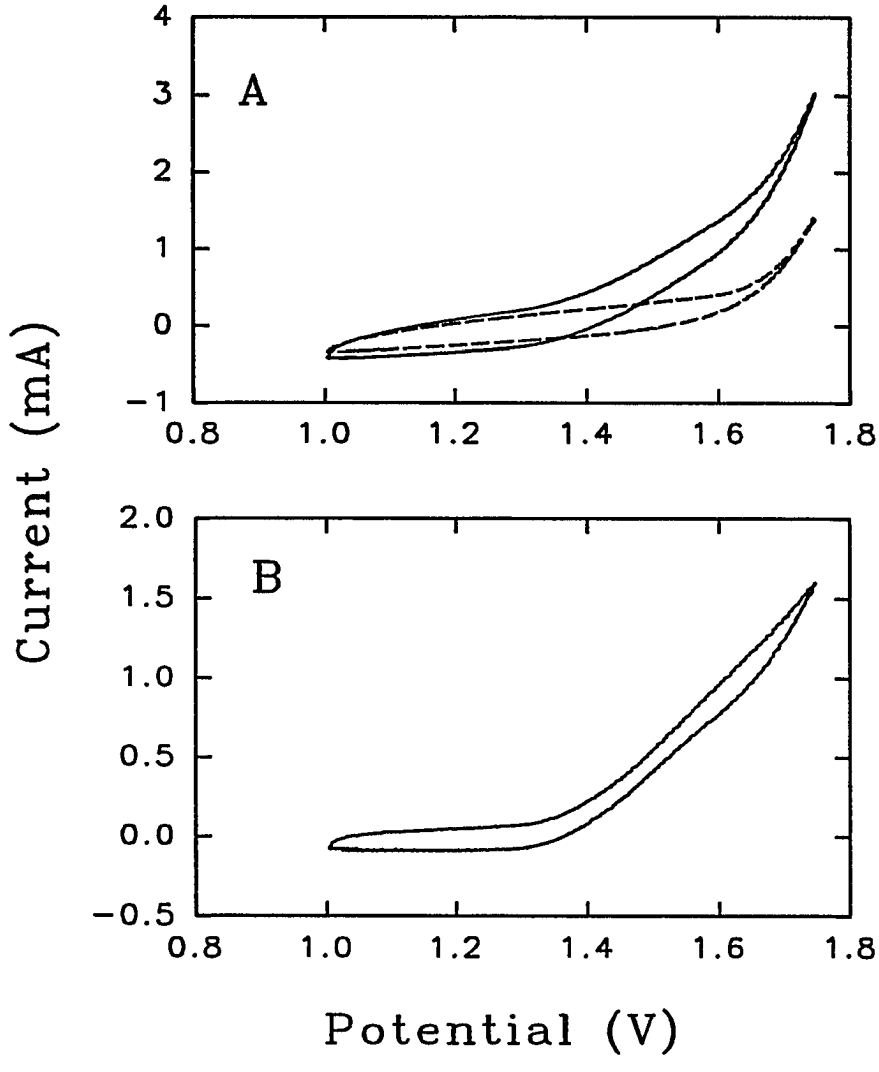

Figure 7A&B Cylcic voltammetric (A) and difference voltammetric (B) response at RDE-II (A_{geom} =0.264cm^2) for 5 mM TMSO, and linear-scan voltammetric responses (pos. scan) (C) for TMSO as a function of concentration (mM): (a) 0, (b) 5, (c) 10, (d) 15. Electrolyte: 0.1 M H_2SO_4. Rotation velocity: 168 rad s^{-1}. Scan rate: 30 mV s^{-1}.

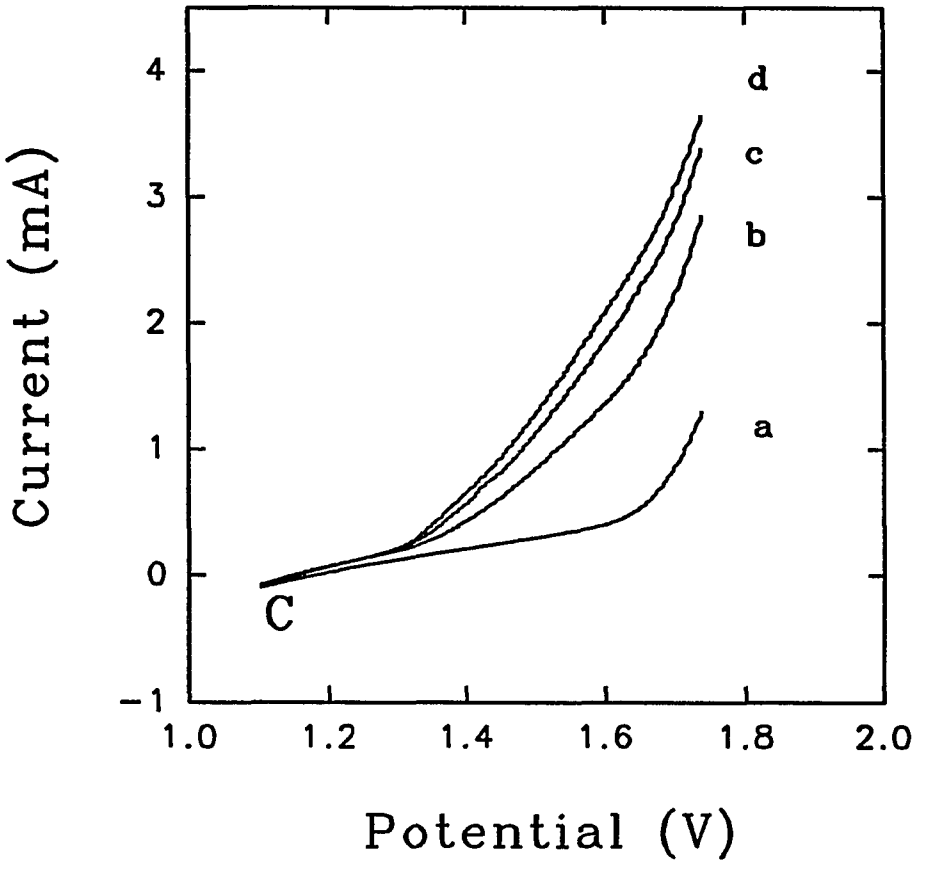

Figure 7C Voltammetric responses (pos. scan) at RDE-II (A_{geom} =0.264cm^2) for TMSO as a function of concentration (mM): (a) 0, (b) 5, (c) 10, (d) 15. Electrolyte: 0.1 M H_2SO_4. Rotation velocity: 168 rad s^{-1}. Scan rate: 30 mV s^{-1}.

corresponding to $E_{1/2}$ = ca. 1.56 V results from oxidation of TMSO to $TMSO_2$. The current response for TMSO is smaller than that for DMSO, measured at the same rotational velocity and potential, and the $E_{1/2}$ for TMSO (1.56 V) is slightly more positive than that for DMSO (1.45 V). Figure 7C contains *i-E* curves (pos. scan) as a function of TMSO concentration. Again, as in Figure 5C for DMSO, the $E_{1/2}$ shifts to more positive values with increasing concentration, as is expected for a quasi-irreversible anodic reaction.

Figures 8 contains the Levich plot of the corrected current obtained by difference voltammetry (Δi-$\omega^{1/2}$) for 2.0 mM TMSO at RDE-II using data obtained at 1.66 V. The non-linear plot is evidence that the reaction occurs under mixed kinetic-transport control. Regression statistics for the linear segment constructed having a zero intercept in this plot are indicated by: $i = b\omega^{1/2}$ where b = 0.070 mA $s^{-1/2}$. From this slope, the value n_{eff} = 2.2 eq mol^{-1} was calculated using A_{geom} = 0.264 cm^2, ν = 0.010 cm^2 s^{-1}, and assuming D = 1.0 x 10^{-5} cm^2 s^{-1}. This value in consistent with the conclusion that TMSO is oxidized to $TMSO_2$ at the designated potential.

Values of $E_{1/2}$ for oxidation of DMSO and TMSO in 0.10 M H_2SO_4 at RDE-I (data not shown) were determined to be 1.15 V and 1.05 V, respectively.

Anodic response for Mn(II).-Figures 9A and 9B contain *i-E* and Δi-*E* curves, respectively, obtained at RDE-I for 50 mM Mn^{2+} in 0.10 M H_2SO_4. Anodic discharge of H_2O with evolution of O_2 is readily observed to occur in the residual curve for $E > 1.3$ V in this acidic medium (Figure 9A). The anodic currents for O_2 in Figure 9A are larger than those in Figure 5 at all potentials because the smaller polymer content of the composite

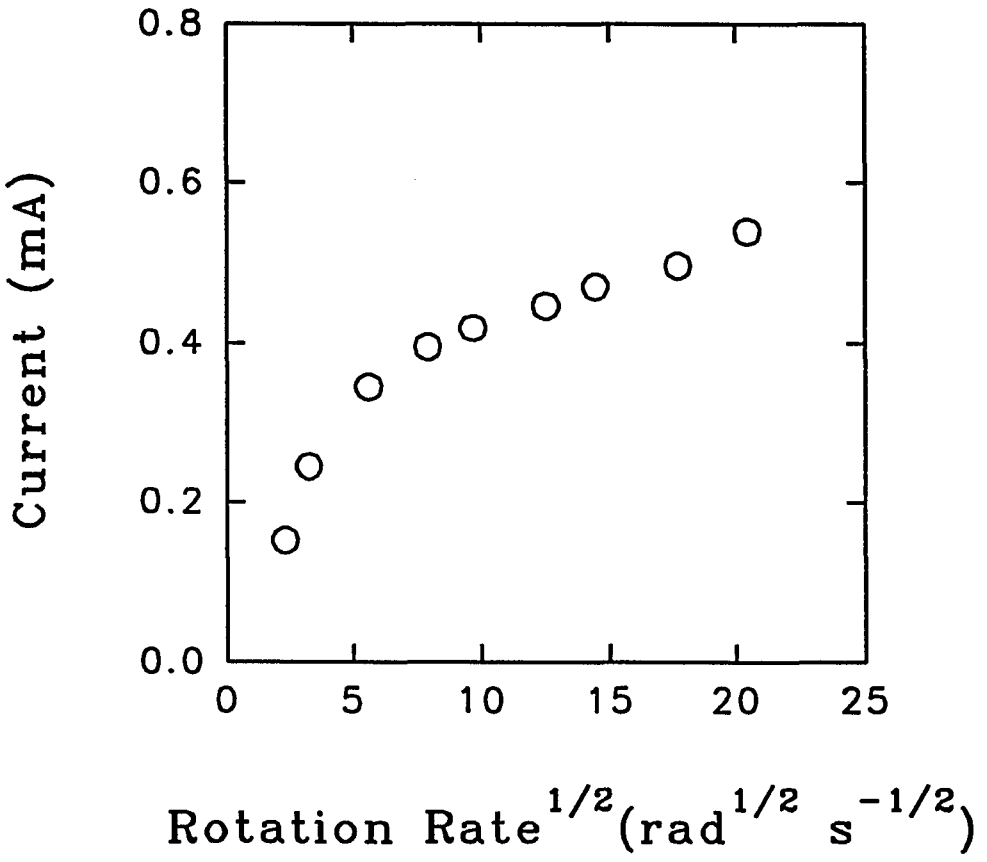

Figure 8. Levich plots of residual-corrected current at RDE-II (A_{geom} =0.264cm^2) at 1.66 V for oxidation of 2 mM TMSO in 0.1 M H_2SO_4.

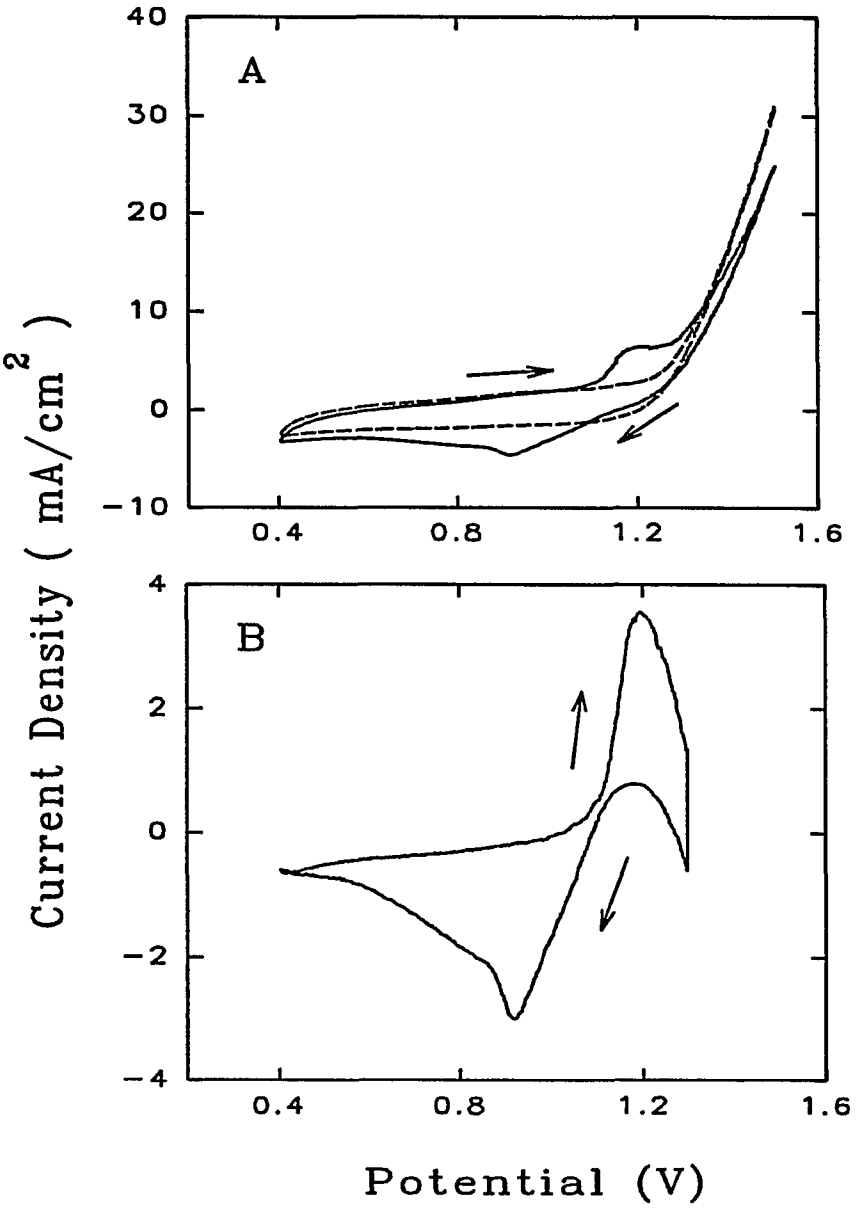

Figure 9A&B Cyclic voltammetric (A) and difference voltammetric (B) response at RDE-I for 50 mM Mn(II). Electrolyte: 0.1 M H_2SO_4. Rotation velocity: 168 rad s^{-1}. Scan rate: 30 mV s^{-1}.

larger value for the effective area of this composite electrode. The anodic wave obtained material for RDE-I results in greater porosity at the RDE-I surface with the result of a during the positive scan in Figure 9A ($E_{1/2}$ = ca. 1.13 V) is concluded to correspond to oxidation of Mn^{2+}. However, the appearance of a cathodic peak (E_{peak} = 0.93 V) during the negative scan is evidence that the product of Mn^{2+} oxidation is MnO_2(s) instead of MnO_4^-. Figures 9C and 9D contain *i-E* curves for the positive and negative scans, respectively, obtained as function of Mn^{2+} concentration. The conclusion that MnO_2(s) is the product of Mn^{2+} oxidation at $E > 1.1$ V is supported by the *i-E* curves (negative scan) in Figure 9D which shows that the area under the cathodic stripping peak increases approximately as a linear function of Mn^{2+} concentration.

A solution containing 50 mM Mn^{2+} was electrolyzed for a 2-hr period at RDE-I for a constant potential of 1.24 V and a rotational velocity of 168 s^{-1}. There was no evidence for the formation of purple MnO_4^-. Following this electrolysis, the electrode was removed from the test solution, rinsed with deionized water, and analyzed by XPS. Figure 10 contains XPS results obtained before (A) and after (B) the 2-hr electrolysis period. Peaks 1 and 2 (Figure 10B) correspond to binding energies of 642 eV and 654 eV, respectively, which match the reported values for MnO_2 ($2p_{3/2}$ and $2p_{1/2}$) at 642.2 eV and 653.9 eV[11] but not those values for MnO_4^- at 646.6 eV and 657 eV.[9]

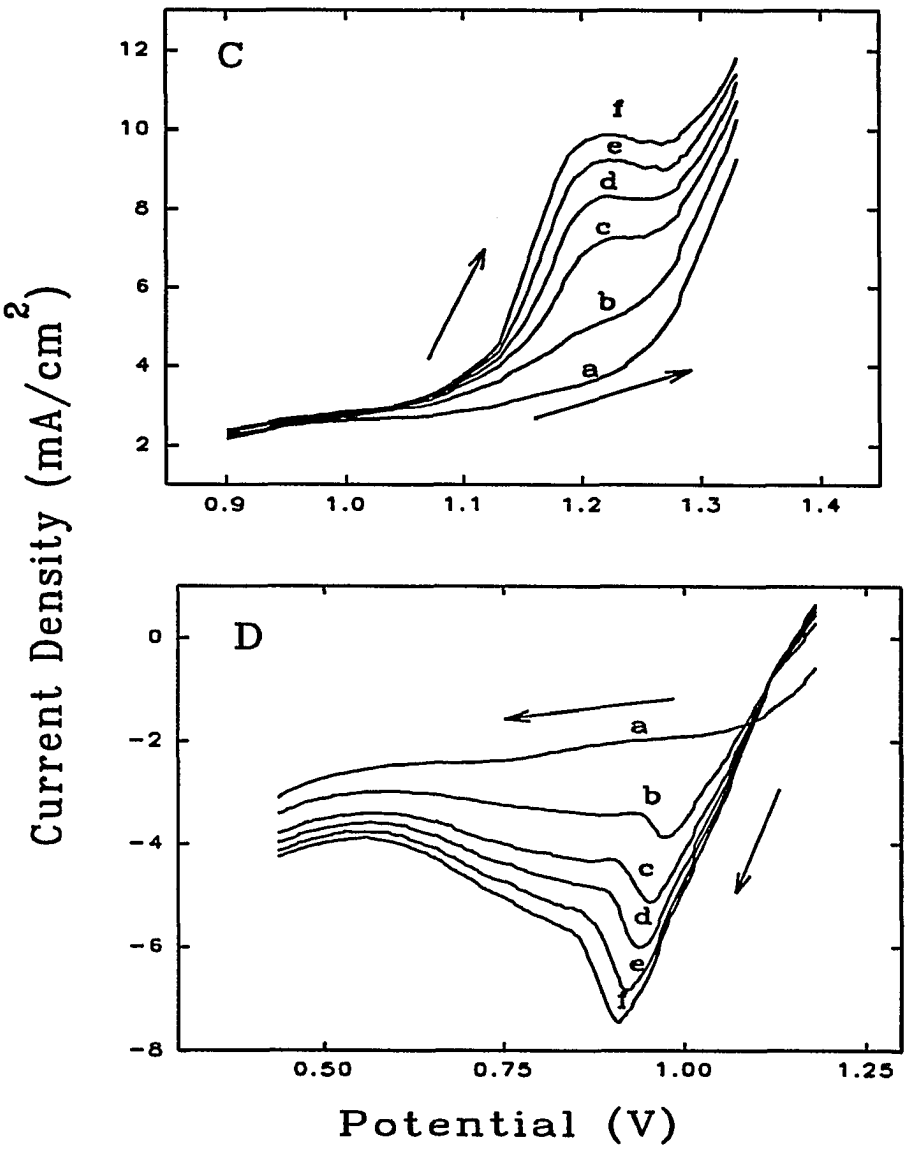

Figure 9C&D Voltammetric responses at RDE-I during positive scan (C) and negative scan (D) for Mn(II) as a function of concentration (mM): (a) 0, (b) 10, (c) 20, (d) 30, (e) 40, (f) 50. Electrolyte: 0.1 M H_2SO_4. Rotation velocity: 168 rad s^{-1}. Scan rate: 30 mV s^{-1}.

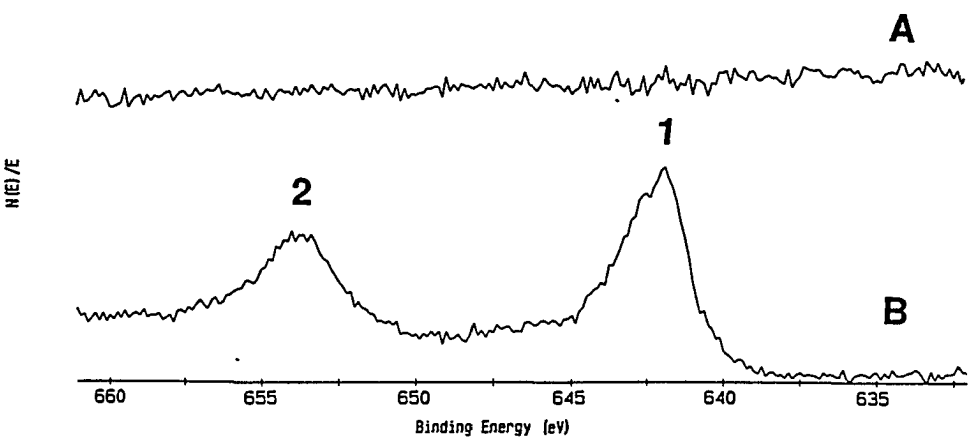

Figure 10 ESCA spectra before (A) and after (B) electrolysis at 1.24 V for 2 hr in 0.1 M H_2SO_4 containing 50 mM Mn(II) at RDE-I.

Conclusions

It is the foremost premise of this research that anodic discharge of H_2O to produce adsorbed hydroxyl radicals (OH) is a prerequisite of anodic O-transfer reactions. Hence, voltammetric waves for anodic O-transfer reactions are expected to have similar $E_{1/2}$ values which correlate with the onset of O_2 evolution. This premise is supported by data obtained in this study and summarized in Table 1. The $E_{1/2}$ values for the specified anodic reactions at the separate electrodes are similar in spite of large differences in the corresponding $E°$ values. However, the averages of these $E_{1/2}$ values for the individual electrodes are substantially different, i.e., ca. 1.1 V for RDE-I and ca. 1.5 V for RDE-II. Nevertheless, the difference of 0.4 V between these averages correlates with the difference in potential for onset of substantial O_2-evolution at the two electrodes, i.e., ca. 1.2 V for RDE-I (see Figure 9) and ca. 1.6 V at RDE-II (see Figure 3A). This difference in apparent O_2-evolution overpotential is concluded to be a consequence of the difference in true surface areas resulting from the differing amounts of polymer used in preparation of the two composite electrodes. The polymer-to-$Bi_2Ru_2O_{7.3}$ ratio was 1:1 for RDE-I and 2:1 for RDE-II. Hence, the active surface area (A_{active}) corresponding to exposed $Bi_2Ru_2O_{7.3}$ particles is larger in RDE-I than in RDE-II. This fact is substantiated by the observation that the charging currents, based on a comparison of the residual curves in the region 0.8 V to 1.2 V, are approximately 5X larger at RDE-I (Figure 9) than at RDE-II (Figure 3). The flux density for OH species generated by discharge of H_2O is proportional to A_{active}; however, the flux density of reactant species being transported to the rotated electrode is

Table 1: Comparison of $E_{1/2}$ and $E°_{ox,red}$ Values.

Reactions (0.10 M H_2SO_4)	$E°_{ox,red}$ (V vs. SCE)	$E_{1/2}$ (V vs. SCE)	
		RDE-I[c]	RDE-II[c]
$I^- \rightarrow IO_3^-$	0.79[a]	1.1	1.5
DMSO $\rightarrow$ $DMSO_2$	-0.07[a]	1.15	1.45
TMSO $\rightarrow$ $TMSO_2$	-0.1[b]	1.05	1.56
$Mn^{2+} \rightarrow MnO_2(s)$	0.86[a]	1.13	n.a.

[a] Data taken from Reference 14.

[b] Estimated from data in References 15 and 16.

[c] Rotational velocity: 168 s^{-1}.

proportional to the geometric area (A_{geom}). Hence, the smaller value of the A_{active}:A_{geom} ratio at RDE-II results in a positive shift in $E_{1/2}$ values for anodic O-transfer reactions in comparison to RDE-I. The variation of $E_{1/2}$ with changes in the A_{active}:A_{geom} ratio requires further study. However, the composite materials studies here do not provide sufficient control of A_{active} to support such a study.

It is disappointing that MnO_2(s) instead of MnO_4^- is observed to be the product of Mn^{2+} oxidation at $Bi_2Ru_2O_{7.3}$ composite electrodes. A similar observation was reported for the Bi(V)-Pb(IV) mixed-oxide electrodes. More specifically, virtually no Mn^{2+} oxidation occurs at pure PbO_2 electrodes, only MnO_4^- is generated at transport-limited rates at the mixed-oxide electrodes containing a Bi(V):Pb(IV) ratio of ca. 1, and some MnO_2(s) is generated simultaneously with MnO_4^- for mixed-oxide electrodes containing $0 <$ Bi(V):Pb(IV) $\ll 1$. In the later case, accumulation of MnO_2(s) resulted to fouling of the electrode with cessation of further oxidation of Mn^{2+}.[17] Hence, we conclude for the $Bi_2Ru_2O_{7.3}$ electrode, that the surface activity of adsorbed OH species is sufficient to support product of MnO_2(s) but not MnO_4^-, even at relatively large positive potentials for which the rate of H_2O discharge is large and, therefore, the flux of OH radicals would seem to be adequate to support the O-transfer reaction. Perhaps this is evidence that the OH species is not adsorbed with sufficient stability to ensure a lifetime adequate to support the mechanism for MnO_4^- production. Hence, the effective surface activity of adsorbed OH is small in spite of a substantial rate of OH generation.

Finally, the fact should not be minimized that $Bi_2Ru_2O_{7.3}$ composite electrode do

exhibit sufficient electrocatalytic activity to support the anodic O-transfer reactions for DMSO and TMSO, whereas these reactions are not observed at the common anode materials (Au, Pt, PbO_2, GC).

Acknowledgments

ESCA data were obtained by James W. Anderegg. Ames Laboratory is operated for the U.S. Department of Energy by Iowa State University under Contract No. W-7405-ENG-82. This research was supported by the Director for Energy Research, Office of Basic Energy Sciences.

References

[1] R. Kanno, Y. Takeda, T. Yamamoto, Y. Kawamoto, and O. Yamamoto, *J. Solid State Chem.* **102**, 106 (1993).

[2] P. A. Cox, J. B. Goodenough, P. J. Tavener, and D. Telles, *J. Solid State Chem.* **62**, 360 (1986).

[3] H. S. Horowitz, J. M. Longo, H. H. Horowitz, and J. T. Lewandowski, in "*Solid State Chemistry in Catalysis*", R. K. Grasselli and J. F. Brazdil (Eds.), ACS Symposium Series 279, p.143, Amer. Chem. Soc.: Washington, DC (1985).

[4] H. S. Horowitz, J. M. Longo, and H. H.Horowitz, *J. Electrochem. Soc.*, **130**, 1851 (1983).

[5] N. M. Marković and P. N. Ross, Jr., *J. Electrochem. Soc.*, **141**, 2590 (1994).

[6] J. E. Vitt and D. C.Johnson, *J. Electrochem.Soc.*, **139**, 774 (1992).

[7] "Standard Potentials in Aqueous Solution," A. J. Bard, R. Parsons, and J. Jordan, Editors, Marcel Dekker, New York (1985).

[8] H. Chang and D. C. Johnson, *J. Electrochem. Soc.*, **137**, 2452 (1990)

[9] "Handbook of X-ray Photoelectron Spectroscopy" Jill Chastain (Ed.), Perkin-Elmer Corporation (1992).

[10] M. Noel and K. I. Vasu, "Cyclic Voltammetry and the Frontiers of Electrochemistry," Aspect Publications Ltd. (1990) p.24.

[11] V. G. Levich, *Physicochemical Hydrodynamics*, Prentice-Hall, Inc.: Englewood Cliffs, N.J., pp. 62-70 (1962).

[12] JCPDS (file No. 26-222) International Center for Diffraction Data, 1601 Park Lane, Swarthmore, PA (1992).

[13] A. Guinier, X-Ray Diffraction, W. H. Freeman and Co., San Francisco, and London, p.121 (1963).

[14] B.Milazzo and S. Carol, "Tables of Standard Electrode Potentials," Wiley, New York (1978).

[15] A. J. Bard, R. Parson, and J. Jordan (Eds.), "Standard Potentials in Aqueous Solution," Marcel Dekker, New York (1985).

[16] W. M. Latimer, "Oxidation Potentials," 2nd ed., Prentice-Hall, Englewood Cliffs, NJ (1952).

[17] W. R. LaCourse, Y.-L. Hsiao, D. C. Johnson, *J. Electrochem.Soc.*, **136**, 3714 (1989).

ELECTROCATALYSIS AT PYROCHLORE OXIDE ELECTRODES: I^- OXIDATION AND IO_3^- REDUCTION AT $Bi_2Ir_2O_7$ IN ACIDIC MEDIA

A paper to be submitted to *J. Electrochem. Soc.*

Lin He, Hugo F. Franzen and Dennis C. Johnson

Abstract

A mixed metal oxide, having the formula $Bi_2Ir_2O_7$, was prepared using a standard thermal technique and shown by x-ray diffractometry (XRD) to have the Pyrochlore Oxide structure. Composite disk electrodes were constructed from the powdered $Bi_2Ir_2O_7$ and their voltammetric activity for I^- and IO_3^- in 0.10 M H_2SO_4 was determined to be very similar to the activity of a pure Ir electrode.

Introduction

Among the ternary metallic oxides, compounds of the general formula $A_2B_2O_7$ (A and B are metals) represent a family of phases isostructural to the mineral pyrochlore. $A_2B_2O_7$ compounds exhibit a wide variety of interesting physical properties. This is because the B element can be a transition metal with variable oxidation state or a post transition metal and the A element can be a rare earth or an element with an inert lone-pair of electrons.

Pyrochlore oxides, especially pyrochlore ruthenates, have received some attention

because of their electrical[1,2,3] and electrochemical properties[4,5]. However, the electrocatalytical properties of $Bi_2Ir_2O_7$ have not been investigated. As has been determined for other pyrochlore materials, $Bi_2Ir_2O_7$ is characterized by high electrical conductivity (10^3 ohm^{-1} cm^{-1}) and low paramagnetic susceptibility ($2.8x10^{-4}$ emu)[6]. The low resistivity and small paramagnetic susceptibility of $Bi_2Ir_2O_7$ are concluded to indicate the presence of a partially filled band and the absence of localized, unpaired electrons[6]. These characteristics are believed to be important in establishing interesting catalytic properties for the pyrochlore oxides.

One particularly troubling aspect of modern electrochemical technology is the scarcity of reversible bi-directional electrocatalysts.[7] We note that the lead-ruthenium and bismuth-ruthenium pyrochlore oxides have been reported to catalyze both the O_2-evolution and O_2-reduction reaction mechanisms.[7] Research described here is part of a larger effort motivated by the desire to determine whether pyrochlore oxides exhibit bi-directional catalytic properties for electrochemical processes involving the transfer of oxygen atoms to/from H_2O in the solvent phase from/to products of the electrode reactions. More specifically, we describe results for the anodic and cathodic reactions resulting in the interconversion of I^- and IO_3^- at $Bi_2Ir_2O_7$ composite electrodes in acidic media.

Two anodic waves have been routinely observed for I^- at a variety of electrode materials in acidic media.[8] The first wave corresponds to the reaction $2I^- \rightarrow I_2 + 2e^-$ (1 eq mol^{-1}) occurring by a quasi-reversible process with $E_{1/2}$ = ca. 0.5 V for noble metal electrodes. The second wave corresponds to the reaction $I^- + 3H_2O \rightarrow IO_3^- + 6H^+ + 6e^-$

(6 eq mol^{-1}) that occurs by an irreversible process requiring the concomitant anodic discharge of H_2O.[8] Hence, the $E_{1/2}$ for IO_3^- production is correlated with the overpotential for H_2O discharge at the electrode under consideration.[8] The irreversible electrocatalytic reduction of IO_3^- at Pt has been studied.[9,10] The mechanism requires adsorption of IO_3^- at oxide-free surface sites; however, I_2, the product of the reduction reaction, is strongly adsorbed at these same Pt sites and, thereby, blocks the mechanism for IO_3^- reduction. Reduction of IO_3^- occurs at more negative potentials by a coupled mechanism in which I_2 is reduced to I^- followed by a homogeneous reaction in the diffusion layer by which IO_3^- reacts with I^- to produce more I_2.

This investigation is based on the premise that the intermediate state of oxygen in these reaction mechanisms has the form of adsorbed hydroxyl radicals (OH_{ads}).[8] Hence, the anodic oxidation of I^- to IO_3^- must occur with concomitant discharge of H_2O to generate OH_{ads}. Furthermore, the direct reduction of IO_3^- to I_2 is presumed to occur by a mechanism in which oxygen atoms from IO_3^- are adsorbed at appropriate surface sites in the form of hydroxyl species (OH_{ads}) followed by their reduction to H_2O.

Experimental

Reagents.-Standard solutions were prepared from reagent grade chemicals: KI (Fisher Scientific Co.) and $NaIO_3^-$ (Fisher Scientific Co.). Electrolyte solution was 0.1 M H_2SO_4, prepared from reagent grade H_2SO_4 (Mallinckrodt), in deionized water. Distilled water was purified further by passage through two D-45 deionizing tanks (Culligan) and a Milli-Q

system (Millipore).

Electrodes.-A mixture of the appropriate amounts of Bi_2O_3 (Alfa, Johnson Matthey) and IrO_2 (Alfa, Johnson Matthey) was ground in an agate mortar until the color was uniform and then pressed into the form of a pellet using a laboratory press (Carve) at 5 tons cm^{-2} pressure. Pelletization improved contact between particles and, thereby, increased the diffusion rates during thermal treatment. The pellet was placed in a small Pt crucible which was located in a quartz tube in a resistance furnace. The pellet was annealed in air at temperatures programmed by an 818 Controller/Programmer (Eurotherm): 600°C for 24 hrs, 750°C for 48 hrs, and finally, 850°C for 72 hrs.

After the thermal treatment, the pellet was ground to a fine powder and blended with a polymeric cement (Duco) to produce a conductive paste. The paste was spread over one end of a stainless steel rod which was used as a rotating disk electrode (RDE, 0.264 cm^2). The outer surface of the rod was covered with pure cement (Duco) and, after curing, was wrapped with Teflon tape to eliminate contact between the cylindrical surface of the stainless steel and test solutions. Two disk electrodes were prepared using different cement-to-powder ratios. RDE-I was made from a 1:1 (vol:vol) mixture of cement and powder, and RDE-II was made from a 2:1 (vol:vol) mixture. Finally, the end surface of the rod was polished with 1-μm alumina (Buehler Ltd.). Only the end surface covered with the composite electrode material was allowed to contact test solutions during voltammetric experiments.

Instrumentation.- X-ray diffractometry (XRD) was performed using an XDS-2000 (Scintag) diffractometer using Cu-$K\alpha_1$ radiation. Scanning electron microscopy (SEM) was

performed using a S-200 (Cambridge) microscope equipped with a thin-window energy dispersive detector (Tracor Northern).

Voltammetry was performed using an RDE4 potentiostat and AFMSRX rotator (Pine Instrument) interfaced with a personal computer (Apex) by a DT2820-A data acquisition board (Data Translation) using ASYST-3.1 software (Keithley/ASYST). The electrochemical cell was made of Pyrex with porous glass discs separating the working, reference and counter electrode compartments. All potentials are reported in volts *vs.* a saturated calomel electrode (SCE; Fisher Scientific). The counter electrode was a coiled Pt wire (7.6 cm^2).

Voltammetric procedures.-Some current-potential data correspond to difference data obtained by subtracting the response obtained in the pure supporting electrolyte from that obtained following addition of an electroactive species. Hence, this procedure tends to minimize contributions to the net voltammetric response from background processes, *e.g.*, double-layer charging, formation and dissolution of surface oxide(s), and evolution of O_2 and H_2.

The mass transport-limited response at uniformly accessible rotated disk electrodes is a linear function of the square root of angular velocity of rotation ($\omega^{1/2}$, s^{-1}) as indicated by:[11]

$$i = 0.62 n_{eff} F A_{geom} D^{2/3} \nu^{-1/6} C^b \omega^{1/2} \qquad [1]$$

where i is the electrode current (mA) corrected for the background response, n_{eff} is the effective number of electrons in the reaction (eq mol^{-1}), A_{geom} is the geometric electrode area (cm^2), ν is the kinematic viscosity of the solution (cm^2 s^{-1}), C^b is the bulk concentration of

the reactant (mol L^{-1}), and F and D have their usual electrochemical significance.

Results and discussion

XRD and SEM data.-Figure 1 contains the XRD pattern obtained for the mixed oxide prepared in this study (B) in comparison with the calculated pattern for $Bi_2Ir_2O_7$ (A)[13]. These XRD data are in good agreement and, therefore, it is concluded that the material prepared for this study is principally the pyrochlore oxide designated as $Bi_2Ir_2O_7$. Bismuth may be required for metallic conductivity.[6] The formation of strong Bi-O sp bonds leads to filled bonding sp bands and empty, strongly destabilized, antibonding sp bands. The $6s^2$ electron pair would then have to be promoted into the next available Bi orbitals which are 6p. These orbitals can form π-bonds with O and since they are degenerate by symmetry, the two Bi electrons will be in a half-filled π^* band. This band with Bi electrons may be the conduction band. The average grain size for the material represented by Figure 1B was estimated to be on the order of 0.072 μm on the basis of the Fresnel Construction.[14]

The planar surface of the composite disk electrode prepared from the material represented in Figure 1B was examined using SEM and typical micrographs are shown in Figures 2A to 2D under different magnitude. The appearance is that of a nearly homogeneous 50:50 mixture of conductive $Bi_2Ir_2O_7$ particles (white, 0.01 - 1 μm dia.) within a nonconductive (black) matrix of the adhesive. The existence of porosity is evident (see Fig.2C & 2D). The particle size of $Bi_2Ir_2O_7$ is in good agreement with that estimated by Fresnel Construction. It is known[15] for powder that the lower the crystallite size, the higher

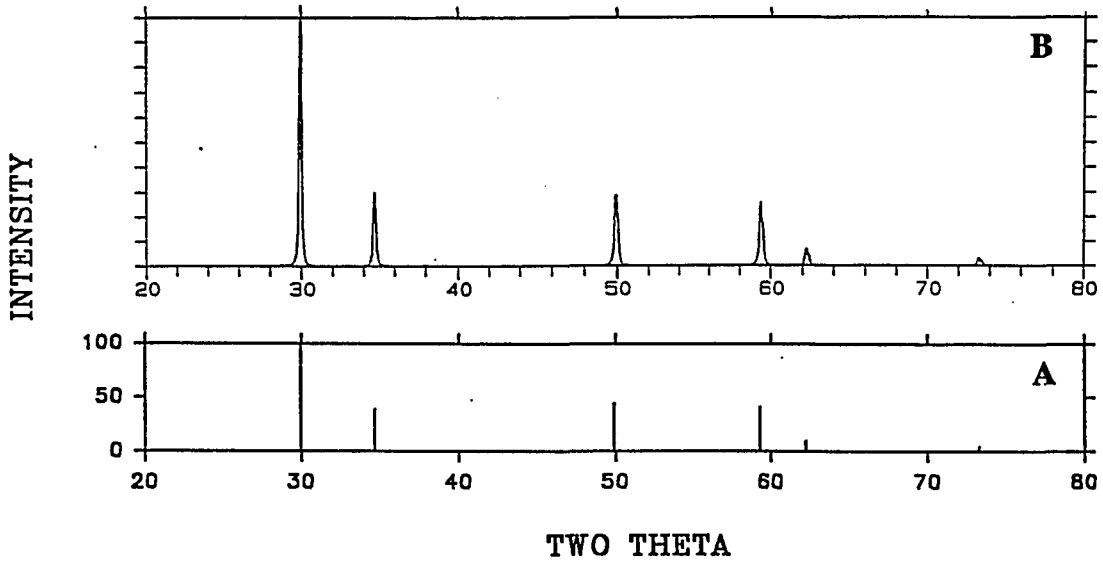

Figure 1. X-ray powder diffraction patterns: (A) theoretical for $Bi_2Ir_2O_7$, (B) prepared sample.

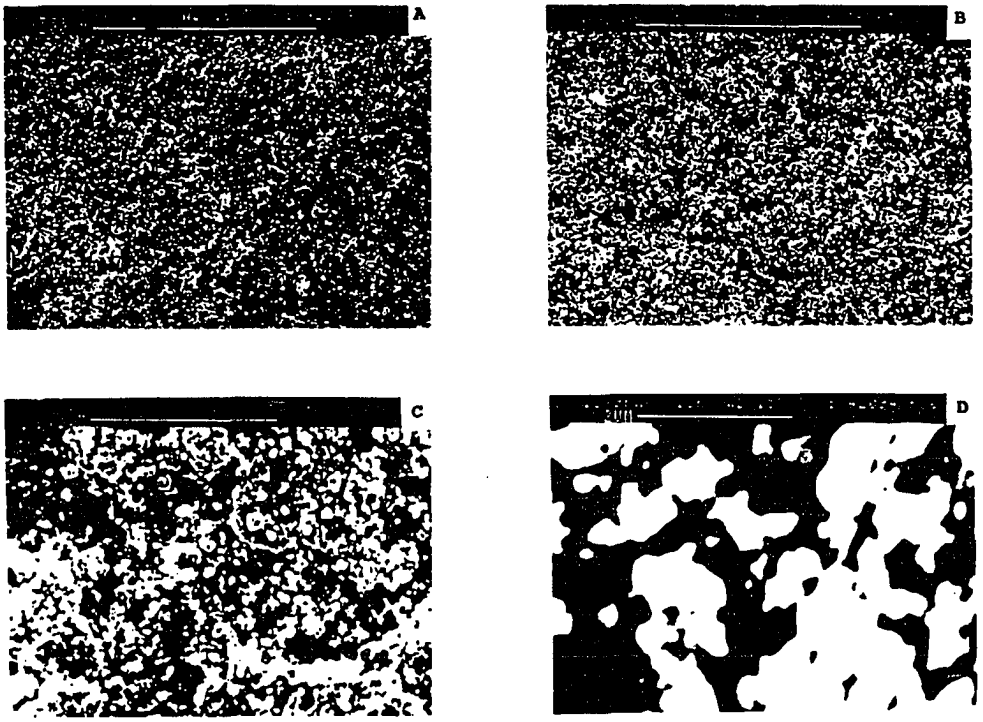

Figure 2. Micrographs of $Bi_2Ir_2O_7$ RDE-1.

the specific surface area. The absolute values of such parameters like crystallinity, crystal size and surface area may be drastically dependent on the specific characteristics of the compounds.[16] According to XRD and SEM, the particle size of $Bi_2Ir_2O_7$ (ca. 0.07 μm) is much smaller than that of $Bi_2Ru_2O_7$ (ca. 0.7 μm)[5] in spite of the fact that they were prepared under the same conditions. The high surface area of $Bi_2Ir_2O_7$ may be beneficial to its catalytical properties.

Voltammetric responses for oxidation of iodide.-Typical voltammetric response obtained in 0.10 M H_2SO_4 is shown in Figure 3A and 3B for the Ir and $Bi_2Ir_2O_7$ electrodes, respectively. Curves **a** and **c** correspond to the background response in the absence of I^- whereas curves **b** and **d** correspond to the total response for 3.0 mM I^-. A comparison of the background response (curves **a** and **c**) indicates that anodic discharge of H_2O with evolution of O_2 occurs at a significant rate at $E > 1.3$ V for both electrodes. In the background response (**a** and **c**), the observed currents in the region $0.0 < E < 1.3$ V are believed to be exclusively the result of double-layer charging processes. The obvious fact that the charging current for the $Bi_2Ir_2O_7$ electrode (RDE-I) is significantly larger than that for the Ir electrode is undoubtedly the result of the higher total surface area of this composite electrode as a consequence of high surface porosity (see Figures 2C and 2D). The porosity was decreased by increasing the cement-to-powder ratio and, therefore, the charging currents for RDE-II (data not shown) were significantly smaller than for RDE-I. Iridium electrodes are well known to form hydrous oxide surface layers under typical voltammetric conditions in acidic media.[18,19] However, anodic and cathodic currents from formation and reduction

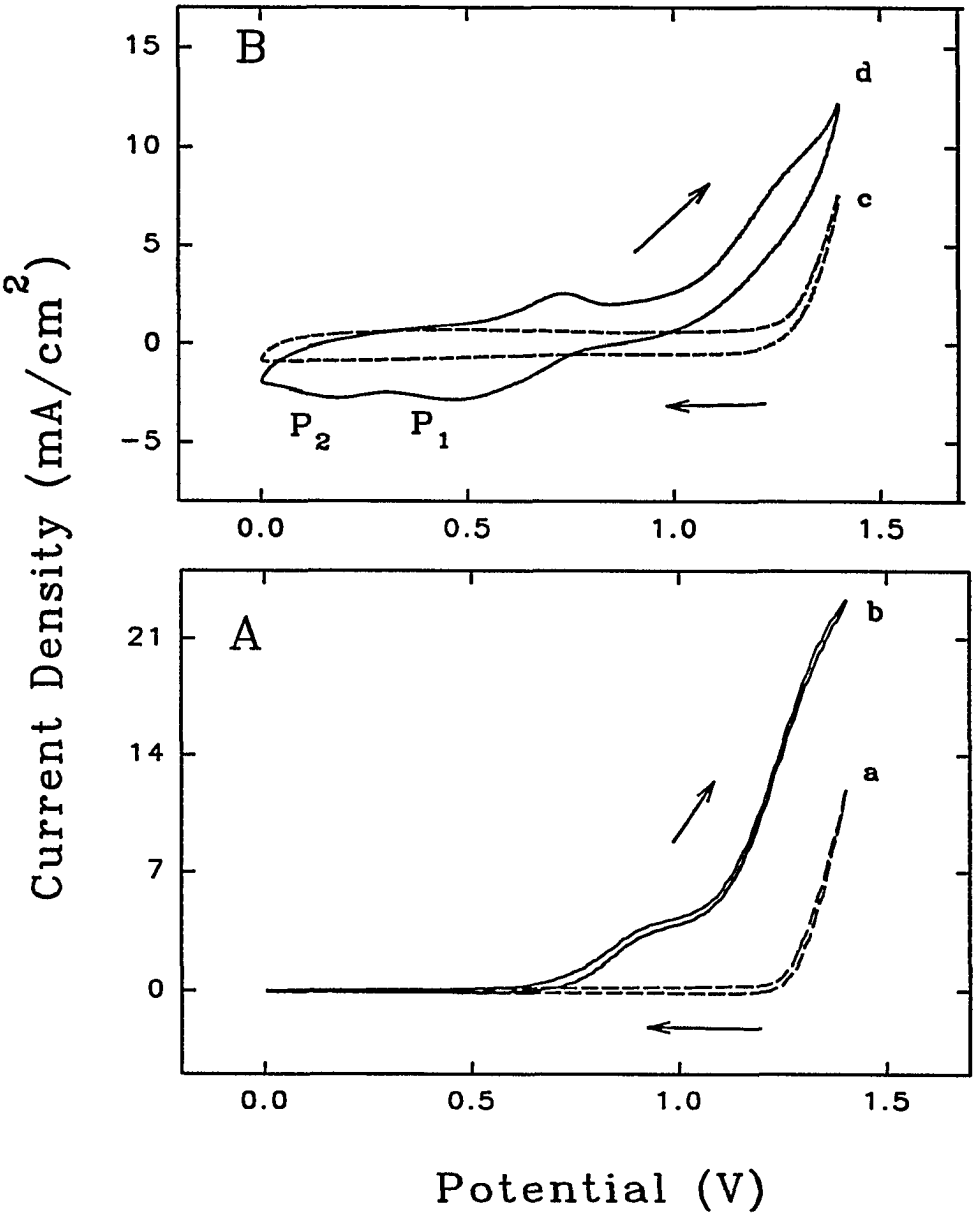

Figure 3. Cyclic voltammetric response for I^- at solid Ir RDE (A) and $Bi_2Ir_2O_7$ RDE-I (B). Concentration of I^- (mM): 0.0 (dashed lines), 3.0 (solid lines). Scan rate: 30 mV s^{-1}. Rotational velocity: 261.7 rad s^{-1}.

processes, respectively, related to the oxide layer in the potential regions shown are not observable in Figure 3 because of the low sensitivity used for the scaling of current response. Voltammetric data obtained in the presence and absence of dissolved O_2 (data not shown) revealed that O_2 reduction does not occur in the potential region indicated in Figure 3.

In the presence of I^-, anodic waves are clearly evident during the positive scans at both the Ir and $Bi_2Ir_2O_7$ electrodes (Figure 3). The first wave, observed at $E_{1/2}$ = 0.80 V for Ir (A) and at $E_{1/2}$ = 0.62 V for $Bi_2Ir_2O_7$ (B), is presumed to correspond to the oxidation of I^- to I_2. The $E_{1/2}$ values[8] at Pt, Au, Ir, and GC for oxidation of I^- to I_2 are in the range of 0.5 to 1.0 V. The second anodic wave, observed at $E \geq 1.1$ V for Ir (A) and $E > 1.0$ V for $Bi_2Ir_2O_7$, is tentatively concluded to correspond to the oxidation of I^- to IO_3^-. This second wave does not exhibit a clear limiting-current plateau, probably because of the contribution from concurrent anodic discharge of H_2O which increases rapidly with increasing potential for $E > 1.3$ V. The importance of the anodic discharge of H_2O in the oxygen-transfer mechanism for oxidation of I^- to IO_3^- has been discussed.[8] From Figures 3A and 3B, we estimate $E_{1/2}$ = 1.2 V for oxidation of I^- to IO_3^- at both the Ir and $Bi_2Ir_2O_7$ electrodes in this medium. This initial assignment of anodic reactions for the Ir electrode is supported by values for n_{eff}. *Values of* n_{eff} are estimated from linear regions of i-$\omega^{1/2}$ plots corresponding to background-corrected currents measured at 0.96 V and 1.28 V, which appear to correspond to values of transport-limited response for the two reactions. Accordingly, $n_{eff,1.28V}/n_{eff,0.96V}$ = 5.2 eq mol^{-1} for the Ir electrode which is in satisfactory agreement with the theoretical value of 6 eq mol^{-1} based on the assumption that the oxidation

products at 0.96 V and 1.28 V are I_2 and IO_3^-, respectively. The current density at RDE-I for oxidation of I^- in Figure 3B is obviously smaller than that in Figure 3A at Ir RDE because the current density was calculated based on the geometric area (A_{geom}) of RDE-I. According to SEM result, the active area (A_{act}) of RDE-I is about half the value of A_{geom}, i.e., $Bi_2Ir_2O_7$ RDE-I may have the characteristics of microelectrode arrays.

Clearly, the most obvious difference between Figures 3A and 3B is that there are two cathodic peaks obtained during the negative scan at the $Bi_2Ir_2O_7$ electrode having the peak potentials E_{p1} = 0.46 V and E_{p2} = 0.17 V. There are no cathodic peaks obtained for the Ir electrode. These cathodic peaks are attributed to the reduction of IO_3^- and/or I_2 trapped within pores near the electrode surface. Shown in Figure 4 are voltammetric curves obtained at the $Bi_2Ir_2O_7$ electrode (RDE-I) as a function of I^- concentrations during the positive (A) and negative (B) scans. The peaked form of the anodic wave for oxidation of I^- to I_2 and the presence of the cathodic peaks during the negative scan are consistent with expectations as a consequence of surface porosity.

Voltammetric responses for iodate.-The voltammetric response is shown in Figure 5 for the Ir (A) and $Bi_2Ir_2O_7$ (B) electrodes obtained in 0.10 M H_2SO_4 for IO_3^- at concentration of (mM) (a) 0.0, (b) 1.0, (c) 2.0, (d) 3.0, (e) 4.0 and (f) 5.0. For the solid Ir RDE (Fig. 5A), one cathodic wave is observed with $E_{1/2}$ = 0.65 V during the negative scan, which matched the reduction of IO_3^- to I_2 in the stationary solution as shown in Rodriguez and co-workers.[18] The peaked wave may be resulted by the absorbtion of reduction product I_2 which can decrease the active surface area of solid Ir electrode. The

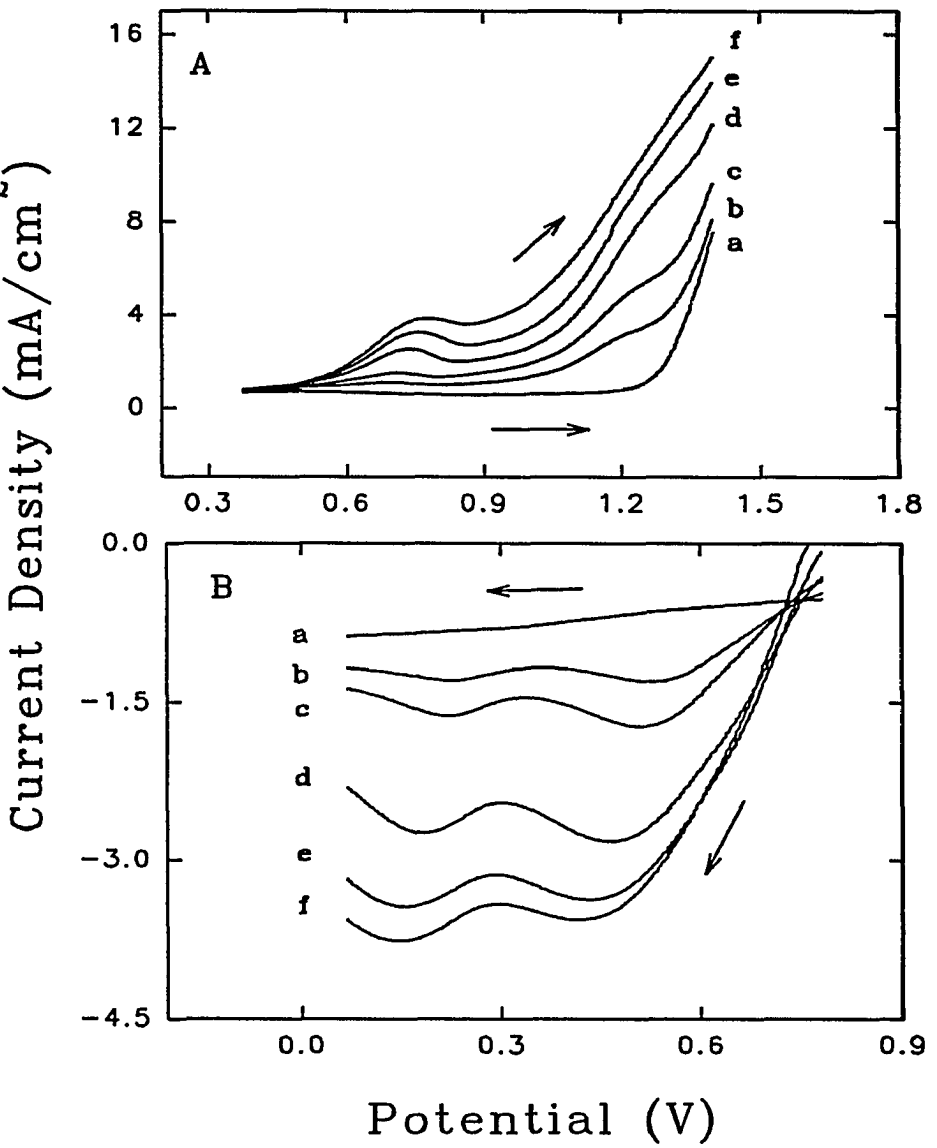

Figure 4. Voltammetric response at the $Bi_2Ir_2O_7$ RDE-I obtained during the positive scan (A) and negative scan (B) as a function of I^- concentration (mM): (a) 0.0, (b) 1.0, (c) 2.0, (d) 3.0, (e) 4.0 and (5) 5.0. Electrolyte: 0.10 M H_2SO_4. Rotational velocity: 261.7 rad s^{-1}. Scan rate: 30 mV s^{-1}.

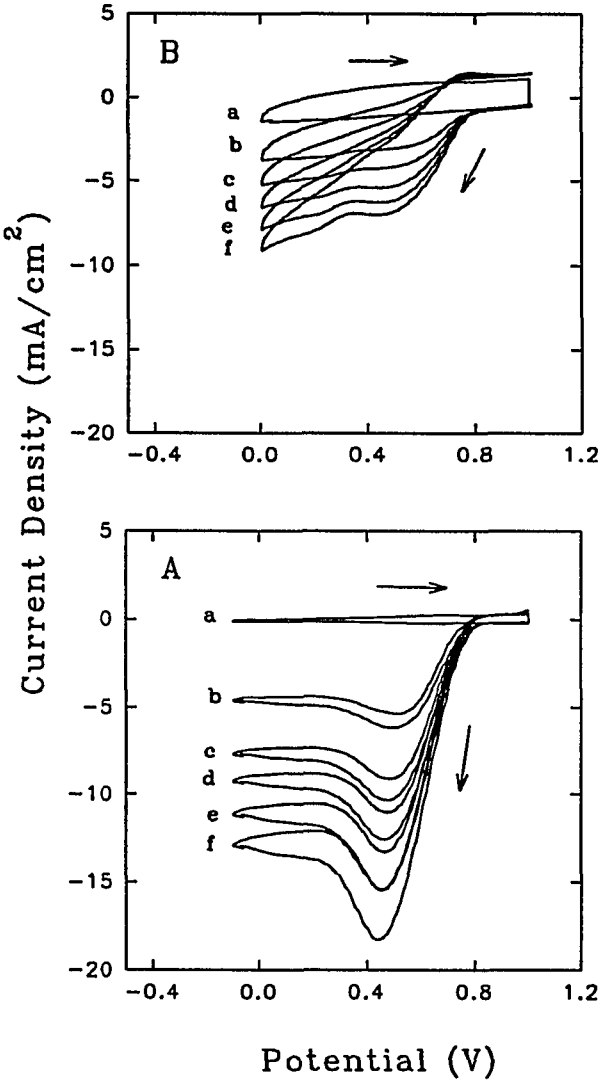

Figure 5A&B Cyclic voltammetric response at the Ir RDE (A) and $Bi_2Ir_2O_7$ RDE-1 (B) as a function of IO_3^- concentration (mM): (a) 0.0, (b) 1.0, (c) 2.0, (d) 3.0, (e) 4.0 and (5) 5.0. Electrolyte: 0.10 M H_2SO_4. Rotation rate: 261.7 rad s^{-1}. Scan rate: 30mV s^{-1}.

similar result was observed for solid Pt RDE.[10] For better understanding, more experimental results are needed, for example, using Ir ring disk electrode. In comparison, two cathodic waves are observed for the $Bi_2Ir_2O_7$ RDE-I. The first wave ($E_{1/2}$ = 0.66 V) is assumed to correspond to the reduction of IO_3^- to I_2 and the second ($E \leq 0.3$ V) is assumed to correspond to the reduction of I_2 to I^- (negative scan).

Figure 5C shows voltammetric data of $Bi_2Ir_2O_7$ RDE-II in the acidic solutions as a function of IO_3^- concentrations (mM) which are (a) 0.0, (b) 1.0, (c) 2.0, (d) 3.0, (e) 4.0 and (f) 5.0. The residual currents in Figure 5C are smaller than those in Figure 5B throughout the potential region examined because the larger polymer content of the composite material for RDE-II results in less porosity at the RDE-II surface with the result of a smaller value for the effective area of this composite electrode. As expected, the current response at RDE-II as a function of IO_3^- concentration is smaller than for RDE-I under the same conditions of concentration and rotational velocity. This is evidence for a smaller active area at RDE-II. The cathodic wave observed at $E_{1/2}$ = 1.05 V in Figure 5C corresponding to the reduction of IO_3^- to I_2 is shifted to more positive with increasing O_2 overpotential at RDE-II as comparing to the first cathodic wave ($E_{1/2}$ = 0.66 V) in Figure 5B. This is interpreted to be an indication of differences in the adsorption energies for OH_{ads} species at the two electrodes.

An anodic wave at $E_{1/2}$ = 1.45 V for RDE-II was not observed during the first cyclic scan in a fresh solution of IO_3^-. However, the wave increased slowly with subsequent scans. This is evidence for the slow buildup of I_2 and/or I_3^- in the bulk solution as a product of the

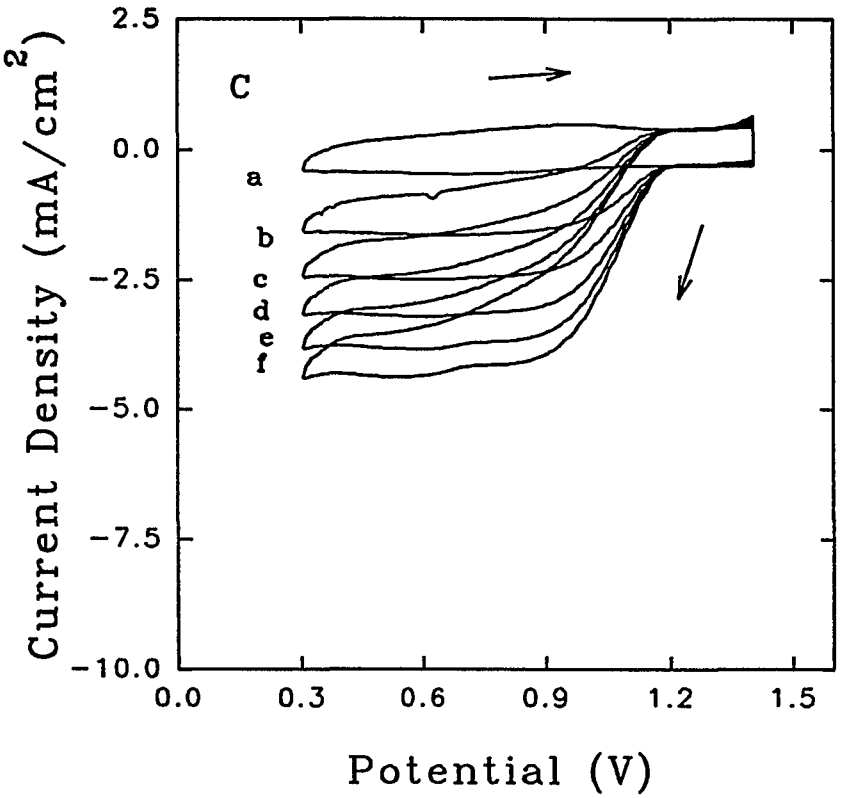

Figure 5C Cyclic voltammetric response at $Bi_2Ir_2O_7$ RDE-2 (C) as a function of IO_3^- concentration (mM): (a) 0.0, (b) 1.0, (c) 2.0, (d) 3.0, (e) 4.0 and (5) 5.0. Electrolyte: 0.10 M H_2SO_4. Rotation rate: 261.7 rad s^{-1}. Scan rate: 30mV s^{-1}.

homogeneous reaction between IO_3^- and I^-. Further evidence supporting this conclusion was the concomitant increase in yellowish color of the solution.

Variation of Scan Rate.-Variation of the potential scan rate (ϑ) in voltammetric studies can be useful for discriminating between surface-controlled and transport-controlled faradaic processes. For the $Bi_2Ir_2O_7$ RDE-I and RDE-II , the residual curves were dependent on the scan rates. The difference voltammetric responses were applied to show that the pure current responses depend on scan rates. In difference voltammetry, each Δi-E curve was obtained by extracting the current for the reaction of interest from the residual curve at the same scan rate. In this study, scan rate was varied in the range 10 - 90 mV s^{-1}. Difference voltammetric curves recorded as a function of scan rate (ϑ) are shown in Figure 6 for the Ir RDE (A) and for $Bi_2Ir_2O_7$ RDE-I (B). For the Ir RDE, the plateau currents were virtually independent of scan rate, which is representative of the characteristic of transport controlled process. The observed variation of peak height as a linear function of ϑ is expected for surface-controlled reactions. The heights of peaks (P_1), (P_2) and (P_4) at RDE-I in Fig. 6B on the negative and positive scans varied nonlinearly with ϑ and similar results were obtained for RDE-II. This is indicative of mixed control by surface and transport controlled processes at the $Bi_2Ir_2O_7$ RDE-I and RDE-II.

Figure 7 shows the difference voltammograms (Δi-E) for Ir RDE (A) and $Bi_2Ir_2O_7$ RDE-I (B) obtained by subtracting the i-E responses obtained at 400 rev min^{-1} from 1600 rev min^{-1} at same initial concentration of IO_3^- (1.0 mM). These Δi-E data discriminate against double-layer charging, formation and dissolution of surface oxide, and the anodic evolution

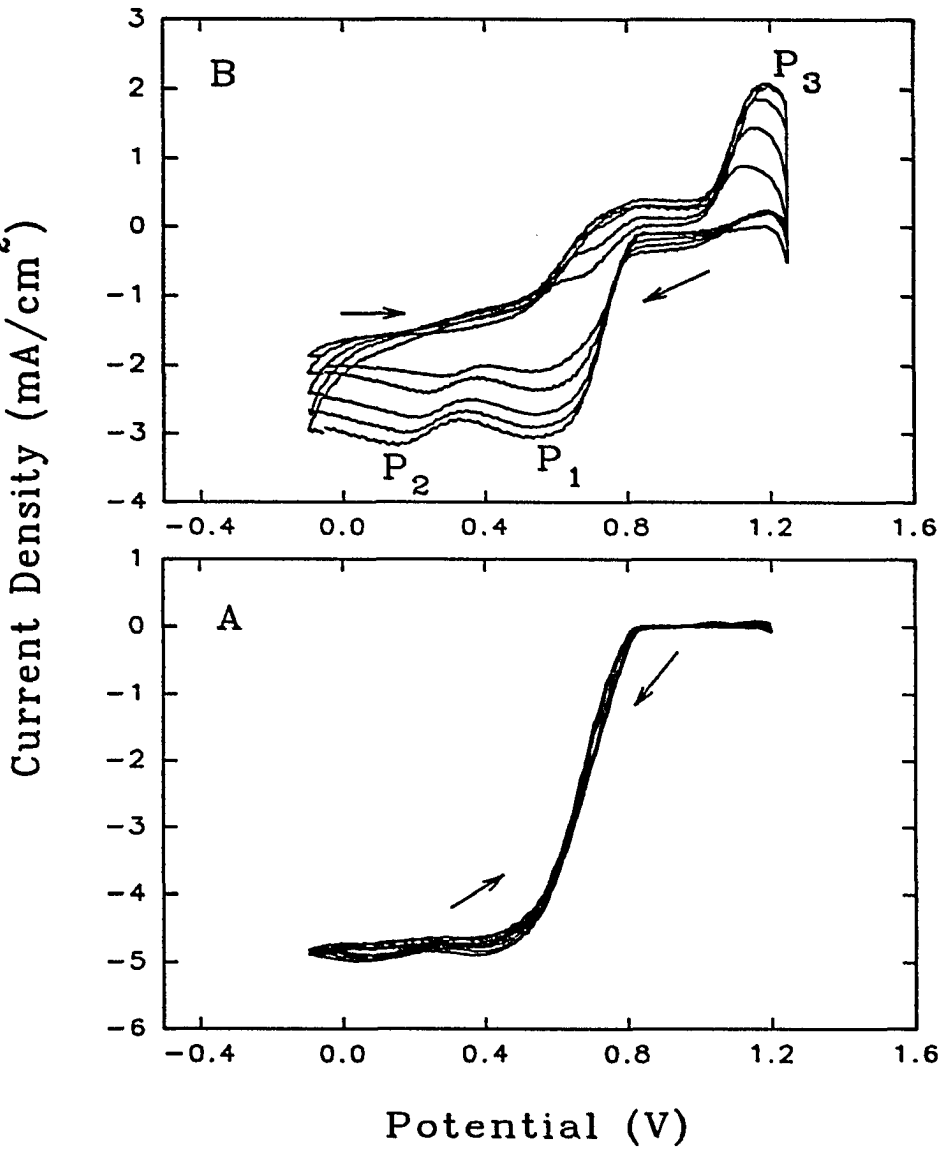

Figure 6. Difference voltammetric response (Δi-E) for 1.0 mM IO_3^- at the Ir RDE (A) and $Bi_2Ir_2O_7$ RDE-I (B) as a function of scan rate (mV s^{-1}): (a) 10, (b) 30, (c) 50, (d) 70, and (e) 90. Electrolyte: 0.10 M H_2SO_4. Rotational velocity: 261.7 rad s^{-1}.

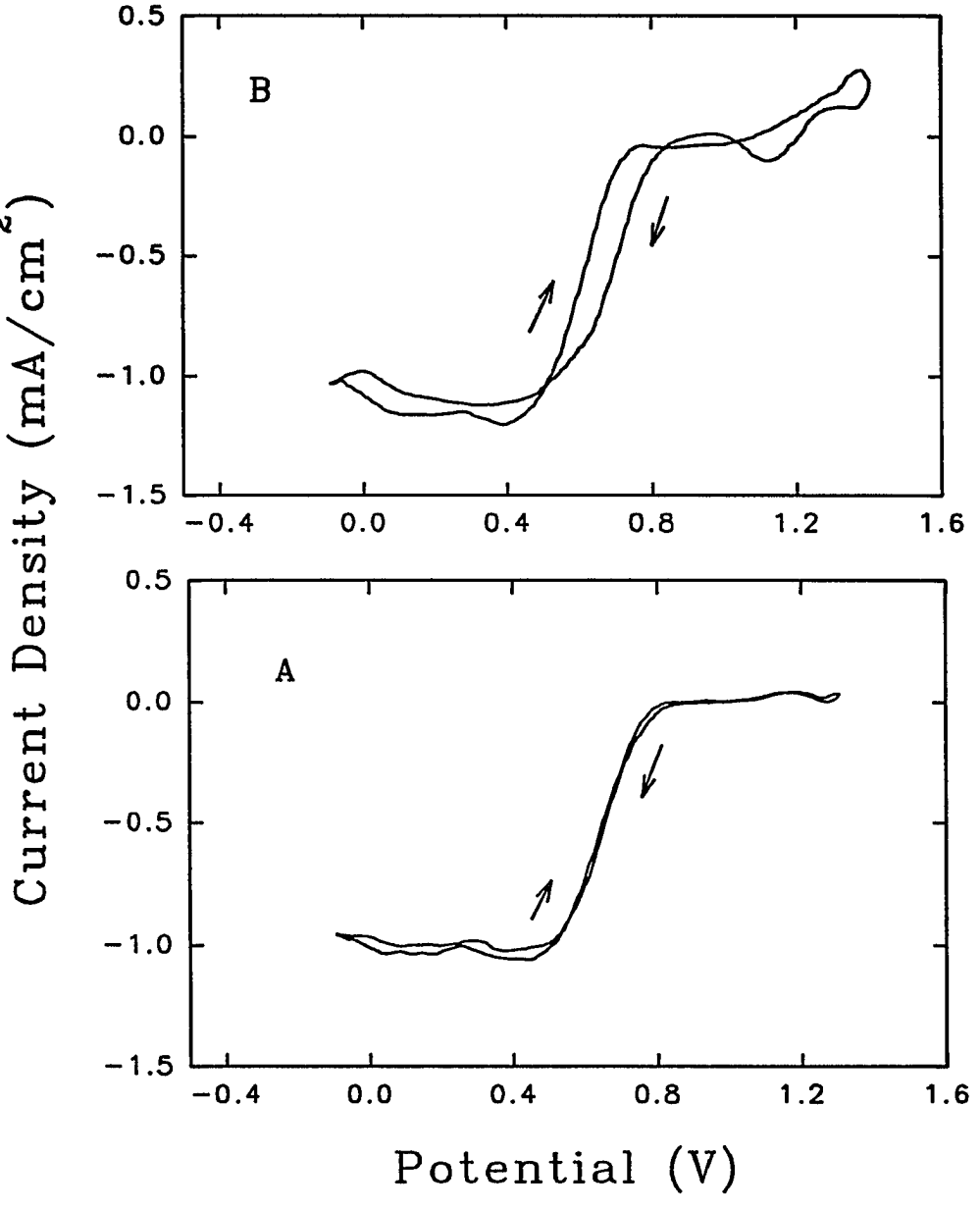

Figure 7. Difference voltammetric response (Δi-E) for 1.0 mM IO_3^- at solid Ir RDE (A) and $Bi_2Ir_2O_7$ RDE-1 (B). Electrolyte: 0.10 M H_2SO_4. Rotational velocity: 168 rad s^{-1} and 42 rad s^{-1}. Scan rate: 30 mV s^{-1}.

of O_2. The current density for the reduction of IO_3^- at the $Bi_2Ir_2O_7$ RDE-I is a little bit larger than that at the Ir RDE. This characteristic of composite electrodes displays the optimum result in the enhancement of current density as comparing with solid Ir RDE, even though A_{geom} of the $Bi_2Ir_2O_7$ composite RDE was used to calculate the current density, and it is clearly observed by scanning electron spectroscopy (Figure 2A - 2D) that the active surface area (A_{act}) of the $Bi_2Ir_2O_7$ composite RDE is smaller than geometric area (A_{geom}). This result expresses that $Bi_2Ir_2O_7$ composite RDE is a better electrode as compared with solid Ir electrode especially in the enhancement of current density.

Variation of rotational velocity.-Amperometric data were obtained as a function of rotational velocity for the reduction of IO_3^-. Typical results are summarized in Figure 8 as Levich plots (i-$\omega^{1/2}$) for the $Bi_2Ir_2O_7$ RDE-I at 0.57 V (A) and 0.15 V (B), and the Ir RDE at 0.44 V (C). These plots for the $Bi_2Ir_2O_7$ RDE-I are linear ($r \geq 0.998$), as expected for processes under mass transport control, but with a nonzero intercept. Combining the results obtained from variation of scan rates, it is indicative of the simultaneous occurrence of surface-controlled and transport-controlled reduction of IO_3^- at $Bi_2Ir_2O_7$ RDE-I. The Levich plot for the Ir RDE (C) is not linear which is evidence for a mixed transport-kinetic controlled reaction. It is evident again that $Bi_2Ir_2O_7$ RDEs have better correspordent for transport-controlled reactions. Regression statics for the linear segment constructed having a zero intercept in the plot (Fig.8C) are indicated by: $i = b\omega^{1/2}$ where $b = 0.181$ mA $s^{-1/2}$. From this slope, the value $n_{eff} = 5.9$ eq mol^{-1} was calculated using $A_{geom} = 0.5024$ cm^2, $\nu = 0.010$ cm^2 s^{-1}, and assuming $D = 1.0 \times 10^{-5}$ cm^2 s^{-1}. The value of n_{eff} calculated for the

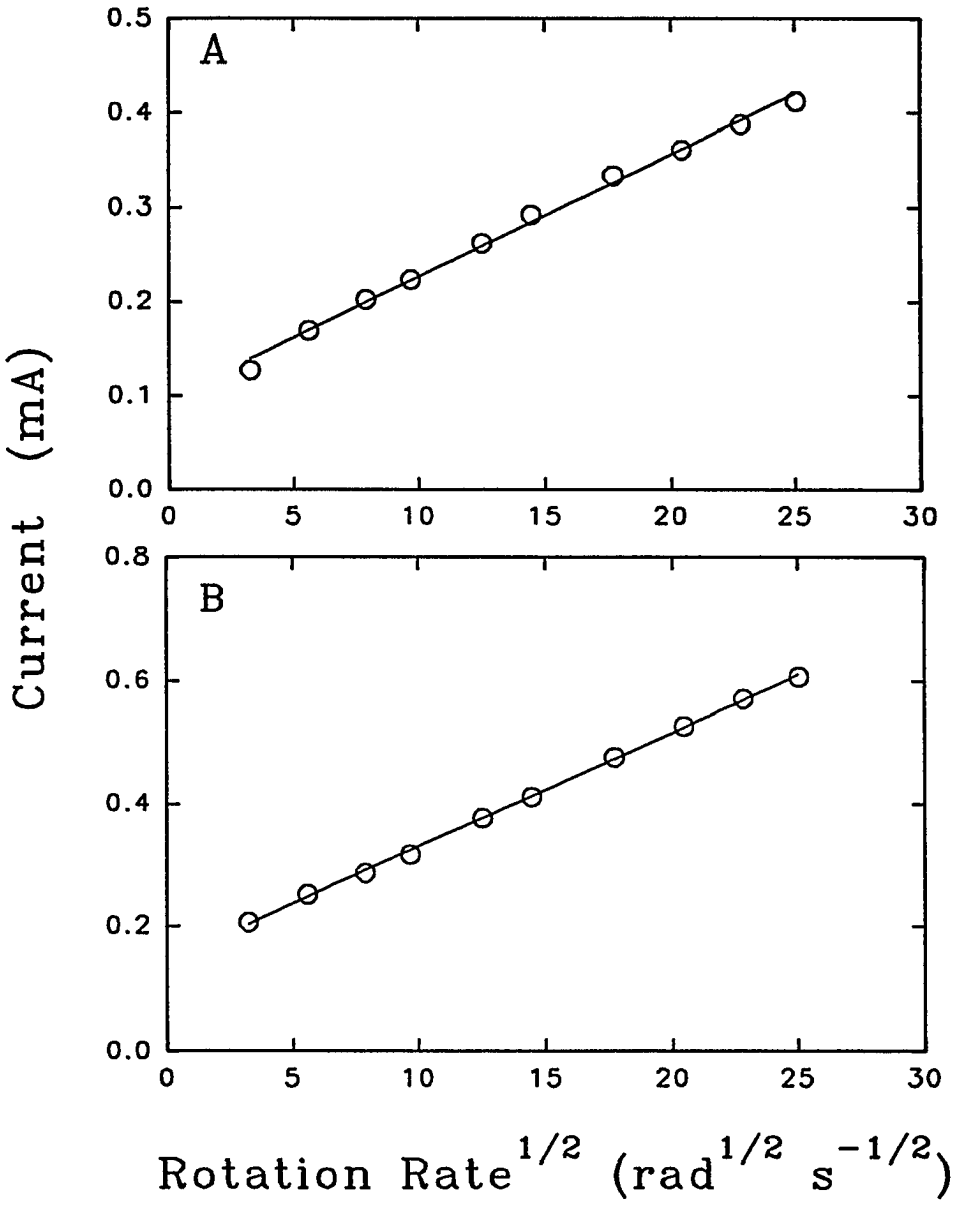

Figure 8A&B Levich plots of background-corrected current for reduction of 1.0 mM IO_3^- on $Bi_2Ir_2O_7$ RDE-1 at 0.57 V (A) and 0.15 V (B). Electrolyte: 0.10 M H_2SO_4.

cathodic wave of the solid Ir RDE is close to the expected value for IO_3^- to I_2 (5 eq mol^{-1}). For the $Bi_2Ir_2O_7$ RDE-I, the ratio of $(\Delta i_{0.57V}/\Delta\omega^{1/2})/(\Delta i_{0.15V}/\Delta\omega^{1/2})$ was applied to estimate $n_{eff,0.57V}/n_{eff,0.15V} = 0.98$ which is in satisfactory agreement with the theoretical value of 1 based on the assumption that the reduction products at 0.57V and 0.15V are I_2 and I^-, respectively. According to above calculation, it is concluded that the reduction of IO_3^- during the negative scan at the $Bi_2Ir_2O_7$ RDE-I can yield I_2 ($0.8 \leq E \leq 0.3$) and I^- ($E \leq 0.3$) with the result that I_2 is absorbed at the oxide surface.

Figure 8D shows the Levich plot for $Bi_2Ir_2O_7$ RDE-II at constant potential 0.7 V in the acidic media. Curvature observed in this i-$\omega^{1/2}$ plot at composite rotating disk electrode can be rationalized on the basis of significant overlap of adjacent diffusion zones when the distance between adjacent active regions is comparable to the diffusion-layer thickness at the electrode surface. The characteristics of RDE-II are closer to those of microelectrode arrays, compared to RDE-I, when the blocking factor is increased in the RDE-II.

Conclusions

The $Bi_2Ir_2O_7$ composite material can be used as an electrochemical catalyst for both anodic oxidation of iodide and cathodic reduction of iodate in acidic medium (0.1M H_2SO_4). The characteristics of the pyrochlore oxide $Bi_2Ir_2O_7$ electrode material are similar to those of the solid Ir electrode. The pyrochlore oxide $Bi_2Ir_2O_7$ electrode material is better than solid Ir in the enhancement of current density and for the transport-controlled reactions. The qualitative conclusion drawn from this study is that the catalytic activity depend on the

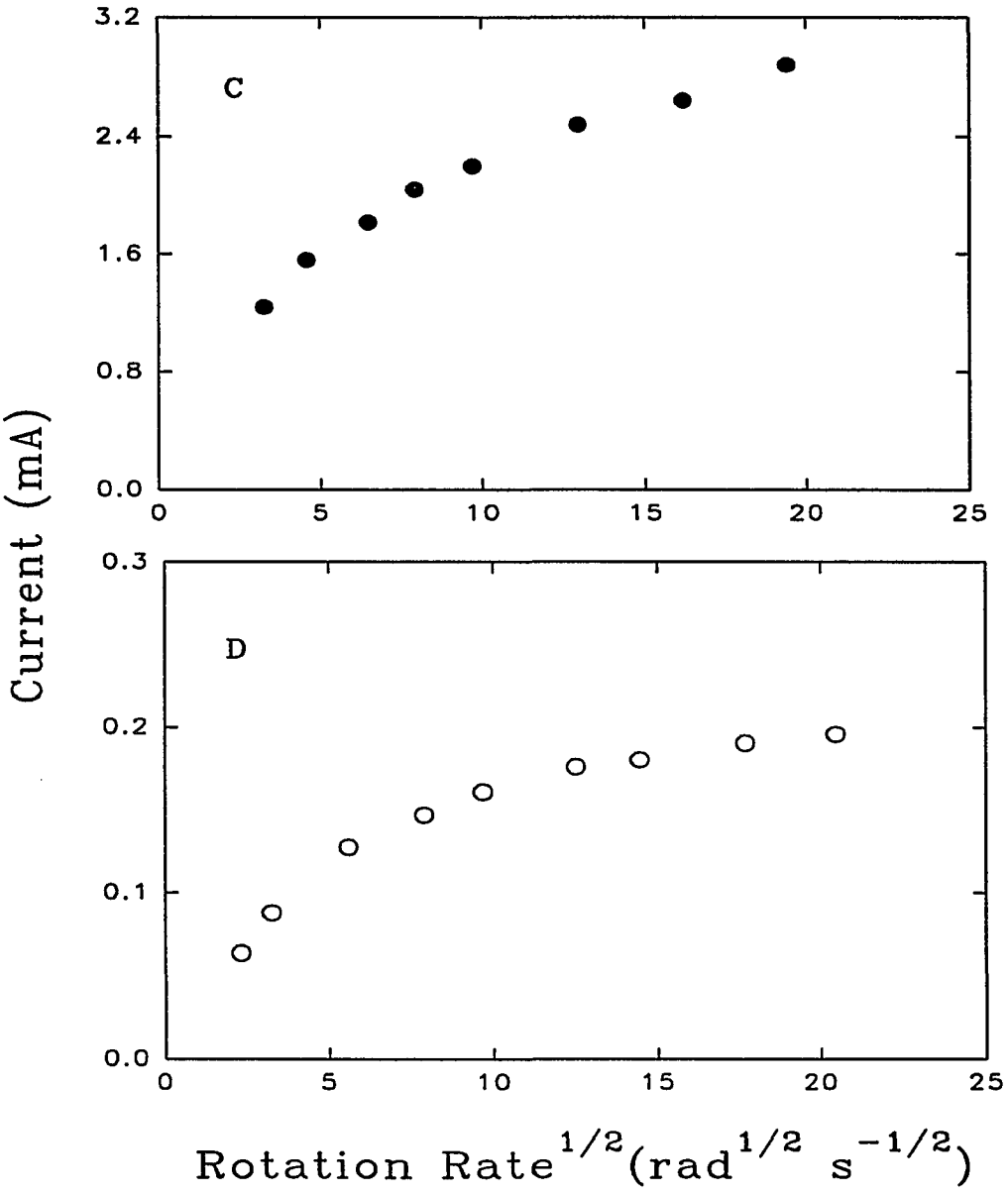

Figure 8C&D Levich plots of background-corrected current for reduction of 1.0 mM IO_3^- on Ir RDE at 0.44 V (C) and on $Bi_2Ir_2O_7$ RDE-2 at 0.70 V (D). Electrolyte: 0.10 M H_2SO_4.

material itself.

Rodriguez *et al.* concluded for polycrystalline Ir that desorption of iodine occurs after hydrogen gas is evolved in acid.[18] Under our experimental conditions, only one cathodic wave was observed for solid Ir RDE for the reduction of IO_3^- to I_2 in the potential range between 0.0 V and 1.3 V. This is in agreement with Rodriguez *et al.*[18] But during the negative scan in the potential range between 0.0 V and 1.3 V, there were two cathodic waves for the $Bi_2Ir_2O_7$ composite RDE corresponding to the reduction of IO_3^- to I_2 and I_2 to I^-.

The plateau currents of reduction of IO_3^- for solid Ir RDE were virtually independent of scan rate, which is representative of a purely transport-controlled process. The plateau currents varied nonlinearly with scan rates at the $Bi_2Ir_2O_7$ composite electrode, which is indicative of mixed control by surface- and transport-controlled processes.

The values of the current at E = 0.57 V and 0.15 V at the $Bi_2Ir_2O_7$ composite RDE on the negative scan increased as a linear function of $\omega^{1/2}$ but with a nonzero intercept, which is indicative of the simultaneous occurrence of surface-controlled reduction and transport-controlled reaction of IO_3^- at the $Bi_2Ir_2O_7$ composite RDE. Linearity of i^{-1}-$\omega^{-1/2}$ plots is evidence that reduction of IO_3^- at the Ir RDE occurs by a mixed transport-kinetic controlled mechanism.

Acknowledgement

Ames Laboratory is operated for the U.S. Department of Energy by Iowa State University under Contract No. W-7405-ENG-82. This research was supported by the

Director for Energy Research, Office of Basic Energy Sciences.

References

[1] T. Yamamoto, R. Kanno, Y. Takeda, O. Yamamoto, Y. Kawamoto, and M. Takano, *J. Solid State Chem.* **109**, 372 (1994).

[2] R. Kanno, Y. Takeda, T. Yamamoto, Y. Kawamoto, and O. Yamamoto, *J. Solid State Chem.* **102**, 106 (1993).

[3] P. A. Cox, J. B. Goodenough, P.J. Tavener, and D. Telles, *J. Solid State Chem.* **62**, 360 (1986).

[4] R. G. Egdell, J. B. Goodenough, A.Hamnett, and C.C. Naish, *J. Chem. Soc., Faraday Trans. 1* **79**, 893 (1983).

[5] L. He, H. F. Franzen, and D. C. Johnson, *J. Electrochem. Soc.*, submitted.

[6] R. J. Bouchard, and J. L. Gillson, *Mat. Res. Bull.* **6**, 669 (1971).

[7] H. S. Horowitz, J. M. Longo, and H. H. Horowitz, *J. Electrochem. Soc.*, **130**, 1851 (1983).

[8] J. E. Vitt and D. C. Johnson, *J. Electrochem. Soc.*, **139**, 774(1992).

[9] P. Beran, and S. Bruckentein, *Anal. Chem.*, **40**, 1044 (1968).

[10] B. R. Wels, D. S. Austin-Harrison, and D.C. Johnson, *Langmuir*, **7**, 559 (1991).

[11] V. G. Levich, *Physicochemical Hydrodynamics*, Prentice Hall: Englewood Cliffs, NJ, p.75(1962).

[12] J. Koutecky and V. G. Levich, *Dokl.Akad.Nauk. SSSR*, **117**, 441 (1957); *Zh. Fiz. Khim.*, **32**, 1565 (1958).

[13] JCPDS (file No.41-953) International Center for Diffraction Data, 1601 Park Lane, Swarthmore, PA (1992).

[14] A. Guinier, X-Ray Diffraction, W.H. Freeman and Co., San Francisco, and London, p.121 (1963).

[15] H. Schafer, *Chemical Transport Reactions*, Academic Press, New York, ch.6,(1964).

[16] S. Trasatti, *Electrodes of Conductive Metallic Oxides*, Elsevier Scientific Publishing Company, 1980.

[17] J. O. Bockris and A. K. N. Reddy, *Modern Electrochemistry*, Plenum Press, New York, Vol.2(1972).

[18] J. F. Rodriguez, M. E. Bothwell, J. E. Harris and M. P. Soriaga *J. Phys. Chem.* **92**, 2702 (1988).

[19] P. G. Pickup and V. I. Birss, *J. Electroanal. Chem.*, **92**, 83 (1987).

[20] D. C. Johnson, *J. Electrochem. Soc.*, **119**, 331 (1972).

SYNTHESIS AND CHARACTERIZATION OF $Pt\text{-}Ti_4O_7$ MICROELECTRODE ARRAYS

A paper to be submitted to *J. Electrochem. Soc.*

Lin He, Hugo F. Franzen and Dennis C. Johnson

Abstract

The synthesis and characterization of $Pt\text{-}Ti_4O_7$ microelectrode arrays have been studied in this work. Data obtained by x-ray diffractometry and scanning electron microscopy are consistent with the existence of heterogeneous mixtures of Pt particles imbeded within the Ti_4O_7 matrix. Rotated disk electrodes (RDEs) constructed from the $Pt\text{-}Ti_4O_7$ materials are compared on the basis of their voltammetric and amperometric responses for the oxidation of I^- and redox of H_2O_2 in acidic media. Significant enhancement of current densities has been observed and rationalized on the basis of microelectrode arrays.

Introduction

Significant advances in electrochemistry have resulted from improvements in the sensitivity, selectivity, convenience, and/or economy of the working electrode. This is why research in the areas of microelectrodes, chemically modified electrodes, and new

composite electrode materials is so important.

The search for efficient and inexpensive catalysts represents a challenging problem that continues to occupy the time and effort of many researchers today. Platinum is a typical catalyst widely used in industries and research laboratories and dominates the cost of the cell. Since a suitable replacement for platinum has not been found, another approach is necessary to decrease overall costs, maintain the same catalytic properties and even achieve higher signal-to-noise ratios. Methods for the synthesis of new Pt microelectrode arrays are in high demand and the understanding of their characteristics is very important.

Conventionally, a composite electrode was as a surface consisting of an ordered or a random arrangement of conducting regions, typically microscale in dimension, separated from one another by an insulator (*e.g.*, Kel-F) to bind the microelectrode particles into physically stable arrangements.[2-4] However, to achieve the optimal fractional active area of *ca.* $\leq 1.7\%$, as suggested by Weber for microelectrode arrays,[9] it has been necessary to incorporate graphite particles within the plastic matrices to achieve electrical connectivity between the microelectrodes. In a study of these so-called "Kelgraf electrodes" containing small Au particles,[4] current densities were more than 10 times larger in comparison to those for the same reaction at pure Au electrodes of large geometry. However, two major disadvantages were recognized when using graphitic powder in the fabrication of these composite electrodes.[4] First, loss of graphite occurred at the surface when the composite materials were subjected to mechanical polishing. Hence, it is apparent that some metal particles can be lost and there can be a sacrifice in electrical connectivity between the

remaining metal particles. Second, graphite is a useful electrode material for many faradaic reactions and, therefore, its use is undesirable in the fabrication of metal microelectrode arrays.

Significant advantages can result from fabrication of microelectrode arrays using matrices (binders) that are both electrically conductive and electrochemically inert. An excellent example of this kind of microelectrode arrays is Ru-Ti_4O_7 RDEs[25], for which Ti_4O_7 is an attractive matrix material with both electrical conductivity and electrochemical inertness. This ceramic material is one of the Magneli phases (Ti_nO_{2n-1}), it has a high conductivity (*ca.* 10^3 Ω^{-1} cm^{-1}), and is very stabile in a variety of corrosive media. [10,11] Furthermore, the desired electrochemical inertness of Ti_4O_7 is indicated by the large values of overpotential reported for anodic and cathodic evolution of O_2 and H_2, respectively, in aqueous media. [10,11] Possible applications of Ti_4O_7 in electrolytic processes have been described in reviews [10,11] and patents. [12,13] As expected for microelectrode arrays, a significant enhancement in current density was observed for Ru-Ti_4O_7 RDEs in comparison to solid Ru RDE.[25] The largest values of relative current density for the oxidation of I^- to I_2 and I^- to IO_3^- were 23 and 20 at the lowest rotation speed (10.5 rad s^{-1}) and the optimal ratio of active area (1%).

The goal of this work is to determine if platinum microelectrode could been made using Ti_4O_7 as the binder and to study electrocatalytic properties of Pt-Ti_4O_7 RDEs as compared with those of pure Pt RDE. Here we report on efforts to generate arrays of Pt microelectrodes within conductive Ti_4O_7 matrices. X-ray diffraction and scanning electron

micrographic data are presented along with voltammetric and amperometric results for the oxidations of I^- to I_2 and IO_3^- and the oxidation of H_2O_2 to O_2 in 0.10 M H_2SO_4.

Experimental

Reagents.—The potassium iodide was a reagent grade chemical (Fisher) and the water was purified in a Milli-Q system (Millipore) after passage through two D-45 deionizing tanks (Culligan). The solutions of 0.10 M H_2SO_4 were prepared by dilution of the concentrated reagent grade chemical (Mallinckrodt) in deionized water.

Electrode fabrication.—The Pt-Ti_4O_7 composite materials were prepared by mixing the appropriate quantities of TiO_2 (Fisher), Ti_2O_3 (Johnson Matthey), and Pt (Aldrich Chem. Co., 0.8-2.2μm diameter). Each mixture was ground in an agate mortar until a uniform color was obtained. Several drops of polyvinyl acetate (1% by vol.) in ethanol were added to the mixture to produce a paste which was pressed into a cylindrical pellet (9-mm dia., 12-mm length) in a laboratory press (Carve) at a pressure of 3 tons cm^{-2}. Pelletization improved contact between particles and, thereby, increased diffusion rates during thermal processing.

The pellets were dried at 150 °C for 1 day and then placed in a tungsten Knudsen cell in an induction furnace. The temperature of the tungsten crucible was monitored using an optical pyrometer. The residual pressure in the furnace was lowered to $< 10^{-5}$ torr using an oil-diffusion pump backed by a mechanical pump. The temperature was then slowly increased to 800 °C and held constant for *ca.* 1 hr to evaporate all traces of organic

material. The temperature was then slowly increased to 1300 °C, under a vacuum of *ca.* 10^{-6} torr, and held constant for 5 hr. Heating was terminated and the sample quenched by radiative heat loss in vacuum, allowing the sample to reach room temperature in *ca.* 2.5 hr.

Disk electrodes were assembled by mounting thermally processed pellets into a metal socket at the end of a stainless steel shaft which could be inserted into the rotator assembly. Cylindrical surfaces of these pellets were coated with wax to prevent their contact with the aqueous test solutions and, furthermore, only the end (disk) surfaces were allowed to contact solutions during use.

Active surface areas (A_{act}) for Pt-Ti_4O_7 electrodes were calculated from the geometric areas (A_{geom}) and the volume fractions of Pt according to:

$$A_{act} = [\,(V_P/(V_T + V_P)]A_{geom}$$

$$= (d_T/d_P)(M_P/M_T)(N_P/N_T)A_{geom} \qquad [1]$$

where V, d, M and N represent the volume, density, molecule weight, and number of moles, respectively; and the subscripts P and T designate Pt and Ti_4O_7, respectively.

X-ray diffractometry.—X-ray diffraction (XRD) data were obtained with an XDS-2000 (Scintag) diffractometer using Cu-Kα_1 radiation. The sample was rotated during data collection to reduce effects of preferred orientation.

Microscopy.—Micrographs and elemental analyses were obtained using a S-2460N

scanning electron microscope (SEM; HITACHI) equipped with a LINK ISIS energy dispersive X-ray spectrometer (EDS; OXFORD).

Voltammetry.— Voltammetric data were obtained using a RDE4 potentiostat and AFMSRX rotator (Pine Instrument Co.) interfaced with a 486 computer by a DT2800-A interface (Data Translation) using ASYST-3.1 software (Keithley-ASYST). The electrochemical cell was constructed from Pyrex with porous glass disks separating the working, reference and counter electrode compartments. All potentials are reported in volts *vs.* a saturated calomel electrode (SCE; Fisher Scientific). The counter electrode was a coiled Pt wire (*ca.* 7.6 cm^2).

The mass transport-limited current at a uniformly accessible RDE ($\theta = 0$) is a linear function of $\omega^{1/2}$ [7] and only observation of negative deviation from linearity in i-$\omega^{1/2}$ plots is interpreted to indicate the faradaic reaction occurs under mixed control by mass-transport and kinetic processes. Data of this type are often plotted as i^{-1} *vs.* $\omega^{-1/2}$ according to: [7]

$$i^{-1} = (nFA_{geom}k_{app}C^b)^{-1} + (0.62nFA_{geom}D^{2/3}\nu^{-1/6}C^b\omega^{1/2})^{-1} \quad [2]$$

where A_{geom} is the geometric area (cm^2), ν is the solution kinematic viscosity ($cm^2\ s^{-1}$), k_{app} is the apparent heterogeneous rate constant (cm s^{-1}), and n, F and C^b have their usual electrochemical significance. The plot of i^{-1} *vs.* $\omega^{-1/2}$ for a reaction under mixed control at a RDE with $\theta = 0$ is linear with a slope proportional to n^{-1} and an intercept proportional to k_{app}^{-1}.

Results and discussion

XRD and SEM data.—Figure 1A contains the XRD pattern for pure Pt metal. [14] Figure 1B contains the XRD pattern of Ti_4O_7 prepared by the method described but in the absence of Pt. This diffraction pattern is in good agreement with that reported for a single Ti_4O_7 crystal by Le Page and Marezie. [15] Figures 1C - 1F contain XRD patterns for Ti_4O_7 samples containing various amounts of Pt. These patterns correspond exactly to combinations of the patterns in Figures 1A & 1B which indicates these samples correspond to heterogeneous mixtures of pure Pt and Ti_4O_7, and there is no evidence that new compounds are formed in which Pt is incorporated within the Ti_4O_7 lattice. Hence, on this basis, it is expected that the Pt is distributed throughout the Ti_4O_7 matrices in the form of small metallic particles, *i.e.*, microelectrodes. The average grain size in the samples was estimated on the basis of the Fresnel Construction [16] and determined to be on the order of 0.88 μm.

Planar surfaces of electrodes were examined using SEM and typical micrographs are shown in Figures 2A - 2D as a function of increasing Pt content. During the experiment, the back scattering emission was applied to discriminate the Pt particles from the matrix. It is evident that the bright spots (Pt particles) are increased in number with increasing Pt content in the mixture of starting materials. The results of SEM-EDS applied to the surfaces shown in Figure 3 revealed that only the bright spots in these micrographs correspond to discreet Pt particles. The EDS spectra shown in Figure 3 were obtained under the conditions (A) with bright spots and (B) without bright spots in Figure 2A for

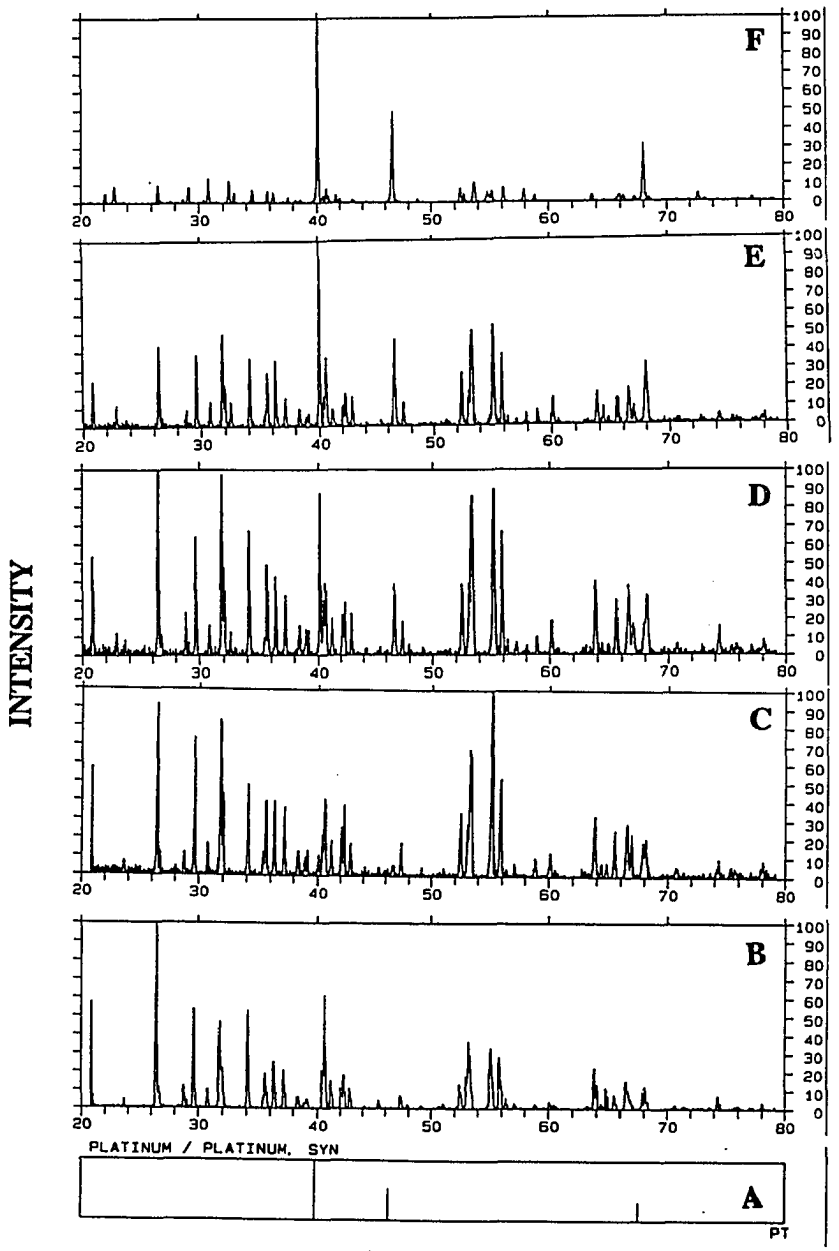

Figure 1. X-ray powder diffraction patterns. Materials: (A) Pt, (B) Ti_4O_7, (C) 0.1% Pt-Ti_4O_7, (D) 0.5% Pt-Ti_4O_7, (E) 1% Pt-Ti_4O_7, (F) 5% Pt-Ti_4O_7.

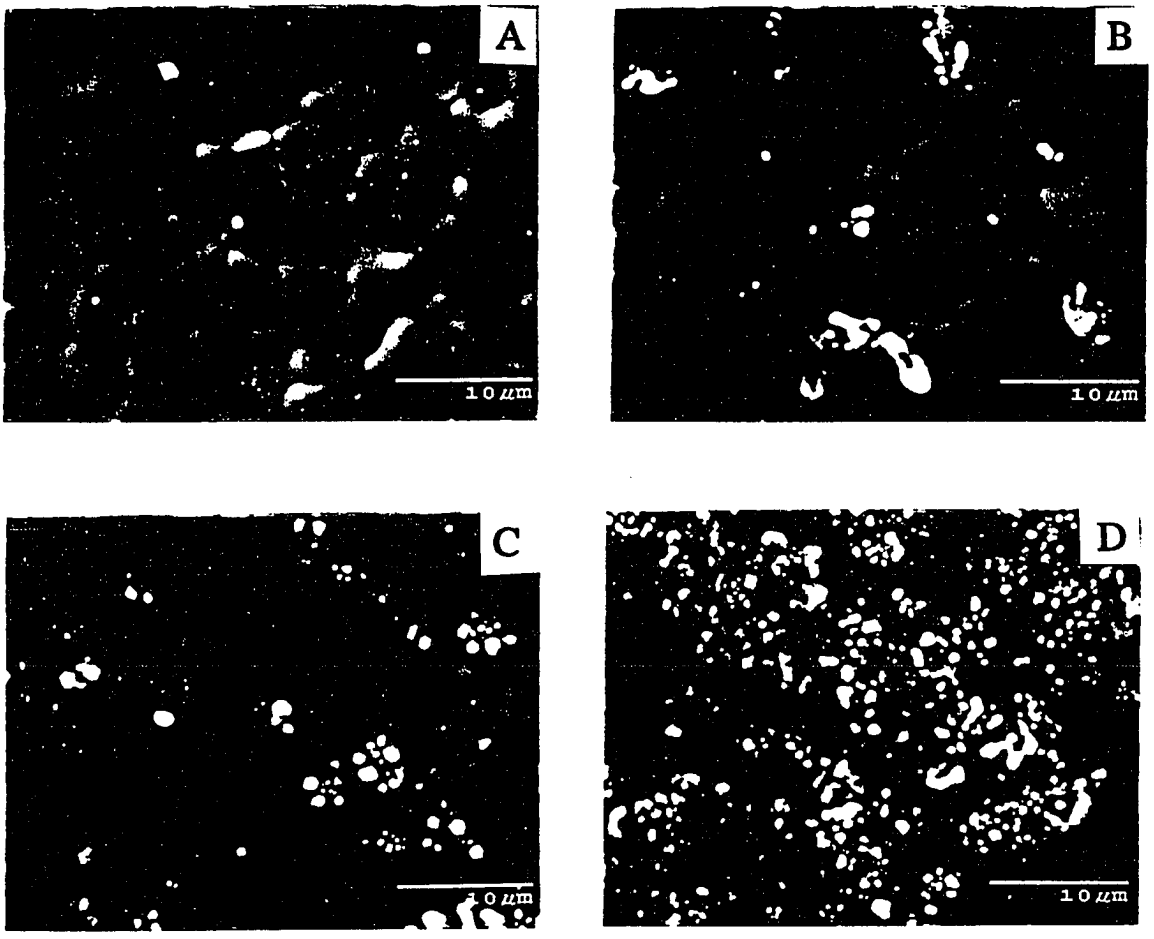

Figure 2. Micrographs of Pt-Ti_4O_7 electrode surfaces. (A) 0.1% Pt-Ti_4O_7, (B) 0.5% Pt-Ti_4O_7, (C) 1% Pt-Ti_4O_7, (D) 5% Pt-Ti_4O_7.

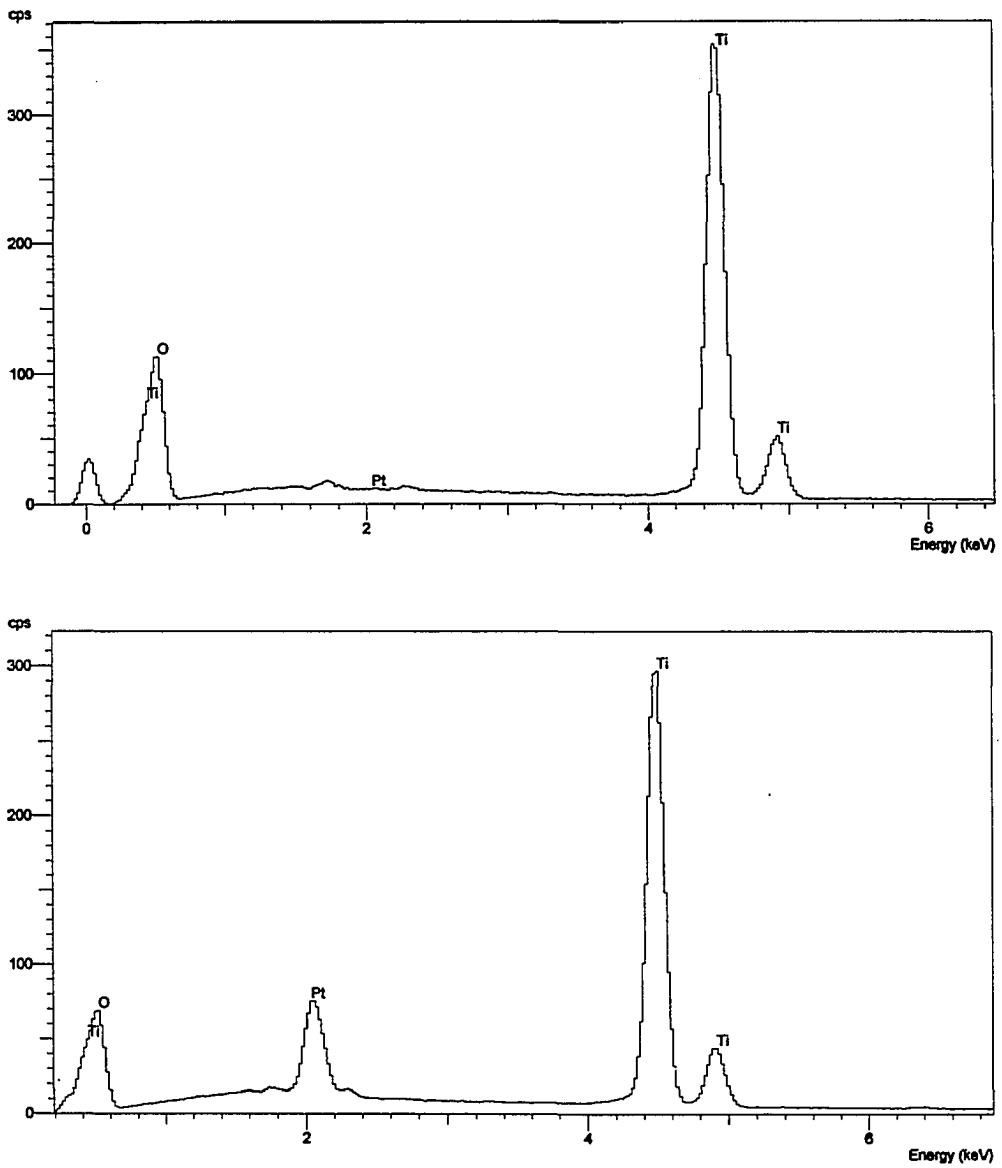

Figure 3. EDS spectra for regions with (A) and without (B) bright spots.

0.1% Pt-Ti_4O_7 . The actual percentages of active area of these Pt-Ti_4O_7 RDEs were calculated based on their x-ray mapping of Pt and they are in good agreement to the experimental values. Platinum particles are very stable in the Ti_4O_7 matrix even when rubbed by tissues (Kimberly-Clark) or polishing cloth (Buehler). The planar surfaces of 0.1% Pt-Ti_4O_7 and 1% Pt-Ti_4O_7 electrodes were polished by silicon carbide discs (LECO) with grit of 600-c, 800-c and 1200-c, respectively, followed by examination using SEM. The typical micrographs 0.1% Pt-Ti_4O_7 and 1% Pt-Ti_4O_7 are similar to those in Figure. 2A&C. The percentages of active areas of these polished 0.1% Pt-Ti_4O_7 and 1% Pt-Ti_4O_7 RDEs were also calculated based on their x-ray mapping of Pt and these values are very close to the expected values (0.1% and 1%). The existence of porosity is evident for all samples. The average diameter for the Pt particles was estimated to be *ca.* 0.1 - 1 μm from SEM-EDS data, which is in acceptable agreement with estimates from XRD data. It is apparent that the distances between nearest Pt particles are randomly distributed and really depend on the electrode itself. It is difficult to make and test adequately the uniformity of these Pt-Ti_4O_7 RDEs surfaces. It is also evident that significant overlap exists between adjacent diffusion zones at these electrode surfaces when the percentage of Pt content is great than 0.5%. Distances between Pt particles in 0.1% Pt-Ti_4O_7 are greater than 8 μm.

Voltammetric results.— Iodide was chosen as a model reactant for the voltammetric characterization of these electrode materials because two major anodic reactions have been reported for iodide at noble metals electrodes in acidic media. The first

reaction is the oxidation of I^- to I_2 (1 eq mol^{-1}) by a quasi-reversible process with $E_{1/2}$ = *ca.* 0.5 V at Ru, Pt, Au, Ir, and glassy carbon (GC) electrodes.[17,18] The second reaction is the oxidation of I^- to IO_3^- (6 eq mol^{-1}) by an irreversible process that requires the concomitant anodic discharge of H_2O. [17] Hence, the anodic wave for production of IO_3^- occurs with a variable $E_{1/2}$ that is dependent on the overpotential for anodic discharge of H_2O at the electrode under consideration [17]. Hydrogen peroxide also was chosen as a reactant because both anodic and cathodic reactions are available at platinum electrode with well defined plateaus.[29] The anodic reaction is the oxidation of H_2O_2 to O_2, and the cathodic reaction corresponds to the reduction of H_2O_2 to H_2O.

1. **Residual Voltammetric responses of electrodes**

Figure 4 shows the residual current-potential (i-E) curves obtained for a Ti_4O_7 rotated disk electrode (RDE; 0.64cm^2) (curve a) in the potential range of -0.35 V to 2.8 V and for the 1% Pt-Ti_4O_7 RDE (0.64cm^2) (curve b) in the potential range of -0.35 V to 1.6 V in 0.1 M H_2SO_4. The residual response for the Pt-Ti_4O_7 RDE is significantly different from that for the Ti_4O_7 RDE. Most obvious is the large difference in the potential for onset of solvent breakdown observed for this current sensitivity, i.e., ca. 1.5 V for the Pt-Ti_4O_7 RDE compared with ca. 2.5 V for the Ti_4O_7 RDE . For the Ti_4O_7 RDE , the current observed during the positive and negative scan in the range E_d = -0.35 to 2.4 V resulted from double-layer charging. For the Pt-Ti_4O_7 RDE , at E_d = 0.4 to 1.4 V on the positive scan, surface oxide was formed. During the subsequent negative scan, reduction of the surface oxide and the reduction of dissolved O_2 produced the large cathodic peak in

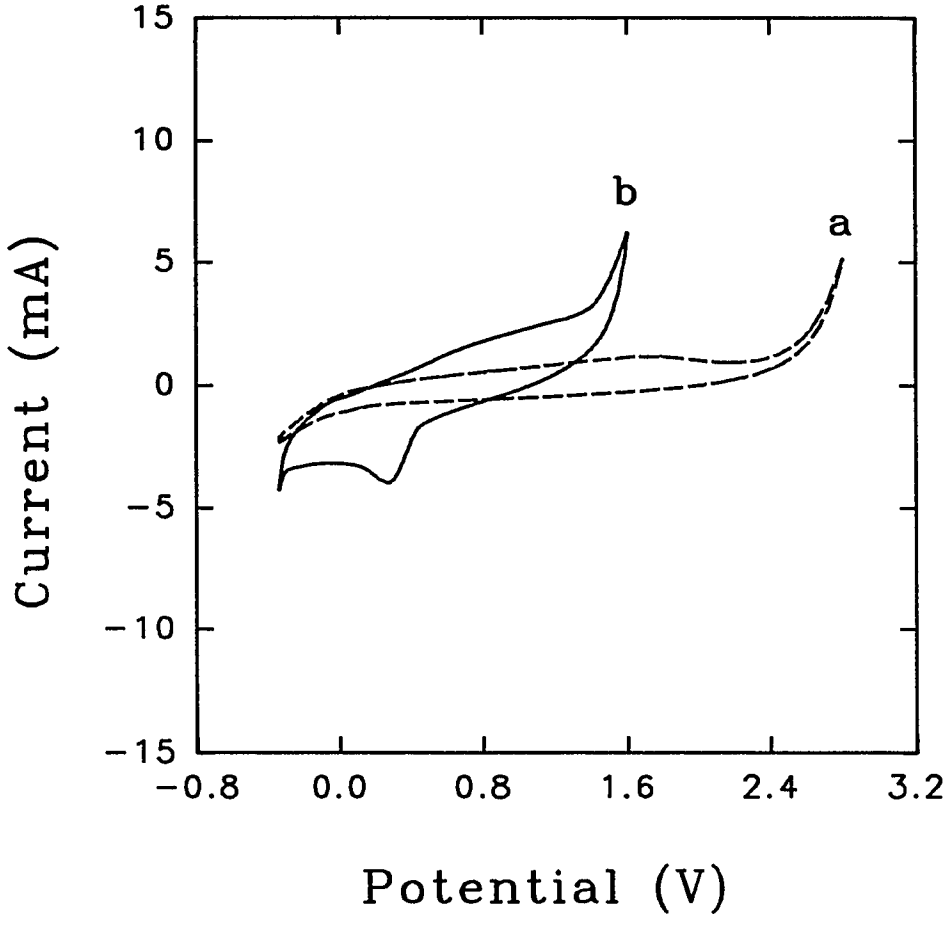

Figure 4. Voltammetric residual current response at Ti_4O_7 (curve a) and 1% Pt-Ti_4O_7 (curve b) rotated disk electrodes in 0.1M H_2SO_4. Scan rate: 30 mV s^{-1}. Rotational velocity: 41.9 rad s^{-1}. A_{geom}: 0.741 cm^2.

the region E_d = 0.5 to -0.3 V with a peak potential (E_p) of ca. 0.2V. To confirm the conclusion that the cathodic peak resulted by the combination of the reduction of surface oxide and the reduction of dissolved O_2 (ca. 0.2 mM in air-saturated in 0.1M H_2SO_4[27]), the following experiments were performed. The first experiment was performed to examine how the cathodic peak depends on the rotation velocity (5.12 to 418.9 rad s^{-1}). The second experiment was to check whether the cathodic peak is a function of scan rate (10 to 90 mV s^{-1}). According to the experimental results, the peak height does depend on the rotation speeds and scan rates but the second fact is dominant. The peak currents are nearly proportional to the potential scan rate while the voltammogram does not change on cycling between the potential range. These characteristics suggest a surface redox process.[28] It is concluded that the effect of surface oxide reduction is larger than that of O_2 reduction for Pt-Ti_4O_7 RDE and the cathodic peak at E ca. 0.2V is contributed dominantly by surface oxide reduction. Cathodic evolution of H_2 occurs at E_d < -0.3 V. On both Ti_4O_7 RDE and Pt-Ti_4O_7 RDE, the large charging currents were observed because rather rough surfaces were evident based on the results of SEM.

2. Current responses for iodide

The difference voltammograms (Δi-E) were generated by subtraction of the i-E responses obtained in the presence and absence of the reactant. Difference voltammetry is anticipated to discriminate against residual currents resulting from double-layer charging, formation and dissolution of surface oxides, and anodic and cathodic evolution of O_2 and H_2, respectively.[26]

The difference voltammetric data are shown in Figure 5 for 2.0mM I^- at solid Pt RDE (A) and 4% Pt-Ti_4O_7 RDE (B) in 0.1M H_2SO_4 . It is apparent from Δi-E curves in Figure 5A that two anodic waves are visible during the positive scans for solid Pt RDE, which are concluded to correspond to the oxidation of I^- to I_2 ($E_{1/2}$ = ca. 0.45 V) and I^- to IO_3^- ($E_{1/2}$ = ca. 1.05 V). Similar results were observed for Pt-Ti_4O_7 REDs as shown in Figure 5B. There is a cathodic peak during the negative scan at E_p = 0.35 V for solid Pt RDE and E_p = 0.28 V for 4% Pt-Ti_4O_7 RDE. These peaks were observed only if the concentration of I^- is greater than a certain value, i.e., > 1.0 mM for Pt RDE and > 1.5 mM for 4% Pt-Ti_4O_7 RDE, and were shifted to more negative potential value as the concentration of reactant increased. The peak heights were a function of the concentrations of I^-, increasing with increasing concentration of I^-. These peaks are attributed to the cathodic stripping of absorbed of I_2 from Pt surface and reduction of I_2 trapped within surface pores at metal sites inside the pores.

To determine whether the cathodic peak was resulted by the reduction of the species produced in the first wave or second wave, the data shown in Figure 6 were obtaineded. Figure 6 shows voltammetry data obtained at 3% Pt-Ti_4O_7 RDE in the range of E_d = 0.0 to 0.85 V in 0.1M H_2SO_4 containing various concentrations of I^- (mM): (a) 0.0, (b) 1.0, (c) 2.0 and (d) 2.5. In this potential range, only the oxidation of I^- to I_2 occurred during the positive scan. The cathodic peak at E_p = 0.35 V resulted from the stripping of I_2 on the surface and the reduction of I_2 . The cathodic peak height in Figure 6 is smaller than that in Figure 5B even at same concentration of I^- (2.0 mM). It is indicative that the cathodic

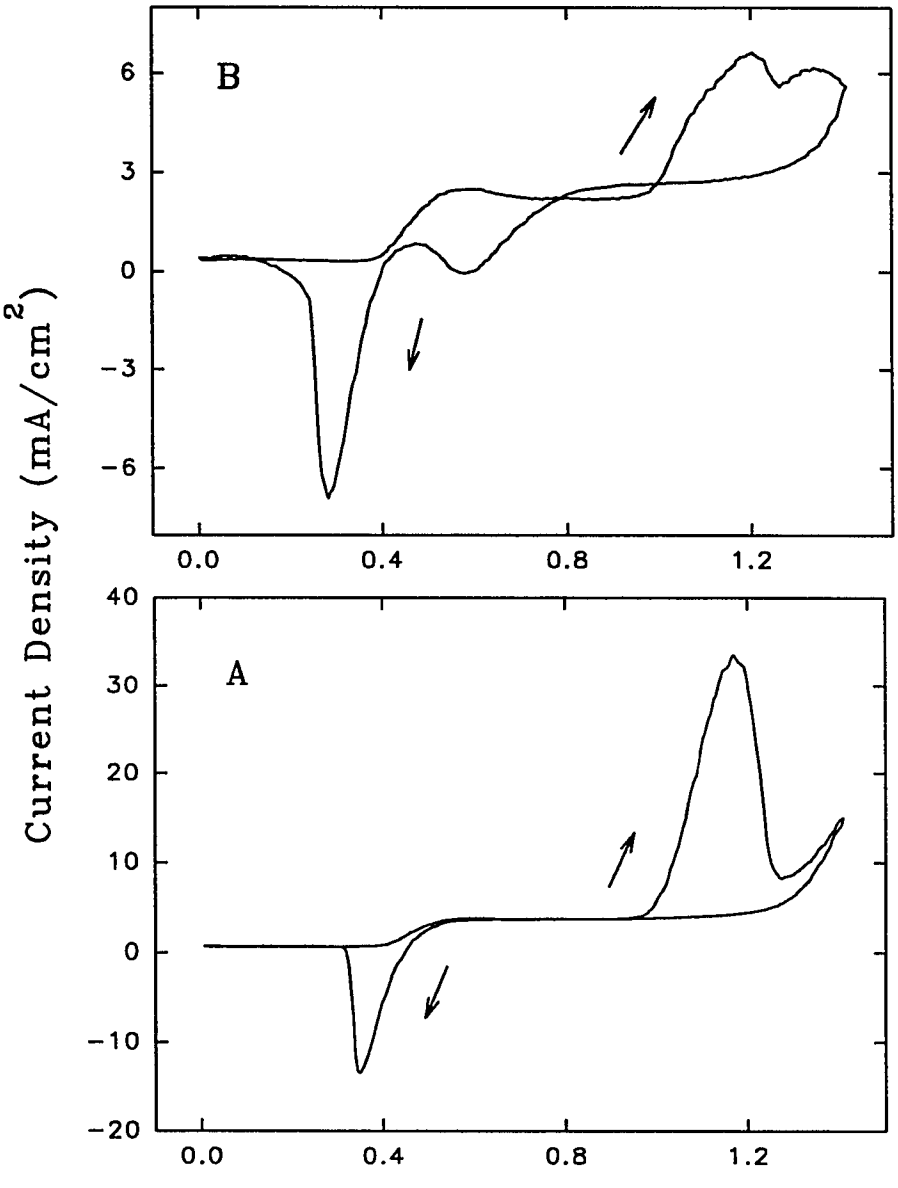

Figure 5. Difference voltammetric response for I^- at Pt (A) and 4% Pt-Ti_4O_7 (B) rotated disk electrodes. Scan rate: 30 mV s^{-1}. Rotational velocity: 41.9 rad s^{-1}. Concentration of I^- (mM): **(a,c)** 0, **(b,d)** 2.0.

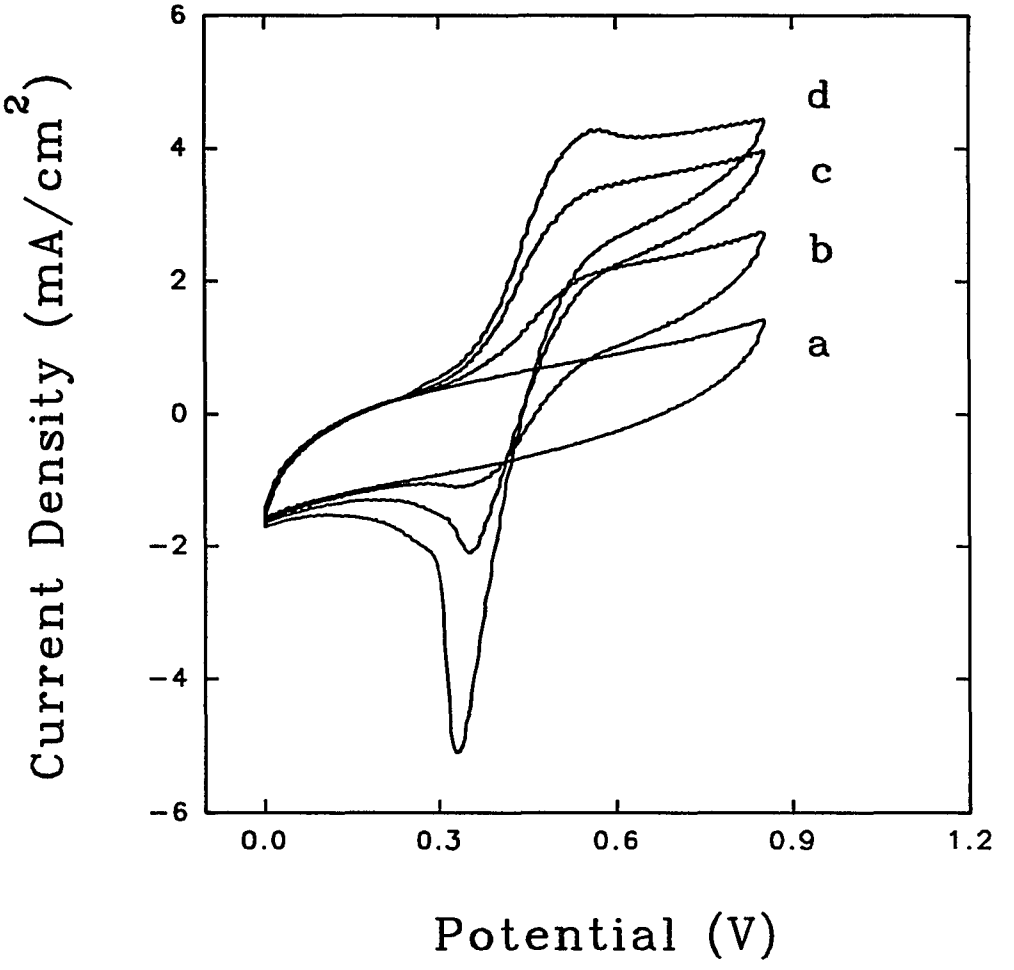

Figure 6. Voltammetric response at the 3% Pt-Ti_4O_7 RDE in the potential range of 0 to 0.85 V containing various I^- concentration. Rotational velocity: 41.9 rad s^{-1}. Scan rate: 30 mV s^{-1}. Concentration of I^- (mM): (a) 0, (b) 1.0, (c) 2.0, (d) 2.5.

peak in Figure 5B was contributed by the stripping of I_2 absorbed on the surface and the reduction of I_2 trapped in the pores. Trapped I_2 can originate from the oxidation of I^- to I_2 and homogenous reaction of I^- with IO_3^-.

3. **Current responses for hydrogen peroxide**

Figure 7 shows voltammetric data of Ti_4O_7 RDE without (curve a) and with (curve b) hydrogen peroxide (5mM) in the potential range of -0.35 V to 1.5 V in 0.1M H_2SO_4. It is evident that the Ti_4O_7 RDE is electrochemically inert towards hydrogen peroxide in this particular potential range and can be used as a matrix for a microelectrode array for this reaction. It is also reported by Baez [28] that Ti_4O_7 RDE can be used as a catalyst for the reduction of hydrogen peroxide only when the potential is more negative than -0.8 V.

Figure 8 presents the voltammograms for the solid Pt RDE (A) and the 1%Pt-Ti_4O_7 RDE (B) in the potential range of -0.35 V to 1.5 V in 0.1M H_2SO_4, in which the curves a and c correspond to the residual curves and curves b and d are the current corresponding to the 3mM H_2O_2. The large magnitude of the charging current in curve c, compared with curve a, indicates that the Pt-Ti_4O_7 RDE has a much greater porosity with a larger surface area exposed to the aqueous solution. This is consistent with the conclusion based on SEM data in Figure 2A-D. Anodic waves are visible during the positive scans in Figure 8A&B that are concluded to correspond to the oxidation of H_2O_2 to O_2 at $E_{1/2}$ = ca. 0.60 V for solid Pt RDE(A) and ca. 0.78 V for 1%Pt-Ti_4O_7 RDE (B). During the negative scan the cathodic waves corresponding to the reduction of H_2O_2 to H_2O are observed at $E_{1/2}$ = ca. 0.4 V for solid Pt RDE(A) and ca. 0.35 V for 1%Pt-Ti_4O_7 RDE (B) and the waves have

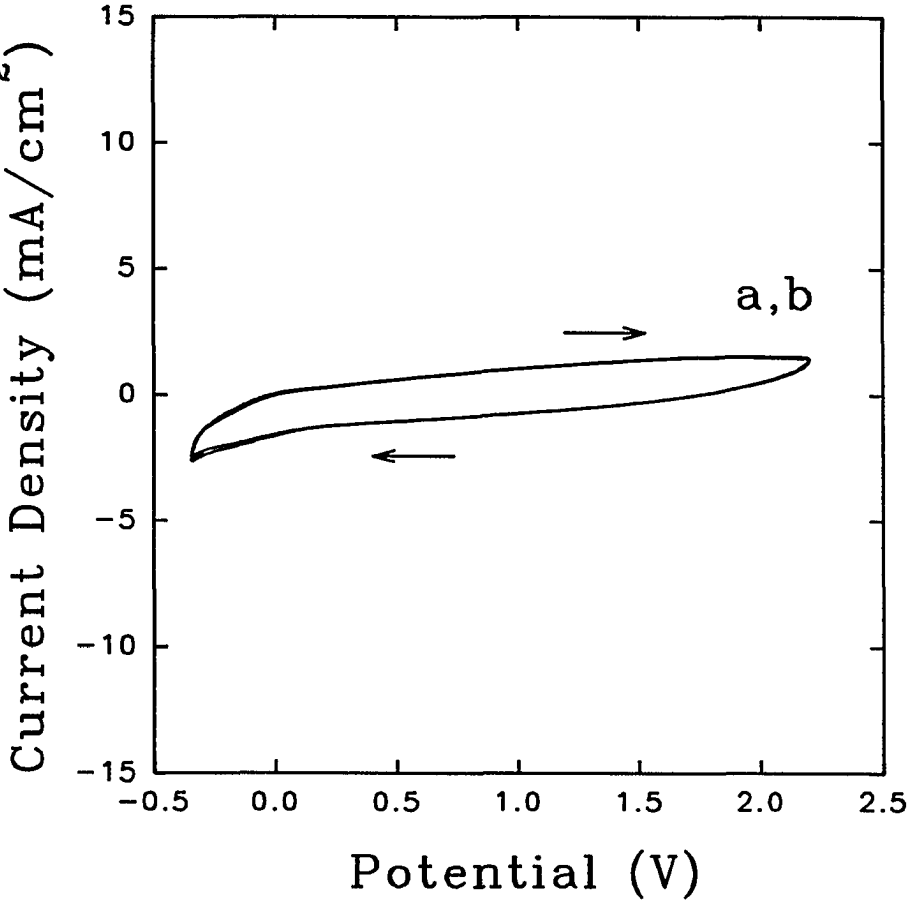

Figure 7. Voltammetric data of Ti_4O_7 RDE without (curve a) and with (curve b) hydrogen peroxide (5mM) at the potential range of -0.35 V to 1.5 V in 0.1M H_2SO_4. Scan rate: 30 mV s^{-1}. Rotational velocity: 41.9 rad s^{-1}. A_{geom}: 0.741 cm^2.

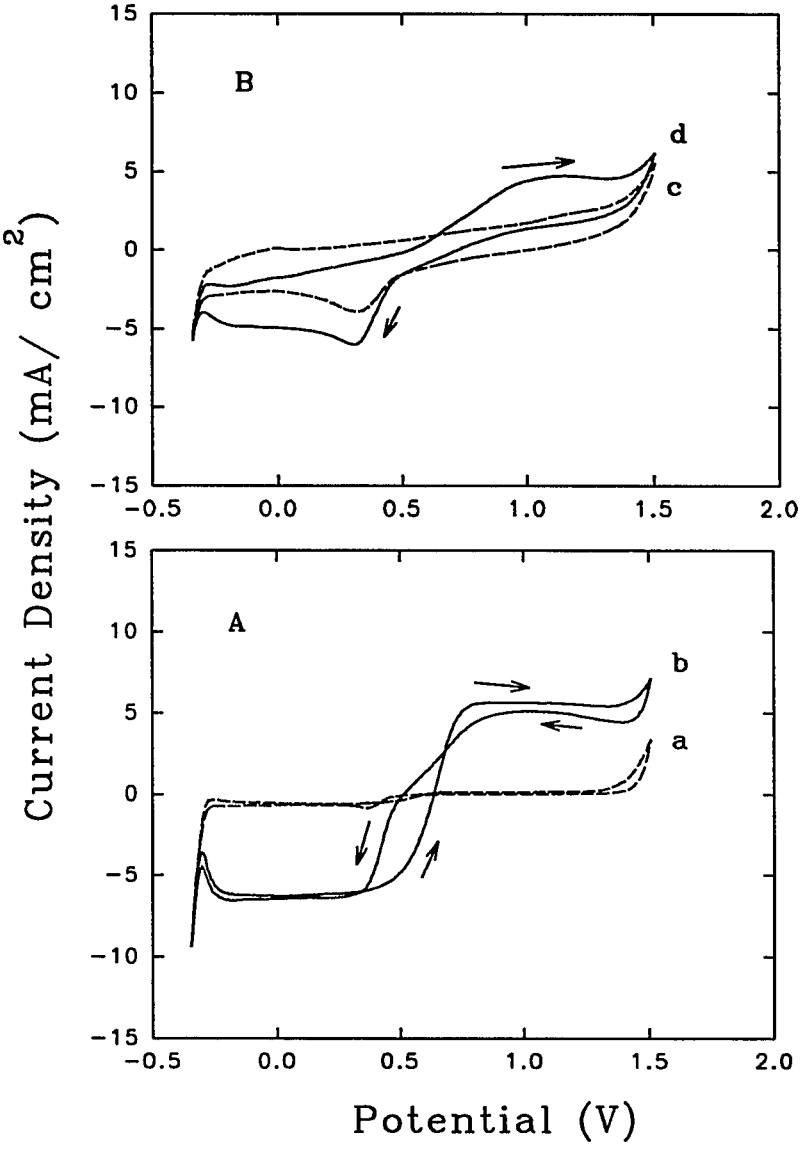

Figure 8. Voltammetric response for H_2O_2 at Pt (A) and 1% Pt-Ti_4O_7 (B) rotated disk electrodes. Scan rate: 30 mV s^{-1}. Rotational velocity: 41.9 rad s^{-1}. Concentration of H_2O_2 (mM): **(a,c)** 0, **(b,d)** 3.0.

well-defined limiting current plateaux.

Determination of current density

The amperometric response of microelectrode arrays can be characterized by the relative current density (*J*) defined as the true current density at the collective microelectrodes of the array normalized with respect to the current density at a solid electrode of large geometry:

$$J = \frac{(i/A_{act})_{array}}{(i/A_{geom})_{solid}} \qquad [3]$$

In effect, according to Equation 3, the ratio of signal-to-background current densities (*S/B*) are enhanced by the factor *J* at array electrodes, in comparison to solid electrodes, when the background current is proportional to the total area of the active region(s) of the electrodes.

The amperometric response at microelectrode arrays also has been characterized by a so-called "attenuation factor" (ρ) defined as the apparent current density at the array normalized with respect to the current density for a solid electrode of large geometry:

$$\rho = \frac{(i/A_{geom})_{array}}{(i/A_{geom})_{solid}} \qquad [4]$$

Hence, from Equations 3 and 4, values of *J* and ρ are related according to:

$$\rho = J(1 - \theta) \qquad [5]$$

where θ has been called a "blocking factor" [1,5,6] by analogy with partially fouled electrode surfaces, and the quantity $\rho/J = 1 - \theta$ is the ratio of the active and geometric areas

(A_{act}/A_{geom}).

The effect of change in rotational velocity (ω) for disk electrodes constructed from microelectrode arrays can be predicted easily for two limiting conditions. For low density arrays ($\theta \rightarrow 1$) with active sites that behave as isolated and ideal microelectrodes, current is expected to be independent of ω. However, because the transport-limited current at a solid RDE is proportional to $\omega^{1/2}$, [7] J and ρ are expected to be proportional to $\omega^{-1/2}$ for these ideal microelectrode arrays. For high density arrays ($\theta \rightarrow 0$), the diffusion zones of adjacent active sites overlap extensively and, in the limit of total overlap of diffusion zones, the corresponding array electrodes have a virtually uniform diffusion-layer thickness across the face of the electrode and the current is proportional to $\omega^{1/2}$. Hence, for these high density array electrodes, J and ρ are expected to be independent of changes in ω. These conclusions are consistent with predictions based on models which neglect the effect of radial mass transport. [1,6,8] For microelectrode arrays of intermediate density ($0 \ll \theta \ll 1$), J and ρ are expected to be complex functions of ω.

Iodide.--- Figure 9 and Figure 10 contain plots of i/A_{geom} vs. $\omega^{1/2}$ corresponding to the oxidation of I^- to I_2 (0.7 v) and I^- to IO_3^- (1.20V) for the solid Pt RDE and various Pt-Ti_4O_7 RDEs. Curves (a), (b) , (c), (d) and (e) are current responses in Levich plots for Pt, 0.1% Pt-Ti_4O_7, 0.5% Pt-Ti_4O_7, 1% Pt-Ti_4O_7 and 5% Pt-Ti_4O_7 RDEs, respectively. Curve (a) for Pt RDE is virtually linear with a near-zero intercept, as expected for transport-limited reactions at a solid RDE (i.e., $A_{act} \approx A_{geom}$). Current density (i/A_{geom}) of 0.1% Pt-Ti_4O_7 RDE is less dependent on $\omega^{1/2}$ as compared with the other Pt-Ti_4O_7 RDEs,

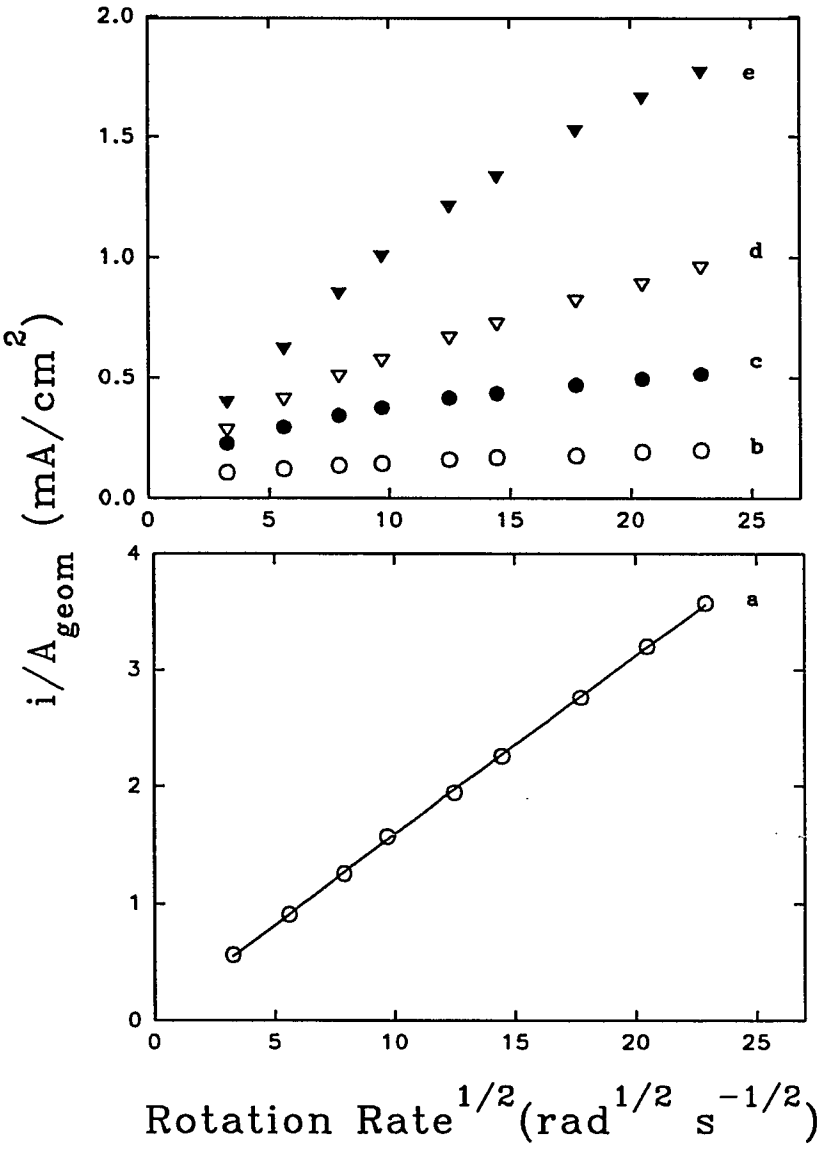

Figure 9. Plots of apparent current density *vs.* square root of rotational velocity for various rotated disk electrodes for oxidation of I^- to I_2 at 0.70 V. Concentration of I^-: 0.5 mM. Electrodes: (a) Pt, (b) 0.1% Pt-Ti_4O_7, (c) 0.5% Pt-Ti_4O_7, (d) 1% Pt-Ti_4O_7, (e) 5% Pt-Ti_4O_7.

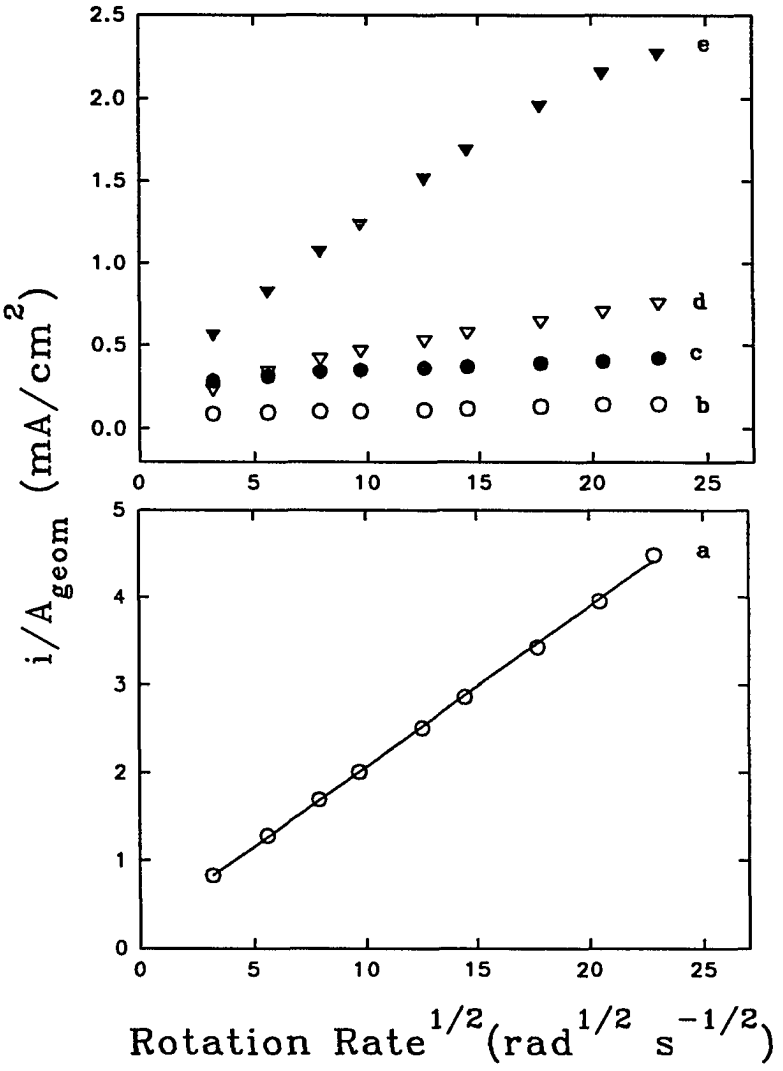

Figure 10. Plots of apparent current density *vs.* square root of rotational velocity for various rotated disk electrodes based on oxidation of I^- to IO_3^- at 1.20 V. Concentration of I^-: 0.5 mM. Electrodes: (a) Pt, (b) 0.1% Pt-Ti_4O_7, (c) 0.5% Pt-Ti_4O_7, (d) 1% Pt-Ti_4O_7, (e) 5% Pt-Ti_4O_7.

which is an indication that the behavior of 0.1% Pt-Ti_4O_7 RDE is closer to an ideal microelectrode array as compared with other Pt-Ti_4O_7 RDEs. The current responses for the other Pt-Ti_4O_7 RDEs (0.5% Pt-Ti_4O_7 to 5% Pt-Ti_4O_7) are more complex and indicate some overlap of the diffusional zones for adjacent microelectrodes in these RDEs, especially at low ω values.

Values of the relative current density (J, see Eqn. 3) are plotted vs. $\log(A_{act}/A_{geom})$ in Figure 11 and Figure 12 for the oxidation of I^- to I_2 (0.7 v) and I^- to IO_3^- (1.20V), respectively, at various Pt-Ti_4O_7 RDEs for various values of ω (10.5 to 523 rad s^{-1}). The theoretical value J=1 can be used as a reference point for $A_{act}/A_{geom} = 1$, corresponding to a transport-limited reaction at solid Pt RDE. As expected, J values are larger for smaller ω value, i.e., curve (f) corresponding to $\omega = 10.5$ rad s^{-1}. The enhancement factors for oxidation of I^- to I_2 and I^- to IO_3^- increase with the fractional active area decreasing. The relative current densities are measured as high as 180 and 108 for the oxidation of I^- to I_2 (0.7 v) and I^- to IO_3^- (1.20V), respectively, at $\omega = 10.5$ rad s^{-1}.

Hydrogen peroxide.--- Figure 13 show current responses (i/A_{geom}) as a function of $\omega^{1/2}$ for the solid Pt RDE (curve a) and for various Pt-Ti_4O_7 RDEs (curve b-e) at E = 1.10V for the oxidation of H_2O_2 to O_2. The mass-transport limited current at a uniformly accessible RDE ($\theta = 0$) is expected to be a linear function of $\omega^{1/2}$. Deviations from linearity in i - $\omega^{1/2}$ plots are observed when the current is under mixed mass-transport and kinetic control. Data of this type are usually plotted as i^{-1} vs.$\omega^{-1/2}$ according to the Koutecky-Levich equation (Eqn.2). Figure 14 shows the A_{geom}/ i^{-1} vs. $\omega^{-1/2}$ plots for solid Pt RDE (curve a),

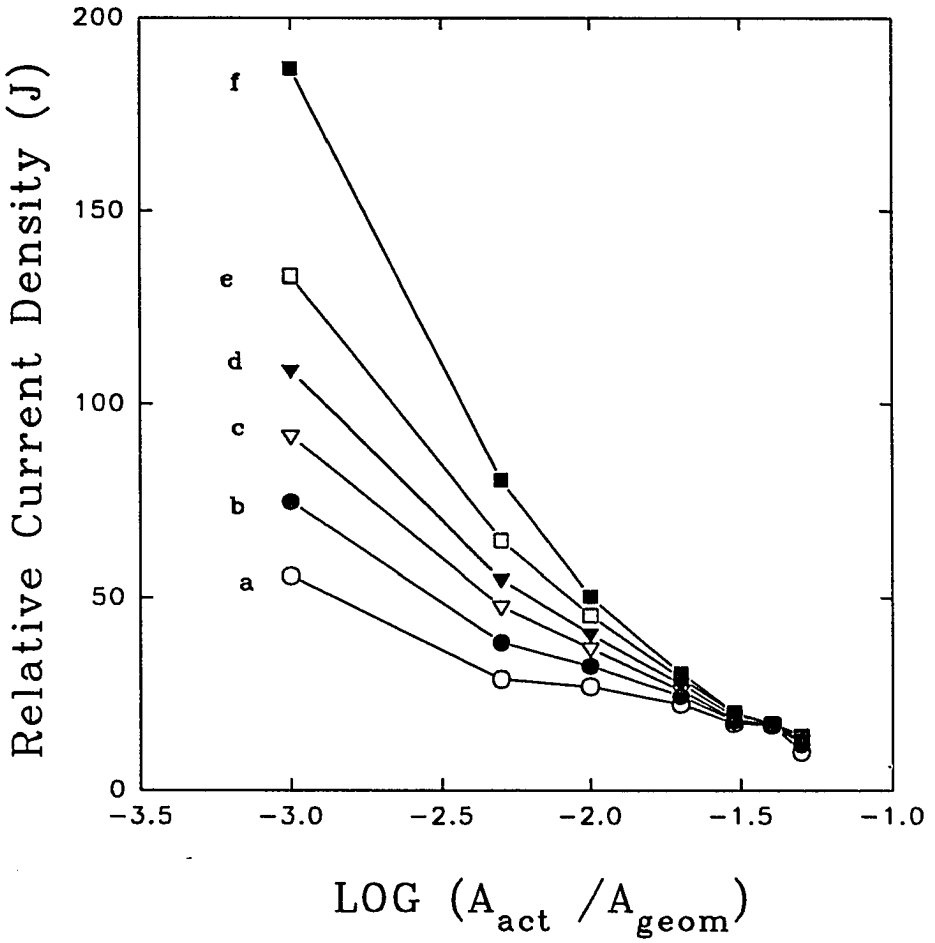

Figure 11. Relative current density (J) as a function of fractional active area (A_{act}/A_{geom} = 1 - θ) at Pt-Ti_4O_7 rotated disk electrodes for oxidation of I^- to I_2 at 0.70 V. Concentration of I^-: 0.5 mM. Rotational velocity (rad s^{-1}): (a) 512, (b) 209, (c) 94.2, (d) 62.8, (e) 31.4, (f) 10.5.

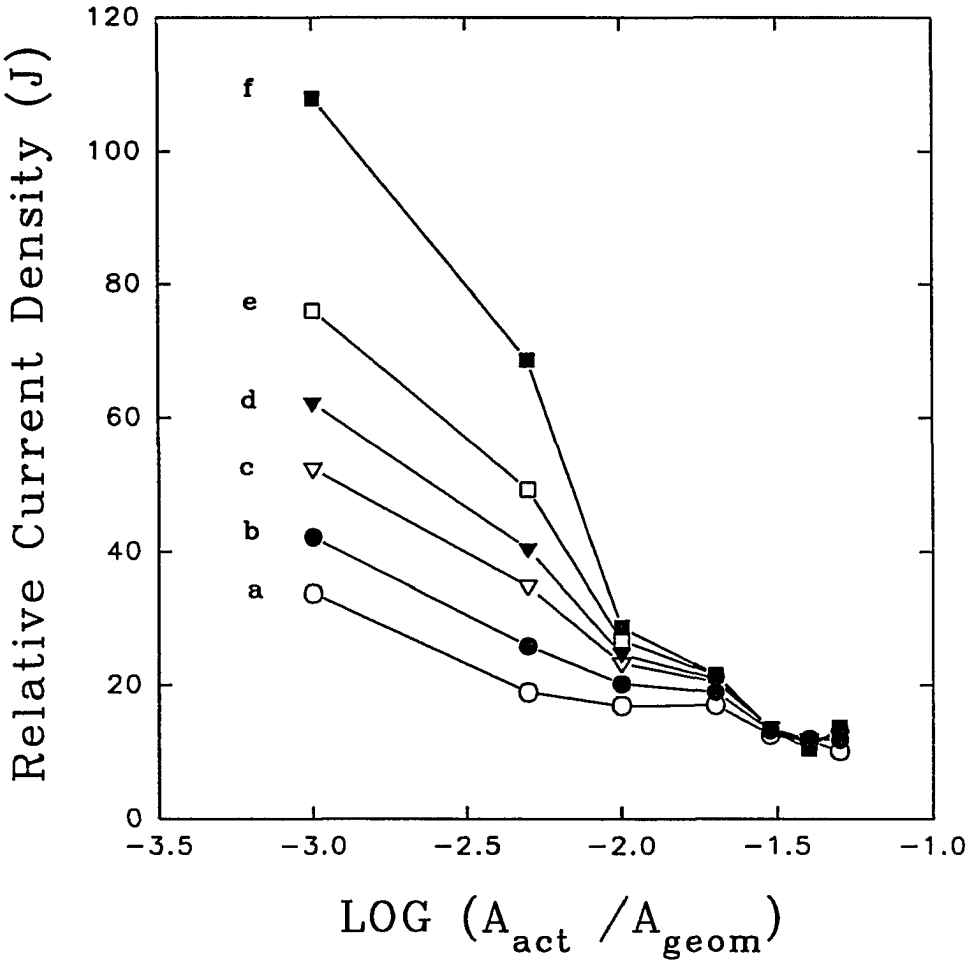

Figure 12. Relative current density (J) as a function of fractional active area (A_{act}/A_{geom} = 1 - θ) at Pt-Ti_4O_7 rotated disk electrodes for oxidation of I^- to IO_3^- at 1.20 V. Concentration of I^-: 0.5 mM. Rotational velocity (rad s^{-1}): (a) 512, (b) 209, (c) 94.2, (d) 62.8, (e) 31.4, (f) 10.5.

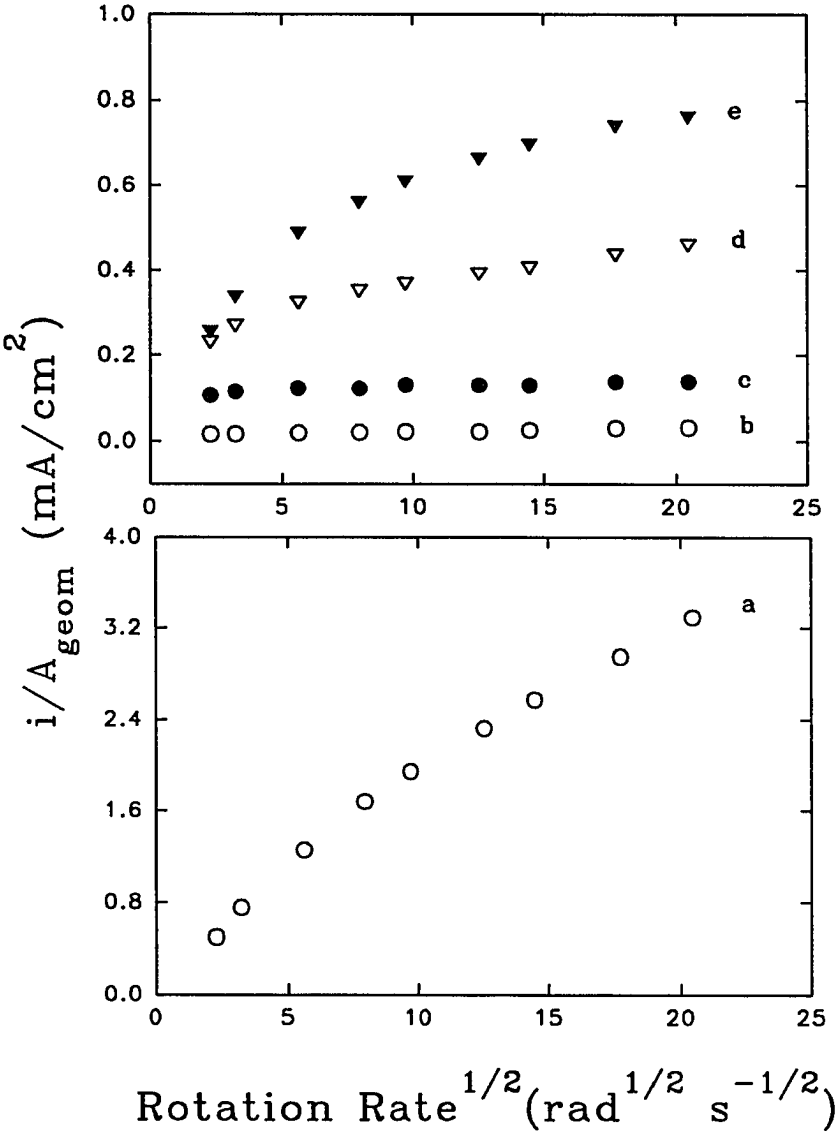

Figure 13. Plots of apparent current density *vs.* square root of rotational velocity for various RDEs for oxidation of H_2O_2 to O_2 at 1.10 V. Concentration of H_2O_2: 0.5 mM. Electrodes: (a) Pt, (b) 0.1% Pt-Ti_4O_7, (c) 0.5% Pt-Ti_4O_7, (d) 1% Pt-Ti_4O_7, (e) 5% Pt-Ti_4O_7.

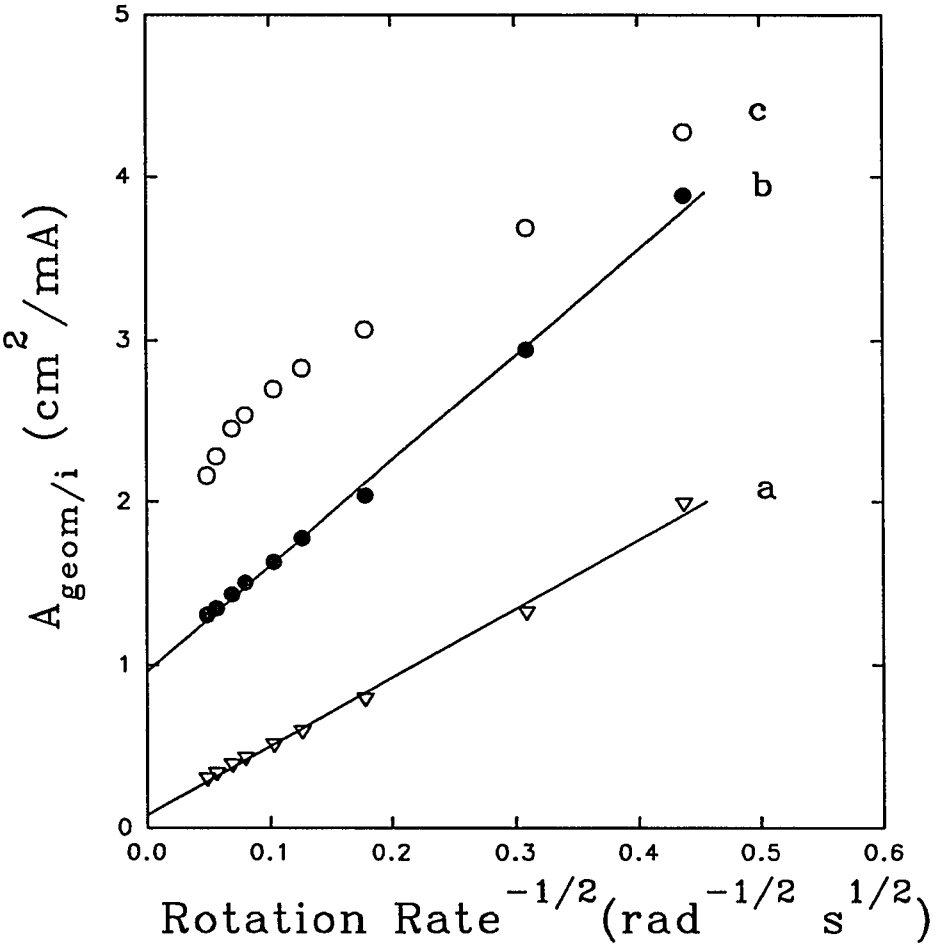

Figure 14. Plots of inverse of apparent current density *vs.* inverse of square root of rotational velocity for various RDEs for oxidation of H_2O_2 to O_2 at 1.10 V. Concentration of H_2O_2: 0.5 mM. Electrodes: (a) Pt, (b) 5% Pt-Ti_4O_7, (c) 1% Pt-Ti_4O_7.

5% (curve b) and 1% (curve c) Pt-Ti_4O_7 RDEs. All current values have been normalized by the geometric areas of the electrodes to allow comparison between electrodes in the same figure. Curve a in Figure 14 is a near-zero intercept linear line with regression coefficient 0.998, which indicates that the kinetics on the surface of solid Pt RDE for the oxidation of hydrogen peroxide is fast and it is nearly mass transport controlled. Curve b is a linear line with regression coefficient 0.998 and non-zero intercept which indicates that it is a mixed mass-transport and kinetic controlled. The situation for the Pt content less than 1% is similar to the curve c in which the curvature of Koutecky-Levich plot is evident. Curvature observed in plots of i vs. $\omega^{1/2}$ and i^{-1} vs. $\omega^{-1/2}$ at partially blocked rotating disk electrodes has been rationalized previously on the basis of significant overlap of adjacent diffusion zones when the distance between adjacent active regions is comparable to the diffusion-layer thickness at the electrode surface. [5,6,8,19-22] Here similar arguments are given to explain the curvature in this work.

Values of the relative current density (J, see Eqn. 3) are plotted vs. $\log(A_{act}/A_{geom})$ in Figure 15 for the oxidation of hydrogen peroxide (1.10V) at various Pt-Ti_4O_7 RDEs for various values of ω (rad s^{-1}): a=5.2, b=10.5, c=31.4, d=62.8, e=157 and f=418.7. The theoretical value J=1 for $A_{act}/A_{geom} = 1$, corresponding to a reaction at solid Pt RDE, is reported as a reference point. As expected, J values are larger for smaller ω values, i.e., curve (a) corresponding to $\omega = 5.2$ rad s^{-1}. The largest enhancement factor for oxidation of hydrogen peroxide (J=48) is apparent for the 1% Pt-Ti_4O_7 RDE. Even though it is expected that J decreases with increased rotating rate ω, the 1% Pt-Ti_4O_7 RDE still exhibits

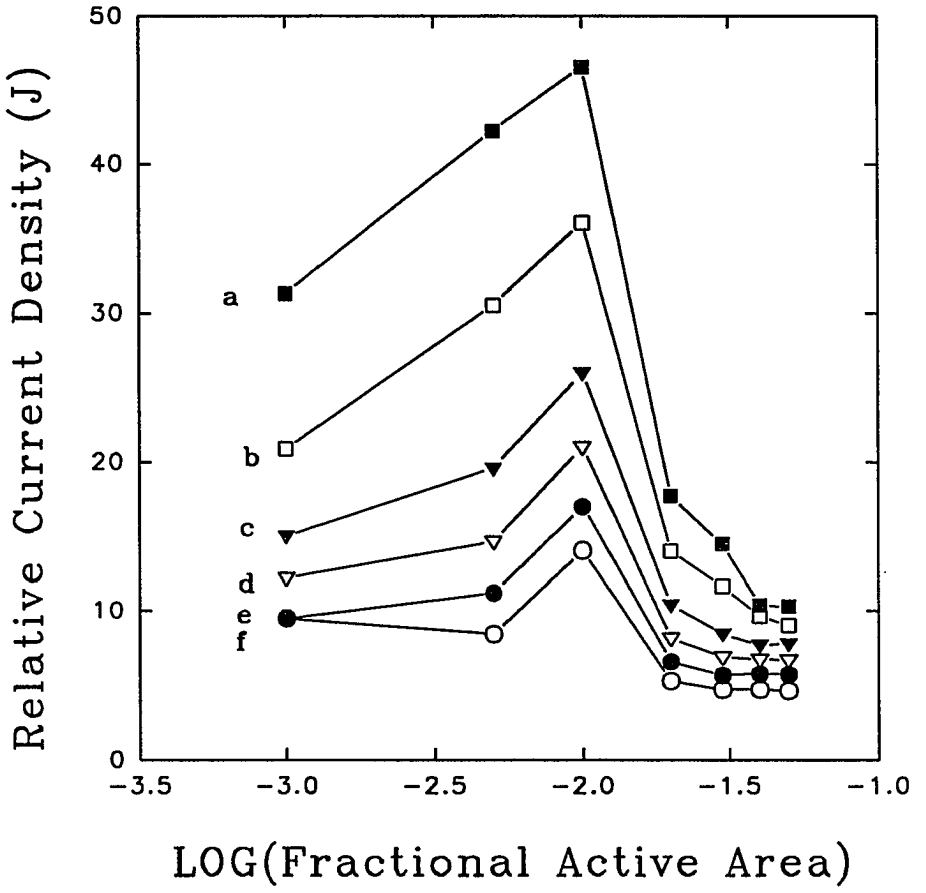

Figure 15. Relative current density (J) as a function of fractional active area (A_{act}/A_{geom} = 1 - θ) at Pt-Ti_4O_7 RDEs for oxidation of H_2O_2 to O_2 at 1.10 V. Concentration of H_2O_2: 0.5 mM. Rotational velocity (rad s^{-1}): (a) 5.2, (b) 10.5, (c) 31.4, (d) 62.8, (e) 157, (f) 418.9.

significantly larger J values than the solid Pt RDE at the highest velocity tested (418.7 rad s^{-1}, curve f in Figure 15), i.e., J=14 for the production of O_2.

As compared Figure 15 (H_2O_2 to O_2) with Figure 11 (I^- to I_2) and Figure 12 (I^- to IO_3^-), the optimal fractional active area for the oxidation of H_2O_2 to O_2 is 1% Pt in Ti_4O_7. For the oxidation of I^- to I_2 and IO_3^-, the smaller the fractional active area, the larger is the enhancement in current density. This is indicative of the fact that even for the same electrode materials the enhancement in current density and the optimal fractional active area really depend on the characteristics of electrochemical reactions themselves.

Conclusions

Platinum microarray electrodes were fabricated successfully using Ti_4O_7 as a binder. The Pt-Ti_4O_7 rotating disc electrodes (RDEs) function similarly as solid Pt RDE for the oxidation of I^-, and redox of H_2O_2 in acidic media.

The large current density enhancement factors were observed as high as 180, 120 and 40 times for oxidation of I^- to I_2, I^- to IO_3^- and H_2O_2 to O_2, respectively. The enhancement factors increase with the fractional active area decreasing for oxidation of I^- to I_2 and I^- to IO_3^-. The enhancement factor for the oxidation of H_2O_2 to O_2 was achieved at the optimal fractional active area close to 1%. This fact indicate that even for the same electrode materials the enhancement in current density and optimal fractional active area really depend on the characteristics of electrochemical reactions themselves.

Curvature observed in plots of i *vs.* $\omega^{1/2}$ and i^{-1} *vs.* $\omega^{-1/2}$ for transport-limited faradaic

reactions at partially blocked rotated disk electrodes has been rationalized on the basis of significant overlap of adjacent diffusion zones when the distance between adjacent active regions is comparable to the diffusion-layer thickness at the electrode surface. [5,6,8,19-22] Here, we rely on similar arguments to explain curvature in our plots.

The observation that 0.1% Pt-Ti_4O_7 responds in a manner close to an ideal microelectrode array is consistent with the result of a simple comparison of estimated values for the diffusion-layer thickness at the Pt sites and the distance between adjacent Pt sites. The steady-state diffusion layer thickness (δ) at an ideal microdisk electrode is $\pi r/4$, where r is the radius of the microdisk. [23,24] Based on the average diameter of 0.5 μm for Pt sites in Pt-Ti_4O_7 RDEs prepared from initial material and estimated on the basis of the peak widths for the XRD data, we calculate $\delta = 0.2$ μm as a conservative estimate. This value of δ is significantly smaller than the value of 8 μm estimated for the minimum inter-site distance in 0.1% Pt-Ti_4O_7 surfaces using SEM. Hence, from this comparison, it is logical to expect that adjacent diffusion zones have virtually no overlap for this electrode material.

Since all of Pt-Ti_4O_7 RDEs tested exhibited the significant enhancement of current densities as compared with solid Pt RDE, we suggest that these Pt-Ti_4O_7 RDEs may have utility for large-scale applications wherein cost of precious metal electrode materials must be minimized.

Acknowledgement

Ames Laboratory is operated for the U.S. Department of Energy by Iowa State University under Contract No. W-7405-ENG-82. This research was supported by the Director for Energy Research, Office of Basic Energy Sciences.

References

1. O. Contamin and E. J. Levart, *J. Electroanal. Chem.*, **136**, 259 (1982).
2. S. L. Peterson and D. E. Tallman, *Anal. Chem.*, **60**, 82 (1988).
3. D. J. Chesney, J. L. Anderson, D. E. Weissaar and D. E. Tallman, *Anal. Chim. Acta*, **124**, 321 (1981).
4. J. E. Vitt, D. C. Johnson and D. E. Tallman, *Anal. Chem.*, **65**, 231 (1993).
5. F. Schelle, R. Landsberg and H. Wolf, *Electrochim. Acta*, **15**, 525 (1970).
6. E. Levart, *J. Electroanal. Chem.*, **187**, 247 (1985).
7. V. G. Levich, *Physicochemical Hydrodynamics*, Prentice Hall: Englewood Cliffs, NJ, p. 75 (1962).
8. V. Yu. Filinovsky, *Electrochim. Acta*, **25**, 309 (1980).
9. S. G. Weber, *Anal. Chem.*, **61**, 295 (1989).
10. R. L. Clarke, in *Proceedings of the Second International Forum on Electrolysis in the Chemical Industry*, Deerfield Beach, FL (1988).
11. P. C. S. Hayfield and R. L. Clarke, in *Proceedings of the Electrochemical Society Meeting*, Los Angeles, CA (1989).

12. P. C. S. Hayfield, *U.S. Patent* 4,422,917 (1983).

13. N. L. Weinberg, J. D. Genders and R. L. Clarke, *U.S Patent* 4,936,970 (1990).

14. P. Villars and L. D. Calvert, *Pearson's Handbook of Crystallographic Data for Intermetallic Phases*, 2nd ed., ASM International: Materials Park, OH, pp. 4776 & 5097 (1991).

15. Y. Le Page and M. Marezie, *J. Solid State Chem.*, **53**, 13 (1984).

16. A. Guinier, *X-Ray Diffraction*, W.H. Freeman and Co., San Francisco, CA, and London, U.K., p. 121 (1963).

17. J. E. Vitt and D. C. Johnson, *J. Electrochem. Soc.*, **138**, 774 (1992).

18. D.C. Johnson, *J. Electrochem. Soc.*, **119**, 331 (1972).

19. R. Landsberg and R. Thiele, *Electrochim. Acta*, **11**, 1243 (1966).

20. F. Schelle, S. Muller, R. Landsberg and H.-J. Spitzer, *J. Electroanal. Chem.*, **19**, 187 (1968).

21. A. M. Trukhan, Yu. M. Povarov and P. D. Lukovtsev, *Elektrokhim.*, **6**, 425 (1970).

22. Yu. M. Povarov, A. M. Trukhan and P. D. Lukovtsev, *Elektrokhim.*, **6**, 602 (1970).

23. K. B. Oldham, *J. Electroanal. Chem.*, **122**, 1 (1981).

24. K. Aoki and J. G. Osteryoung, *J. Electroanal. Chem.*, **122**, 19 (1981).

25. L. He, H. F. Franzen, J. E. Vitt and D. C. Johnson *J. Electrochem. Soc.*, **141**, 1014 (1994).

26. M. Noel and K.I. Vasu, *Cyclic Voltammetry and the Frontiers of Electrochemistry*, Aspect Publication Ltd. (1990) p.24

27. R. C. Weast, *CRC Handbook of Chemistry and Physics*, CRC press, Inc., Boca Raton, Florida (1990), D115.

28. V. B. Baez, J. E. Graves and D. Pletcher *J. Electroanal. Chem.* , **340**, 273 (1992).

29. V.G. Prabhu, L.R. Zarapkar and R.G. Dhaneshwar *Electrochimica Acta*, **26**, 725 (1981).

GENERAL SUMMARY AND CONCLUSIONS

Research described in this dissertation is part of a large project to synthesize composite electrode materials. Goals of this research include the identification of important composition-structure-reactivity relationships as well as the discovery of new electrode materials that might have applicability in various electrochemical industries, including use as amperometric sensors.

Microelectrode arrays consist of numerous small electrodes within the surface of an electrochemically inert matrix. The inert matrix provides mechanical stability, defines the fluid dynamic properties, and ensures electrical correspondence between the microelectrodes. In some previous research related to microelectrode arrays, graphite particles were incorporated into the matrix to achieve connectivity between the microelectrodes and to achieve the optimal fractional active area. However, there are two disadvantages to using graphite powder. First, when the electrodes are polished, a loss of graphite occurs at the surface, resulting in a loss of electrical connectivity. Second, because graphite is a useful electrode material for faradaic reactions, its use is undesirable in the fabrication of metal microelectrode arrays.

Advantages could be gained if matrices are used that are both electrically conductive and electrochemically inert are used. A ceramic material, Ti_4O_7, is an appropriate candidate because of its high conductivity and stability in corrosive media. A part of research described in this dissertation focuses on the generation of noble metal (e.g., Ru and Pt) microelectrodes within conductive Ti_4O_7 matrices as part of a larger project to

synthesize composite electrode materials using a minimum of precious metals.

Since all of Ru-Ti_4O_7 and Pt-Ti_4O_7 RDEs tested exhibited the significant enhancement of current densities as compared with solid Ru and Pt RDEs, we suggest that these Ru-Ti_4O_7 and Pt-Ti_4O_7 RDEs may have utility for large-scale applications wherein cost of precious metal electrode materials must be minimized.

The largest current density enhancement for oxidation of I^- to I_2 (J=23) and to IO_3^- (J=20) are apparent for the 1% Ru-Ti_4O_7 RDE. This electrode composition corresponds closely to the optimal fractional active area predicted by Weber for microelectrode arrays. As expected, relative current density (J) are largest for the smallest rotation rate.

The Pt-Ti_4O_7 RDEs function similarly as solid Pt RDE for the oxidation of I^-, and redox of H_2O_2 in the acidic media. The large current densities enhancement factors were observed as high as 180, 120 and 40 times for oxidation of I^- to I_2, I^- to IO_3^- and H_2O_2 to O_2, respectively. The enhancement factors increase with the fractional active area deceasing for oxidation of I^- to I_2 and I^- to IO_3^-. The enhancement factor for the oxidation of H_2O_2 to O_2 was achieved at the optimal fractional active area closed to 1%. It is indicative that even for the same electrode materials the enhancement in current density and optimal fractional active area really depend on the characteristics of electrochemical reactions themselves.

The observation that the 0.1% Pt-Ti_4O_7 RDE and the 0.5% Ru-Ti_4O_7 RDE respond in a manner close to ideal microelectrode arrays is consistent with results of a simple comparison of estimated values for the diffusion-layer thickness at the Pt or Ru sites and

the distance between adjacent Pt or Ru sites. The steady-state diffusion layer thickness (δ) at an ideal microdisk electrode is $\pi r/4$, where r is the radius of the microdisk. [23,24] Based on the estimated average diameter of 0.4 μm for Ru sites in Ru-Ti_4O_7 and 0.5 μm for Pt sites in the Pt-Ti_4O_7 RDEs by the peak width for XRD data, we calculate δ = 0.2 μm as a conservative estimate. The values of δ are significantly smaller than the values of 10 μm and 8 μm estimated for the minimum inter-site distance in the 0.5% Ru-Ti_4O_7 and the 0.1% Pt-Ti_4O_7 surfaces, respectively, using SEM. Hence, from this comparison, it is logical to expect that adjacent diffusion zones have virtually no overlap for these electrode materials.

The study of electrocatalysis at pyrochlore oxide $Bi_2Ru_2O_{7.3}$ evidences the foremost premise that anodic discharge of H_2O to produce adsorbed hydroxyl radicals (OH) is a prerequisite of anodic O-transfer reactions. Hence, voltammetric waves for O-transfer reactions are expected to have similar $E_{1/2}$ values which correlate with the onset of O_2 evolution. The $E_{1/2}$ values for the specified anodic reactions at the separate electrodes are similar in spite of large differences in the corresponding E° values. The averages of these $E_{1/2}$ values for the individual electrodes are substantially difference which correlates with the difference in potential for onset of substantial O_2-evolution at different electrodes. This difference in apparent O_2-evolution overpotential is concluded to be a consequence of the difference in true surface areas resulting from the differing amount of polymer used in preparation of the two composite electrode.

The flux density for OH species generated by anodic discharge of H_2O is proportional to A_{active}; however, the flux density of reactant species being transported to the

rotated electrode is proportional to the geometric area (A_{geom}). Hence, the smaller value of the A_{active} : A_{geom} ratio results in a positive shift in $E_{1/2}$ values for anodic O-transfer reactions. The variation of $E_{1/2}$ with changes in the A_{active} : A_{geom} ratio requires further study. However, the composite materials studied here do not provide sufficient control of A_{active} to support such a study.

Composite electrode, $Bi_2Ru_2O_{7.3}$, exhibits sufficient electrocatalytic activity to support the anodic O-transfer reactions for DMSO and TMSO, whereas these reactions are not observed at the common anode materials (Au, Pt, PbO_2, GC).

The $Bi_2Ir_2O_7$ composite electrode material can be used as an electrochemical catalyst for both anodic oxidation of iodide and cathodic reduction of iodate in acidic medium (0.1 M H_2SO_4). The characteristic of the pyrochlore oxide $Bi_2Ir_2O_7$ electrode material is similar to that of the solid Ir electrode. The pyrochlore oxide $Bi_2Ir_2O_7$ electrode material is better than solid Ir in the enhancement of current density and for the transport-controlled reactions. The qualitative conclusion drawn from this study is that the catalytic activity depend on the material itself.

The plateau currents of reduction of IO_3^- for solid Ir RDE were virtually independent of scan rate, which is representative of a purely transport-controlled process. The plateau currents varied nonlinearly with scan rates at the $Bi_2Ir_2O_7$ composite electrode, which is indicative of mixed control by surface- and transport-controlled processes.

The values of the current at E = 0.57 V and 0.15 V at the $Bi_2Ir_2O_7$ composite RDE on the negative scan increased as a linear function of $\omega^{1/2}$ but with a nonzero intercept,

which is indicative of the simultaneous occurrence of surface-controlled reduction and transport-controlled reaction of IO_3^- at the $Bi_2Ir_2O_7$ composite RDE. Linearity of i^{-1}-$\omega^{-1/2}$ plots is evidence that reduction of IO_3^- at the Ir RDE occurs by a mixed transport-kinetic controlled mechanism.